

DOCTORAL THESIS

**Theory of Multipole Fluctuation Mediated
Superconductivity and Multipole Phase:**

**Important Roles of Many Body Effects
and Strong Spin-Orbit Coupling**

February 13 2020

Department of Physics, Nagoya University

Material Science (Physics)

Condensed-Matter Theory Group (Sc)

Rina Tazai

Contents

1	General introduction	3
1.1	Problems in strongly correlated materials	3
1.2	Roles of many body effects	5
1.3	Multipole degrees of freedom	6
2	Functional Renormalization Group (fRG) study	9
	Introduction	
	Model	
2.1	Multiorbital Hubbard model	9
	Method & Result	
2.2	4-point vertex by fRG+cRPA	11
2.3	3-point vertex and p-p (p-h) fluctuations	13
2.4	Superconductivity by fRG+cRPA	15
	Discussion	
2.5	Analysis of the U -VC	17
2.6	Diagrammatic method vs fRG analysis	18
	Conclusion	
3	Cooperation of el-ph and AFM fluctuations for SC state	22
	Introduction	
	Model	
3.1	Hubbard-Holstein model (B_{1g} phonon)	22
	Method & Result	
3.2	B_{1g} -orbital fluctuations	24
3.3	Superconductivity	26
	Discussion	
3.4	Local approximation for U -VC	28
3.5	Filling dependence	29
3.6	Retardation & impurity effects	29
	Conclusion	
4	S-wave superconductivity in CeCu_2Si_2	33
	Introduction	
	Model	
4.1	$\Gamma_7^{(1)}$ - $\Gamma_7^{(2)}$ Periodic Anderson Model	34
4.2	Multipole symmetry	36
	Method & Result	
4.3	Green function	38
4.4	Multipole susceptibility	39
4.5	Phonon mediated interaction	42
4.6	SC gap equation	43
4.7	U -VC	44
4.8	SC phase diagram	47

Discussion	
4.9 CEF splitting and f - f hopping	48
4.10 Important roles of χ -VC	49
4.11 Microscopic origin of S -wave SC	51
4.12 Retardation effect	54
Conclusion	
5 Multipole phase	59
Introduction	
Model	
5.1 Γ_8 PAM & multipole symmetry	59
Method & Result	
5.2 Magnetic multipole susceptibility	61
5.3 Electric multipole susceptibility	62
Discussion	
5.4 Microscopic origin of quadrupole phase	64
5.5 Magnetic field	65
Conclusion	
6 Summary	69
7 Appendix	72

1 General introduction

1.1 Problems in strongly correlated materials

In the strongly correlated electron systems (SCES), there remains considerable unsolved problems. We review some of them as an introduction to our present study. Until now, various interesting quantum phenomena have been observed in SCES. For instance, phase transition with nontrivial order parameters and transport phenomena have been studied intensively. However, it is left as a long-standing problem to understand these phenomena microscopically, since it requires to solve "many body problem" among a number of electrons $N \sim 10^{23}$. Therefore, development of microscopic many-body theories is one of the important issues in SCES. In this study, we aim to understand these phenomena in the same framework. Especially, we focus on microscopic origin of "unconventional superconductivity" and "hidden order" motivated by recent progress in this field.

First, we review a brief history of theoretical studies on microscopic origin of superconductivity. In 1957, Bardeen, Cooper and Schrieffer discovered that phonon mediated retarded attraction works as a glue for Cooper pairs. Now, it is well known as BCS theory and succeeded in explaining the characteristic features of weakly correlated superconductor mainly composed of s - and p -orbital electrons.

On the other hand, the first discovery of superconductor in SCES was reported in heavy fermion (HF) system CeCu_2Si_2 in 1979. After that, various transition metals such as cuprates, ruthenate and iron based compounds were also recorded. However, the microscopic origin of these superconductor could not be understood within BCS theory since various kinds of particle-hole (p-h) instabilities due to the strong Coulomb repulsion can overwhelm BCS-like electron-phonon (el-ph) interaction. In this case, non-BCS superconducting (SC) states may appear. In facts, various p-h ordered phases such as magnetic, charge, and orbital ordered phase appear near SC phase in SCES. Thus, theory of SC pairing mechanism beyond BCS formalism is required for SCES.

To solve the problem, simple approximation based on Random Phase Approximation + Migdal-Eliashberg theorem (RPA+ME) has been used for years. It succeeded in explaining unconventional SC phase near antiferro magnetic (AFM) phase in SCES, such as cuprates superconductors. To sum up, essence of RPA+ME theory is listed as follows;

- (i) Elemental p-h excitation is given by simple 1-loop process as shown in Fig.1(b).
- (ii) p-h fluctuations are given by p-h ladder and p-h bubble processes.
- (iii) p-p instability in forming Cooper pairs is given by p-p ladder process.
- (iv) Coupling constant between electron and p-h fluctuations in gap equation is bare Coulomb U .

Here, (i) and (ii) correspond to RPA theory and (iii)-(iv) represent ME theory. Especially, (iv) is often called Migdal approximation. Based on (i)~(ii), development of AFM fluctuations is explained, and AFM fluctuations work as repulsion for Cooper pairs according to (iii)~(iv). Therefore, one of the main

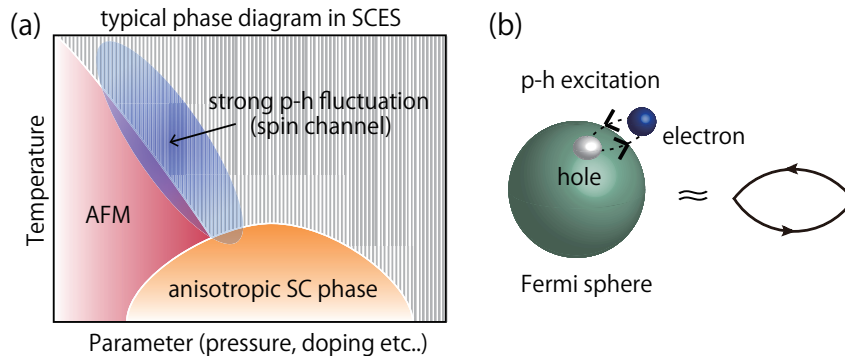


Figure 1: (a) Typical phase diagram often seen in SCES, such as cuprates, Fe-based and HF compounds. (b) p-h excitation due to 1 loop process.

conclusion from RPA+ME theory is that nodal pairing state emerges to gain condensation energy. It is well known that a lot of superconductors in SCES show similar phase diagram, which means that AFM phase is close to SC phase as shown in Fig.1(a). Therefore, it is widely believed that typical SC phase diagram in SCES had already been well understood at this stage.

However, recent improved experiments revealed isotropic s-wave SC states emerge even near AFM phase in SCES, such as Fe-compounds, organic system and HF system CeCu_2Si_2 . In particular, discovery of s-wave SC state in CeCu_2Si_2 in 2017 surprised researchers since it had been believed as *d*-wave superconductor for a long time after 1979. These discoveries revealed that RPA+ME theory fails in many systems and unreliable. Therefore, we have to go beyond conventional RPA+ME theory.

Now, we are at the starting point for constructing a new microscopic theory of SC paring in SCES. Hereafter, we move into our present study. To go beyond RPA+ME theory, we focus on higher-order many body effects. Through our study in multi-orbital SCES, we found that violation of (i) and (iv) occurs and they are replaced with

(i)' Many body effects beyond 1-loop process are important for p-h fluctuations.

(iv)' Coupling constant changes from bare Coulomb U to dressed one due to many-body effect.

These findings are our main results in the present paper. Thus, we show more detailed explanation on this point in Sec.1.2. Based on the results, we reconsider following questions;

Q1: In particular, what type of scattering process is significant in multi-orbital SCES ?

Q2: Is it true that AFM fluctuations and el-ph coupling always compete in SC paring mechanism as derived in RPA+ME theory?

Q3: How can we understand s-wave SC state in CeCu_2Si_2 ?

In addition, we notice that our findings is also helpful to understand long-standing issues in normal states as well as SC states. For instance, microscopic origin of hidden ordered phase in HF system remains significant problem. Therefore, we study on CeB_6 as one of the typical hidden ordered system. Then, we add the following question;

Q4: How can we understand hidden ordered phase in CeB_6 ?

To answer these fundamental questions, we study SC paring and hidden ordering mechanism in SCES based on the common "many-body effects mechanism".

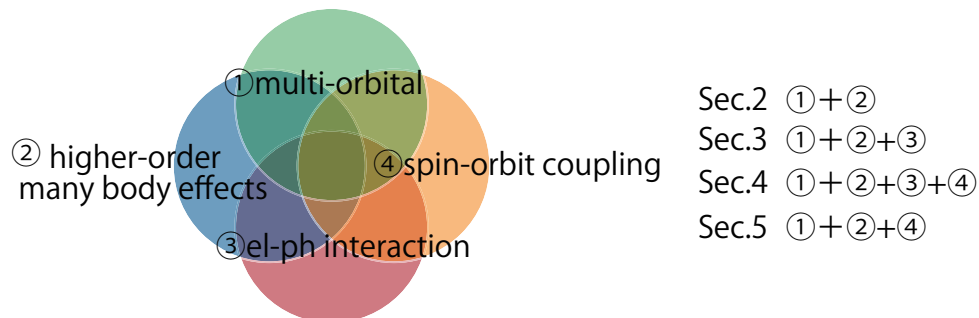


Figure 2: Map of the present study. We propose a microscopic origin of SC paring and hidden ordering considering higher-order many body effects, el-ph interaction, SOI and multi-orbital nature.

To understand the questions Q3 and Q4, strong spin-orbit interaction (SOI) has to be taken into account. In this case, *f*-electrons are characterized by total angular momentum J in stead of spin and orbital angular momentum S, L . Therefore, p-h fluctuations are defined in J -space, which we call multipole fluctuation. Concept of multipole fluctuation is introduced in Sec.1.3. Development of higher-ranks multipole fluctuations is characteristic property of *f*-electron systems and brings various interesting phenomena. For this reason, the 5th question is

Q5: How do multipole fluctuations work in HF system in the presence of many body effects ?

In this paper, we discuss above-mentioned questions in the following 4 sections (Sec.2~5). In Sec.2, we study *d*-orbital Hubbard model based on functional-renormalized-group+constrained RPA (fRG+cRPA)

method to discover fundamental properties of many body effect beyond RPA+ME, corresponding to Q1. In Sec.3, we study Hubbard-Holstein model with phonon-mediated interaction to answer the Q2. After that, in Sec.4, we move into HF superconductor CeCu₂Si₂ with strong SOI to answer Q3 and Q5. In Sec.5, we propose a microscopic origin of hidden ordered phase in CeB₆ related to Q4 and Q5. We summarized our present study in the map of Fig.2.

After all, we obtain the following results, which answer the questions Q1~Q5;

Result 1: Mode coupling effect between orbital and spin degrees of freedom plays essential roles for SC paring in multi-orbital SCES system.

Result 2: AFM fluctuations and phonon-mediated interaction can work cooperatively and enhance the T_c of isotropic SC paring.

Result 3: Mode coupling effect is more significant in f -electron systems due to the strong SOI. Interference between electric and magnetic multipole fluctuations stabilize s-wavs SC.

Result 4: Interference among different ranks multipole fluctuations causes the hidden ordered phase.

1.2 Roles of many body effects

In this section, we explain significant roles of many body effects beyond conventional theory. Before that, we review conventional RPA+ME theory in more detail by using Feynman diagram. In Fig.3, we show the Feynman diagram of p-h fluctuations by RPA. Solid lines represent 1-particle propagator (Green function) and dotted line corresponds to el-el interaction, such as Coulomb interaction U . Filled region shows reducible 3-point vertex function. We consider simple 1-loop p-h excitation corresponding to the 1st term of right-hand-side (rhs) of the figure within RPA. Then, the Coulomb interaction U is considered by bubble and ladder process as shown in the 2nd and 3rd terms of rhs in Fig.3, respectively.

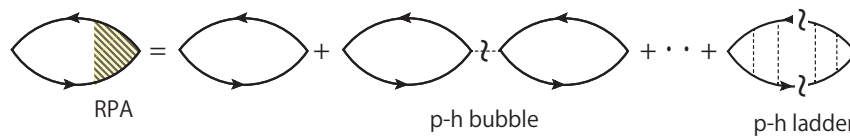


Figure 3: p-h fluctuations due to p-h bubble and ladder process. Solid and dotted line correspond to electron propagator and Coulomb repulsion, respectively.

After that, p-p instability is obtained by p-p ladder process as shown in Fig.4. The red (black) colored rectangular shows reducible (irreducible) 4-point vertex function of p-p channel. p-p channel 4-point vertex is composed of p-h fluctuations. In ME approximation, coupling constant between Green function and p-h fluctuations are given by the bare Coulomb interaction U represented as the right digram in Fig.4.

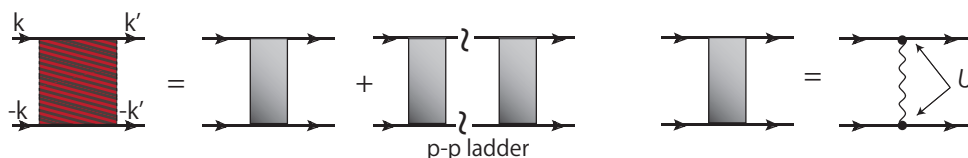


Figure 4: SC paring instability due to p-p ladder process. Red (black) filled area shows reducible (irreducible) 4-point vertex function, respectively. Wavy line corresponds to p-h fluctuations.

On the other hand, in the present study, we consider many body effects beyond RPA+ME theory. In this case, irreducible p-h fluctuations are dressed by 3-point vertex correction (VC) as shown in Fig.5. The red colored region represents the 3-point VC due to the many body effects beyond RPA. Here, 3-point VC is reducible with respect to U . The 1st term of the rhs of the figure shows 1 loop process included in RPA. In contrast, the 2nd and 3rd term are VC neglected in RPA. Through our study, we found that these VC play significant roles for SC paring as well as hidden ordering. Thus, we call them χ -VC,

collectively. The 2nd term shows VC due to the single p-h fluctuation, which is called Maki-Thompson (MT) term. The 3rd term corresponds to 2nd order of p-h fluctuation, which is called Aslamazov-Larkin (AL) term.

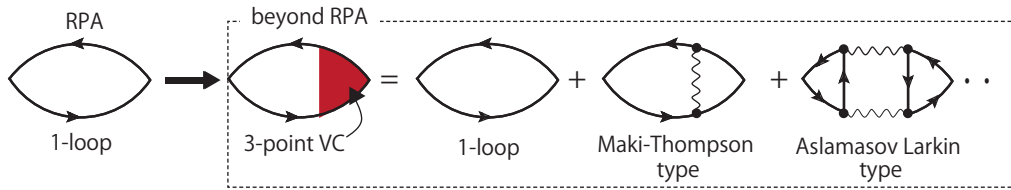


Figure 5: p-h fluctuations beyond RPA+ME theory. The red colored region shows 3-point VC.

Fig.6 represents the irreducible 4-point vertex in p-p ladder beyond ME theory. The blue colored triangle gives 3-point VC neglected in ME theory. We call the VC for p-p ladder U -VC. The U -VC also include AL and MT terms. In the present study, we revealed that U -VC as well as χ -VC play significant roles to understand the SC paring mechanism in SCES.

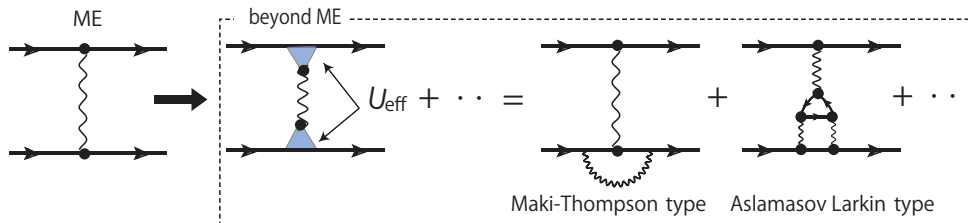


Figure 6: Blue colored triangle shows 3-point VC beyond ME. The VC due to the 1st (2nd) order of p-h fluctuations corresponds to MT (AL) term.

In general, it is difficult to understand what kind of scattering process is essentially important in SCES, since it is required to consider all of the possible processes including higher order terms than above-mentioned processes. To overcome this difficulty, we study fRG+constrained RPA (cRPA) in the present study. In this method, parquet type scatterings are automatically generated only by solving differential equation. Therefore, obtained results are unbiased and quite reliable. However, it is still hard to identify the essential process solely by fRG+cRPA, since a number of minor processes are automatically included. Thus, it is important to analyze by using more than 2 different method, such as diagrammatic calculation in addition to fRG+cRPA. For this reason, in the present study, we compare the obtained result by both method and revealed that the significant contribution comes from the interference between different types of p-h fluctuations. In particular, it is due to AL-type U -VC and χ -VC.

1.3 Multipole degrees of freedom

In this section, we introduce "multipole" to classify the p-h order parameters in f -electron system with strong SOI. Here, we show the definition of the multipole order parameter based on d -electron model, since it is easier than f -electron system. First, we consider d_{zx} - and d_{yz} -orbital wave function given by

$$\psi_{zx}(\vec{r}) = R_{n,2}(r) \frac{1}{\sqrt{2}} \{Y_{2,1}(\theta, \phi) + Y_{2,-1}(\theta, \phi)\}, \quad (1.1)$$

$$\psi_{yz}(\vec{r}) = R_{n,2}(r) \frac{i}{\sqrt{2}} \{Y_{2,1}(\theta, \phi) - Y_{2,-1}(\theta, \phi)\}, \quad (1.2)$$

where $R_{n,l}(r)$ and $Y_{l,m}(\theta, \phi)$ are radial distribution function and spherical harmonics, respectively. The index (n, l, m) denotes (principal, azimuth, magnetic) quantum number. By using the wave function, the possible p-h order parameter (OP) is expressed as

$$OP = \sum_{a,a'=d_{zx},d_{yz}} \int d\vec{r}_i \psi_a^*(\vec{r}_i) f_{aa'}(\vec{r}_i) \psi_{a'}(\vec{r}_i) \quad (1.3)$$

where i denotes the site index. The function $f_{aa'}(\vec{r}_i)$ represents the anisotropy of electrons charge distribution and defines the symmetry of the local order parameter. Here, the order parameter function f is also written by using $R_{n,l}(r)$ and $Y_{l,m}(\theta, \phi)$. Therefore, the OP is expressed as

$$OP \propto \int d\phi Y_{l,m_1}^* Y_{l',m'} Y_{l,m_2} = \delta(m_1 - m' - m_2) \quad (f_{aa'}(\vec{r}_i) \propto Y_{l',m'}). \quad (1.4)$$

In this case, possible combination for $(l'm')$ in $Y_{l',m'}(\theta, \phi)$ are 9 patterns given by

$$f_{aa'}(\vec{r}_i) \propto Y_{0,0}, Y_{1,0}, Y_{1,\pm 1}, Y_{2,0}, Y_{2,\pm 1}, Y_{2,\pm 2}, \quad (1.5)$$

These 9 possible order parameters are classified into multipole channel by m' . $f_{aa'}(\vec{r}_i)$ for $m' = (0, 1, 2)$ corresponds to (monopole, dipole, quadrupole), which belongs to rank (0,1,2). In more general, when the wave functions of the ground states are written by $Y_{l,m=a\sim b}$, the possible $f_{aa'}(\vec{r}_i)$ is given by

$$f_{aa'}(\vec{r}_i) \propto Y_{l',0}, Y_{l',\pm 1} \sim Y_{l',\pm(b-a)} \quad (0 \leq l' \leq l), \quad (1.6)$$

Therefore, if we consider all of the $t_{2g} + e_g$ -orbital, which means that the wave function is written by $Y_{2,0}Y_{2,\pm 1}, Y_{2,\pm 2}$, we obtain 25-type possible orders up to the hexadecapole (rank 4).

On the other hand, the 'active' multipole orders are only 4 type (9-type) in the case of d_{zx} - and d_{yz} -orbital ($t_{2g} + e_g$ -orbital) system since the independent degrees of freedom are given by square of the orbital number. For instance, in the monopole case ($f_{aa'}(\vec{r}_i) \propto 1$), the OP is rewritten as

$$\begin{aligned} OP(\text{mono}) &= \sum_{a,a'=d_{zx},d_{yz}} \int d\vec{r}_i \psi_a^*(\vec{r}_i) \sqrt{x^2 + y^2 + z^2} \psi_{a'}(\vec{r}_i) \\ &= \int d\vec{r}_i \sqrt{x^2 + y^2 + z^2} (\psi_{d_{zx}}^*(\vec{r}_i) \psi_{d_{zx}}(\vec{r}_i) + \psi_{d_{yz}}^*(\vec{r}_i) \psi_{d_{yz}}(\vec{r}_i)) \propto n_{zx} + n_{yz}. \end{aligned} \quad (1.7)$$

To derive the final expression in Eq.(1.7), we use the fact that $\int d\vec{r}_i \sqrt{x^2 + y^2 + z^2} \psi_{d_{zx}}^*(\vec{r}_i) \psi_{d_{yz}}(\vec{r}_i) = 0$ since integrands are odd function for x or y . Therefore, the order parameter corresponds to $n_{zx} + n_{yz}$. More over, we obtain the following matrix representation focusing on the orbital dependence of $\hat{f}(\vec{r}_i)$ for monopole.

$$OP(\text{mono}) = \begin{pmatrix} \psi_{zx} & \psi_{yz} \\ \psi_{zx}^* & \psi_{yz}^* \end{pmatrix} \begin{pmatrix} 1 & 0 \\ 0 & 1 \end{pmatrix} \propto \hat{I}. \quad (1.8)$$

In the same way, we also obtain the $x^2 - y^2$ -type quadrupole OP given by

$$\begin{aligned} OP(\text{quad} : x^2 - y^2) &= \sum_{a,a'=d_{zx},d_{yz}} \int d\vec{r}_i \psi_a^*(\vec{r}_i) (x^2 - y^2) \psi_{a'}(\vec{r}_i) \\ &= \int d\vec{r}_i (x^2 - y^2) (\psi_{d_{zx}}^*(\vec{r}_i) \psi_{d_{zx}}(\vec{r}_i) - \psi_{d_{yz}}^*(\vec{r}_i) \psi_{d_{yz}}(\vec{r}_i)) \end{aligned} \quad (1.9)$$

In this case, the order parameter is given by $\langle \psi_{d_{zx}}^*(\vec{r}_i) \psi_{d_{zx}}(\vec{r}_i) - \psi_{d_{yz}}^*(\vec{r}_i) \psi_{d_{yz}}(\vec{r}_i) \rangle$ and

$$OP(\text{quad} : x^2 - y^2) = \begin{pmatrix} \psi_{zx} & \psi_{yz} \\ \psi_{zx}^* & \psi_{yz}^* \end{pmatrix} \begin{pmatrix} 1 & 0 \\ 0 & -1 \end{pmatrix} \propto \hat{L}_x^2 - \hat{L}_y^2. \quad (1.10)$$

In addition, xy -type quadrupole OP is also independent OP to above mentioned 2-type OP.

$$OP(\text{quad} : xy) = \int d\vec{r}_i xy (\psi_{d_{zx}}^*(\vec{r}_i) \psi_{d_{yz}}(\vec{r}_i) + \psi_{d_{yz}}^*(\vec{r}_i) \psi_{d_{zx}}(\vec{r}_i)), \quad (1.11)$$

where the order parameter corresponds to $\langle \psi_{d_{zx}}^*(\vec{r}_i) \psi_{d_{yz}}(\vec{r}_i) + \psi_{d_{yz}}^*(\vec{r}_i) \psi_{d_{zx}}(\vec{r}_i) \rangle$

$$OP(\text{quad} : xy) = \begin{pmatrix} \psi_{zx} & \psi_{yz} \\ \psi_{zx}^* & \psi_{yz}^* \end{pmatrix} \begin{pmatrix} 0 & 1 \\ 1 & 0 \end{pmatrix} \propto \hat{L}_x \hat{L}_y. \quad (1.12)$$

We note that xz or yz type quadrupole OP goes to zero due to the symmetry of the wave function. The $3z^2 - r^2$ type quadrupole OP is not independent OP since we obtain the following equation;

$$\begin{aligned} OP(\text{quad} : 3z^2 - r^2) &= \sum_{a,a'=d_{xz},d_{yz}} \int d\vec{r}_i \psi_a^*(\vec{r}_i) (3z^2 - r^2) \psi_{a'}(\vec{r}_i) \\ &= \int d\vec{r}_i (3z^2 - r^2) (\psi_{d_{zx}}^*(\vec{r}_i) \psi_{d_{zx}}(\vec{r}_i) + \psi_{d_{yz}}^*(\vec{r}_i) \psi_{d_{yz}}(\vec{r}_i)), \end{aligned} \quad (1.13)$$

where the order parameter corresponds to $n_{zx} + n_{yz}$, which is the same as that of monopole. Now, we have already obtained 3-multipole OP including 1-monopole and 2-quadrupole OP. The final one is dipole one, which is given by

$$OP(\text{dipole}) = \begin{matrix} \psi_{zx} & \psi_{yz} \\ \psi_{zx}^* & \psi_{yz}^* \end{matrix} \begin{pmatrix} 0 & i \\ -i & 0 \end{pmatrix} \propto \hat{L}_z. \quad (1.14)$$

In the dipole ordered phase, TRS is broken even in the orbital space. For instance, local circular current emerges in the dipole phase. As we show in this section, the OP matrix is written by using the orbital angular momentum operator \hat{L} . On the contrary, with the strong SOI, the \hat{L} changes to $\hat{J} = \hat{L} + \hat{S}$. Therefore, it is naturally expected that the rank of OP with SOI tends to be higher than that without the SOI. Here, the active OP in multipole basis are summarize as follows.

	d_{zx}, d_{yz}	$t_{2g} + e_g$	Sec.4 (Γ_7)	Sec.5 (Γ_8)
number of the active OP	4	25	16	16
the highest rank	quadrupole	hexadecapole	dotriacontapole	octupole

2 Functional Renormalization Group (fRG) study

Introduction

In Sec.2, we investigate SC mechanism based on functional renormalization group (fRG) study to understand fundamental properties of many-body effects beyond RPA+ME theory [1].

Recently, SC phase associated with multi orbital nature in SCES has been studied intensively. In the multi orbital systems, such as heavy Fermion and Fe-based superconductors, SC phase emerges near the orbital ordered phase. Therefore, it is naturally expected that SC pairing glue is derived from strong orbital fluctuations. However, in the theoretical way, it is difficult to explain the emergence of orbital ordering/fluctuations within the realistic condition. In fact, only p-h fluctuations related to the spin degrees of freedom become dominant over that of orbital channel within the conventional mean-field scheme, such as RPA and fluctuation exchange (FLEX) approximation [2].

Thus, it is required to go beyond mean-field-level approximations to reveal the low temperature physics in multi orbital systems. Especially, we focus on the many body effects beyond conventional theory, which is called vertex corrections (VC) in terms of quantum statistical mechanics [3]-[5]. For this purpose, we study fRG theory [6, 7] as a reliable and unbiased method to consider VC in multi orbital system, since it enables us to calculate parquet type VC automatically only by solving the differential equation, which is called RG equation. Thus, VC for p-p and p-h channels fluctuations are generated equivalently without the violation of Pauli exclusion principle.

Once the orbital fluctuations develop, it is naturally expected that orbital-fluctuations-mediated SC phase appears. In particular, spin triplet SC (TSC) pairing can be induced by orbital fluctuations as well as ordinal spin singlet SC. Within ME scheme, SC pairing interaction consists of orbital (spin) channel fluctuations $\chi^{c(s)}$ and bare Coulomb interaction $U^{c(s)}$ summarized as

	spin channel		charge channel	
spin singlet SC	repulsive	$3U^s\chi^sU^s$	attractive	$U^c\chi^cU^c$
spin triplet SC	attractive	$U^s\chi^sU^s$	attractive	$U^c\chi^cU^c$

Accordingly, spin fluctuations driven spin singlet SC phase easily appears even if $\chi^c \simeq \chi^s$ due to the coefficient '3' for spin singlet SC given in the table compared with triplet SC. In spite of that, the bare U can be enhanced or suppressed by considering the VC, which is confirmed in the present fRG study. Alto, the same VC causes (i) enhancement (suppression) of the p-h susceptibilities and (ii) that of the effective SC pairing interaction. Note that (i) and (ii) can be realized simultaneously.

In this section, we study 2-orbital Hubbard model for describing Sr_2RuO_4 [8]-[17] by using the fRG theory to reveal an origin of unconventional SC pairing, which comes from orbital degrees of freedom as well as many body effects beyond RPA+ME theory. For this purpose, we analyze linearized SC gap equation with the VC. As a result, we reveal that the bare coupling constant $U^{s(c)}$ changes into effective coupling constant $U_{\text{eff}}^{s(c)}$. Especially, charge ch coupling constant is drastically enhanced by moderate spin fluctuations due to the VC at low temperature, while spin ch interaction is suppressed. Therefore, unconventional SC phase driven by orbital fluctuations can appear in multiorbital SCES, such as Fe (Ru)-based and organic superconductors. Also, phonon mediated SC pairing interaction can be enhanced by factor U_{eff}^c/U^c , which we will discuss in the Sec.3.

Model

2.1 Multiorbital Hubbard model

Here, we introduce 2-orbitals Hubbard model on 2D square lattice for describing d_{xz} , d_{yz} -orbitals in Sr_2RuO_4 . The Hamiltonian for the kinetic part is written by

$$\hat{H}_0 = \sum_{\mathbf{k}\sigma lm} \xi_{\mathbf{k}}^{lm} d_{\mathbf{k}l\sigma}^\dagger d_{\mathbf{k}m\sigma}, \quad (2.1)$$

where l, m takes 1 or 2, which corresponds to d_{xz} or d_{yz} -orbital, respectively. The energy dispersion is defined as $\xi_k^{11} = -2t \cos k_x - 2t'' \cos k_y$, $\xi_k^{22} = -2t \cos k_y - 2t'' \cos k_x$, $\xi_k^{12} = \xi_k^{2,1} = -4t' \sin k_x \sin k_y$. Energy scale is measured from Fermi energy and the energy unit is $t = 1$. The hopping parameters are fixed at $(t, t', t'') = (1, 0.1, 0.1)$. The electron's number is fixed at $n = n_{xz} + n_{yz} = 4 \times (2/3) = 2.67$, where t_{2g} ground states are filled up with 4 electrons. The band dispersion and Fermi surfaces are plotted in Figs.8(a) and (b). Quasi 1D Fermi surfaces (α and β) are obtained. The nesting vector $\mathbf{Q} = (2/3\pi, 2/3\pi)$ is consistent with observed results by neutron scattering experiment [18].

Here, we introduce the interaction terms given by the on-site Coulomb interaction, which includes intra- (inter-) orbital U (U'), pair hopping J' and Hund's coupling J . The definition of U, U', J, J' are given in Fig.7. The Hamiltonian for the interaction part is given by

$$\hat{H}_U = \frac{1}{4} \sum_i \sum_{l'mm'} \sum_{\sigma\sigma'\rho\rho'} U_{l'mm'}^{\sigma\sigma'\rho\rho'} d_{il\sigma}^\dagger d_{il'\sigma'} d_{im\rho} d_{im'\rho'}^\dagger, \quad (2.2)$$

$$\hat{U}^{\sigma\sigma'\rho\rho'} = \frac{1}{2} \hat{U}^s \vec{\sigma}_{\sigma\sigma'} \cdot \vec{\sigma}_{\rho'\rho} + \frac{1}{2} \hat{U}^c \delta_{\sigma\sigma'} \delta_{\rho'\rho}, \quad (2.3)$$

where $\vec{\sigma}$ is Pauli matrix vector and \hat{U} is the bare 4-point vertex function given by 4×4 tensor, which is anti-symmetrized as $U_{5678}^{1234} = -U_{7856}^{3412}$ based on anti-commutation relation for Fermion. All elements in $\hat{U}^{s(c)}$ are listed as follows,

$$\begin{cases} \hat{U}^s = U & (l = l' = m = m') \\ \hat{U}^s = U' & (l = m \neq l' = m') \\ \hat{U}^s = J & (l = l' \neq m = m') \\ \hat{U}^s = J' & (l = m' \neq l' = m), \end{cases} \quad \begin{cases} \hat{U}^c = -U & (l = l' = m = m') \\ \hat{U}^c = U' - 2J & (l = m \neq l' = m') \\ \hat{U}^c = -2U' + J & (l = l' \neq m = m') \\ \hat{U}^c = -J' & (l = m' \neq l' = m). \end{cases} \quad (2.4)$$

Other elements not listed in Eq.(2.4) go to zero. To simplify the model, we assume the relation $J =$

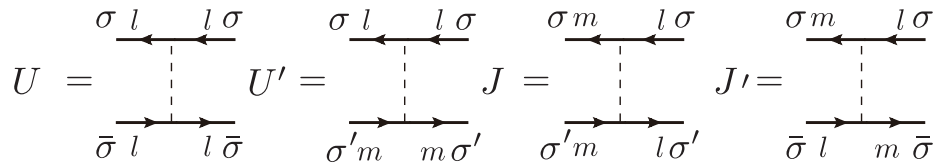


Figure 7: Definition of U, U', J, J' under the condition of $l \neq m$.

$J' = (U - U')/2$ in the numerical calculation. Therefore, there are only two independent parameters, such as U and J . Note that SU(2) symmetry is satisfied in the present system since spin-orbit coupling is neglected.

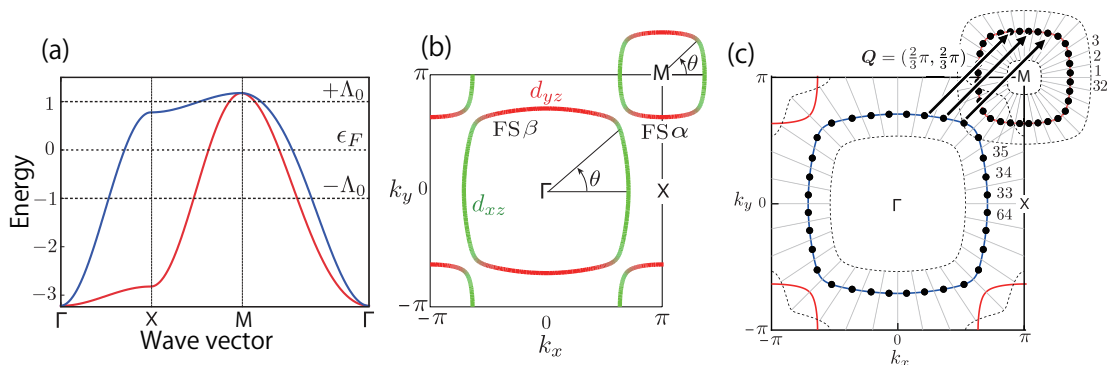


Figure 8: (a) Obtained band dispersion and (b) Fermi surfaces mainly formed by d_{xz} (green) and d_{yz} (red) orbital. (c) The region of each patches on the Fermi surface. Black arrows show major nesting vector at $\mathbf{Q} = (2/3\pi, 2/3\pi)$.

In the fRG+constrained RPA method, d -electrons energy scale is divided into higher energy ($|\xi_{\mathbf{k}}| > \Lambda_0$) and lower energy part ($|\xi_{\mathbf{k}}| < \Lambda_0$). We perform RPA for the higher-energy part and adopt RG method

for the lower-energy part. In addition, \mathbf{k} -space in the lower-energy part is divided into several grained region, which we call 'patch'. In the present numerical study, we use 32 patches for each Fermi surfaces. Figure 8(c) shows the contours for $|\xi_{\mathbf{k}}| = \Lambda_0 = 1$ and the center of patches $p_\alpha(p_\beta)$, which takes $1 \sim 32$ ($33 \sim 64$).

Finally, we define d -electrons Green function as

$$\hat{G}(k) = \frac{1}{i\epsilon_n - \hat{H}_0}, \quad (2.5)$$

where $k = (\mathbf{k}, \epsilon_n) = (\mathbf{k}, (2n+1)\pi T)$. $\hat{G}(k)$ does not have spin index since \hat{H}_0 is independent of the spin. Therefore, $\hat{G}(k)$ is represented by 2×2 matrix in the orbital space.

● key facts

- * 1 We use 2-orbital (d_{xz}, d_{yz}) Hubbard model with on-site Coulomb interaction.
- * 2 The bare 4-point vertex U has SU(2) symmetry and parametrized by U and J .
- * 3 We perform RPA for high energy region $|\xi| > \Lambda_0$ and fRG for lower region $|\xi| < \Lambda_0$.
- * 4 We divide \mathbf{k} -space into 32 patches for low energy region $|\xi| < \Lambda_0$.

Method & Result

2.2 4-point vertex by fRG+cRPA

Here, we calculate fully renormalized 4-point vertex function based on the fRG+constrained RPA (cRPA) method [19]. In this combined method, high energy scatterings are calculated by RPA while lower energy ones are obtained by fRG method. The initial values for the 4-point vertex are composed of \hat{U}^c and \hat{U}^s in Eq.(2.2)~(2.4). Note that the initial vertex does not have \mathbf{k} -dependence as shown in Eq.(2.4).

Then, the 4-point vertex $\hat{U}^{c,s}$ comes to have \mathbf{k} -dependence by considering high energy scatterings ($|\xi_{\mathbf{k}}| > \Lambda_0$) within the cRPA method as

$$\hat{\Gamma}_{\text{cRPA}}^{s(c)}(k+q, k; k'+q, k') = \hat{U}^{s(c)} + \hat{U}^{s(c)} \hat{\chi}_{\text{cRPA}}^{s(c)}(k-k') \hat{U}^{s(c)} - \{\text{A.C.}\}, \quad (2.6)$$

$$\hat{\chi}_{\text{cRPA}}^{s(c)}(q) = \frac{\hat{\chi}_{\text{cRPA}}^0(q)}{\hat{1} - \hat{U}^{s(c)} \hat{\chi}_{\text{cRPA}}^0(q)}, \quad (2.7)$$

$$\hat{\chi}_{\text{cRPA}}^0(q) = -T \sum_k \hat{G}(k+q) \theta(|\xi_{\mathbf{k}+q}| - \Lambda_0) \hat{G}(k) \theta(|\xi_{\mathbf{k}}| - \Lambda_0), \quad (2.8)$$

where $q = (\mathbf{q}, \omega_m) = (\mathbf{q}, 2\pi Tm)$ and 'A.C.' denotes anti-commutation of the 2nd term in the rhs of Eq.(2.6) for orbital, spin and k index. The detailed definition of $\Gamma(k+q, k; k'+q, k')$ is given as a Feynman diagram in Fig.9. θ is Heaviside step function defined as $\theta(k) = 1(0)$ for $k > 0(k < 0)$. Therefore, we only consider d -electrons with high energy than Λ_0 in Eq.(2.8) within cRPA. This assumption is justified when many body effects beyond RPA remain small in the high energy region, while it becomes larger in low energy region.

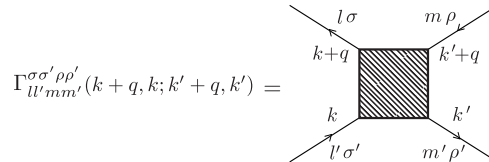


Figure 9: Definition of 4-point vertex function in the present study.

Then, we perform the fRG method to obtain fully renormalized 4-point vertex function $\hat{\Gamma}_{\text{RG}}$ including low energy scatterings. We use the $\hat{\Gamma}_{\text{cRPA}}^{s(c)}$ as a initial value for fRG. In the fRG formalism, $\hat{\Gamma}_{\text{RG}}$ is

automatically obtained by solving the differential equation. The RG equation in the band basis within 1-loop approximation is given by

$$\begin{aligned} \frac{d}{d\Lambda} \Gamma_{\text{RG}}(k_1, k_2; k_3, k_4) = & -T \sum_{k, k'} \left[\frac{d}{d\Lambda} \tilde{G}(k) \tilde{G}(k') \right] \left[\Gamma_{\text{RG}}(k_1, k_2; k, k') \Gamma_{\text{RG}}(k, k'; k_3, k_4) \right. \\ & \left. - \Gamma_{\text{RG}}(k_1, k_3; k, k') \Gamma_{\text{RG}}(k, k'; k_2, k_4) - \frac{1}{2} \Gamma_{\text{RG}}(k_1, k; k', k_4) \Gamma_{\text{RG}}(k, k_2; k_3, k') \right] \end{aligned} \quad (2.9)$$

where the compact notation k denotes $k = (\mathbf{k}, \epsilon_n, u, \sigma)$, where u is band index. The 1st and 2nd contributions in the rhs of Eq.(2.9) come from p-h scattering and the 3rd one corresponds to p-p scatterings. To perform the RG method, the Green function $\tilde{G}(k)$ in the band basis is defined as

$$\tilde{G}(k) \equiv G(k) \theta(|\xi_{\mathbf{k}}^u| - \Lambda). \quad (2.10)$$

Then, Eq.(2.9) is rewritten by on-shell Green function ($\Lambda - d\Lambda \leq |\xi_{\mathbf{k}}| < \Lambda$) and high energy one ($\Lambda \leq |\xi_{\mathbf{k}}| < \Lambda_0$). In particular, the 1st term of the rhs of Eq.(2.9) is given by

$$\begin{aligned} \text{1st term} = & \int_{|\xi_{\mathbf{k}}|=\Lambda} \frac{dk}{v_{\mathbf{k}}} \Gamma_{\text{RG}}(k_1, k_2; k, k-k_1+k_2) \frac{f(\xi_{k-k_1+k_2}) - f(\xi_{\mathbf{k}})}{\xi_{k-k_1+k_2} - \xi_{\mathbf{k}}} \theta(|\xi_{k-k_1+k_2}| - \Lambda) \Gamma_{\text{RG}}(k, k-k_1+k_2, k_3, k_4) \\ & + \int_{|\xi_{\mathbf{k}'}|=\Lambda} \frac{dk'}{v_{\mathbf{k}'}} \Gamma_{\text{RG}}(k_1, k_2; k_1-k_2+k', k') \frac{f(\xi_{k'} - f(\xi_{k_1-k_2+k'}))}{\xi_{k'} - \xi_{k_1-k_2+k'}} \theta(|\xi_{k_1-k_2+k'}| - \Lambda) \Gamma_{\text{RG}}(k_1-k_2+k', k'; k_3, k_4). \end{aligned}$$

The diagrammatic expression for the RG equation is shown in Fig.10. By solving the RG equation, parquet type scatterings are automatically included as shown in Fig.11. The present RG formulation is almost equivalent to Ward-Takahashi identity, which brings the relation between N and N+2 point vertex functions while we neglect the higher point vertex functions than 6-point vertex and 2-loop diagram, which gives self energy term [20]-[22].

Here, we comment that p-p channel scattering is negligibly small in the higher energy region. Therefore, we neglect the p-p channel scattering in the cRPA, while it gives significant contribution in lower energy region. For instance, perfect cancellation occurs between p-h and p-p loop in 1D system. Thus, we consider p-p channel in the RG equation. In contrast to the present fRG method, lower energy Green function ($|\xi_{\mathbf{k}}| < \Lambda$) is considered as well as on-shell one in the Wilson's RG method. The essence behind both RG method is the same.

Figure 10: 1-loop RG differential equation about 4-point vertex. The crossed red line represents electron propagator G with energy cutoff Λ , while the slashed line denotes on shell one.

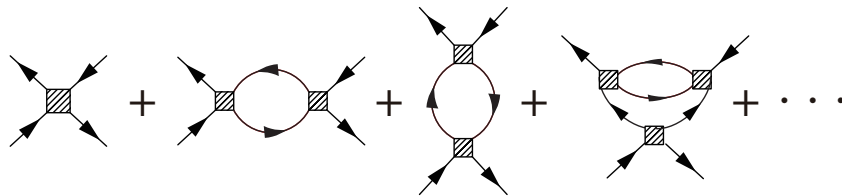


Figure 11: Parquet type diagrams included in the present fRG method.

Finally, we obtain renormalized 4-point vertex $\Gamma_{\text{RG}}(k_1, k_2; k_3, k_4)$ by solving the RG equation, numerically. The RG flow starts from $\Lambda = \Lambda_0$ to the low energy cutoff $\omega_c \ll T$. Here, we set $\Lambda_0 = 1.0$ ($<$ band width) as shown in Fig.8 (a) and use logarithmic energy scaling parameter:

$$\Lambda_l = \Lambda_0 e^{-l} \quad (l \geq 0). \quad (2.11)$$

It is verified that our main results do not change even in the case of $\Lambda_0 \sim W_{\text{band}}/2$.

Here, we discuss SU(2) symmetry and spin index of 4-point vertex function. In principle, to obtain physical quantity, it is enough to calculate only $\Gamma^{\uparrow\uparrow\uparrow\uparrow}$ due to the following reason. In general, the present Hamiltonian in the band basis can be written by

$$H = \sum_{k_i\sigma} \tilde{\Gamma}_{k_1k_2k_3k_4}^{\sigma\sigma\sigma\sigma} d_{k_1\sigma}^\dagger d_{k_2\sigma} d_{k_3\sigma} d_{k_4\sigma}^\dagger + \sum_{k_i\sigma\sigma'} \tilde{\Gamma}_{k_1k_2k_3k_4}^{\sigma\bar{\sigma}\sigma\bar{\sigma}} d_{k_1\sigma}^\dagger d_{k_2\bar{\sigma}} d_{k_3\sigma} d_{k_4\bar{\sigma}}^\dagger. \quad (2.12)$$

Then, the rotation of the spin space is given by the unitary transformation,

$$\begin{pmatrix} \alpha & -\beta \\ \beta^* & \alpha^* \end{pmatrix} \begin{pmatrix} d_\uparrow \\ d_\downarrow \end{pmatrix} = \begin{pmatrix} d_\uparrow \\ d_\downarrow \end{pmatrix} \quad (|\alpha|^2 + |\beta|^2 = 1). \quad (2.13)$$

Here, the Hamiltonian does not change under the rotation. Then, we obtain

$$\tilde{\Gamma}_{1234}^{\sigma\sigma\sigma\sigma} - \tilde{\Gamma}_{1324}^{\sigma\sigma\sigma\sigma} = \tilde{\Gamma}_{1234}^{\sigma\bar{\sigma}\sigma\bar{\sigma}} - \tilde{\Gamma}_{1324}^{\sigma\bar{\sigma}\sigma\bar{\sigma}}. \quad (2.14)$$

Therefore, $\Gamma_{\text{RG}}^{\uparrow\downarrow\uparrow\downarrow}$ is calculated from $\Gamma_{\text{RG}}^{\uparrow\uparrow\uparrow\uparrow}$. In addition, in the orbital basis, $\hat{\Gamma}_{\text{RG}}$ is uniquely decomposed into spin and charge channels,

$$\hat{\Gamma}_{\text{RG}}(k+q, k; k'+q, k') = \frac{1}{2}\Gamma_{\text{RG}}^{\text{S}}(k+q, k; k'+q, k')\vec{\sigma}_{\sigma\sigma'} \cdot \vec{\sigma}_{\rho'\rho} + \frac{1}{2}\Gamma_{\text{RG}}^{\text{C}}(k+q, k; k'+q, k')\delta_{\sigma\sigma'}\delta_{\rho'\rho}. \quad (2.15)$$

Note that $\hat{\Gamma}_{\text{RG}}$ in the orbital basis is obtained from that in the band basis by using unitary transformation $u_{lu}(\mathbf{k}) = \langle l, \mathbf{k} | u, \mathbf{k} \rangle$.

In some previous fRG study, Λ_0 is set larger than bandwidth W_{band} . In these cases, bare Coulomb interaction is used as the initial value. On the other hand, in our present fRG+cRPA study, $\Lambda_0 < W_{\text{band}}$, and the initial value is calculated by cRPA, which includes high energy processes without over counting [23]. In addition, there are difference on the condition of momentum conservation $k_1 + k_4 \simeq k_2 + k_3$ for the 4-point vertex explained in Appendix A. The present fRG+cRPA method has some merits listed as follows;

- (i) High energy scatterings are accurately considered within RPA by using fine \mathbf{k} -meshes ($\mathbf{k}_x \times \mathbf{k}_y = 128 \times 128$). This is justified when VC is not so large at high energy. On the other hand, conventional RG method cause numerical errors from the violation of \mathbf{k} -conservation at low energy region.
- (ii) Van-Vleck scattering, which is important in multi orbital SCES, is taken into account. Especially, these process contribute to the development of orbital fluctuations.

● key facts ●

- * 1 4-point vertex function is calculated by fRG+cRPA method.
- * 2 In the fRG method, parquet type 4-point vertex is automatically generated.
- * 3 High energy scattering is considered by cRPA, which gives initial value for RG equation.
- * 4 fRG+cRPA method brings great merit compared with previous fRG without cRPA.

2.3 3-point vertex and p-p (p-h) fluctuations

Here, we formulate the d -electrons susceptibility within the fRG+cRPA method. The definition of charge (spin) channel (ch) susceptibility due to p-h excitation is given by

$$\chi_{ll'mm'}^{c(s)}(q) = \int_0^\beta d\tau \frac{1}{2} \langle A_{ll'}^{c(s)}(\mathbf{q}, \tau) A_{m'm}^{c(s)}(-\mathbf{q}, 0) \rangle e^{i\omega_l \tau}, \quad (2.16)$$

$$A_{ll'}^{c(s)}(\mathbf{q}) \equiv \sum_{\mathbf{k}} (d_{\mathbf{k}l'\uparrow}^\dagger d_{\mathbf{k}+q\uparrow} + (-) d_{\mathbf{k}l'\downarrow}^\dagger d_{\mathbf{k}+q\downarrow}) \quad (2.17)$$

In the framework of fRG theory, the p-h susceptibility is calculated by solving the differential equation;

$$\frac{d}{d\Lambda} \chi_{\text{RG}}^{c(s)}(q) = T \sum_{\mathbf{k}} \left[\frac{d}{d\Lambda} \tilde{G}(\mathbf{k}) \tilde{G}(\mathbf{k}+q) \right] R^{c(s)}(q; \mathbf{k}, \mathbf{k}+q) R^{c(s)}(-q; \mathbf{k}+q, \mathbf{k}) \quad (2.18)$$

$$\frac{d}{d\Lambda} R^{c(s)}(q; k, k') = -T \sum_{k''} \left[\frac{d}{d\Lambda} \tilde{G}(k'') \tilde{G}(k'' + q) \right] R^{c(s)}(q; k'', k'' + q) \Gamma_{\text{RG}}^{c(s)}(k, k'' + q, k', k''), \quad (2.19)$$

where $R^{c(s)}$ is the 3-point vertex diagrammatically expressed in Fig.12. We simply put the initial value

Figure 12: (a) RG equation for p-h susceptibility in the fRG theory. The shaded triangles show 3-point vertex function. (b) RG equation for 3-point vertex function.

for 3-point vertex; $\hat{R} = \hat{1}$. Then, obtained p-h susceptibility in the orbital basis with fully considered VC is given by

$$\hat{\chi}_{\text{RG}}^{c(s)}(q) = \hat{\Phi}^{c(s)}(q) [\hat{1} - \hat{U}^{c(s)} \hat{\Phi}^{c(s)}(q)]^{-1} \quad (2.20)$$

$$\hat{\Phi}^{c(s)}(q) = -T \sum_n \hat{G}(k+q) \hat{G}(k) \hat{\Lambda}^{c(s)}(k+q, k), \quad (2.21)$$

where Λ is VC for irreducible susceptibility due to many body effects beyond RPA, which we call χ -VC. In the present fRG study, χ -VC is automatically calculated by solving the renormalization equation.

To study SC phase, we introduce the SC susceptibilities by p-p excitation in the band basis, which is defined as

$$\chi_{t(s)}^{\text{SC}} = \frac{1}{2} \int_0^\beta d\tau \langle B_{t(s)}^\dagger(\tau) B_{t(s)}(0) \rangle, \quad \left(B_{t(s)} \equiv \sum_{\mathbf{k}} \Delta_{t(s)}(\mathbf{k}) d_{\mathbf{k}\uparrow} d_{-\mathbf{k}\uparrow(\downarrow)} \right) \quad (2.22)$$

where spin triplet (singlet) gap: $\Delta_{t(s)}(\mathbf{k})$ is uniquely determined so as to maximize the SC susceptibilities.

Here, we show numerical results at $T = 5 \times 10^{-4}$ and low energy cutoff $\Lambda = 0.01T$ (i.e., $l = \ln(\Lambda_0/0.01T)$). The strength of correlation parameters are set at $(U, J/U) = (3.10, 0.08)$ in Figs.13(a) and (b), referring to the black circle in 'U vs J/U phase diagram' given by Fig.13 (c). We obtain large quadrupole susceptibility as shown in Fig.13(a), which is given by

$$\chi_{x^2-y^2}^c(\mathbf{q}) = \sum_{l,m} (-1)^{l+m} \chi_{llmm}^c(\mathbf{q}). \quad (2.23)$$

The quadrupole susceptibility diverge when orbital polarization $n_{xz} - n_{yz}$ emerges. In Fig.13(b), obtained total spin susceptibility is plotted, which is defined as

$$\chi^s(\mathbf{q}) = \sum_{l,m} \chi_{llmm}^s(\mathbf{q}). \quad (2.24)$$

Both $\chi^s(\mathbf{q})$ and $\chi_{x^2-y^2}^c(\mathbf{q})$ has the maximum value around the major nesting at $\mathbf{Q} = (2\pi/3, 2\pi/3)$, There are simple relation $\chi^s(\mathbf{Q}) \approx \chi_{x^2-y^2}^c(\mathbf{Q})$. However, orbital fluctuations are quite weak $\chi^c(\mathbf{Q}) \ll \chi^s(\mathbf{Q})$ within RPA. Therefore, we conclude that the orbital fluctuations are strongly enhanced by many body effects due to the χ -VC considered in the fRG method. From the obtained phase diagram given in Fig.13(c), spin triplet and singlet SC paring states are realized below orbital and magnetic ordered phase for wide range parameter region, respectively. Here, the boundary of the orbital and magnetic ordered phase correspond to the broken lines, while the solid lines represents spin triplet and singlet SC phase. The relation $\chi^s(\mathbf{Q}) = \chi_{x^2-y^2}^c(\mathbf{Q})$ holds on the purple colored dotted line.

Obtained TSC gap $\Delta_t(k)$ belongs to the E_u representation and it is written as $\Delta_{t,x}(\mathbf{k}), \Delta_{t,y}(\mathbf{k}) \propto \sin 3k_x, \sin 3k_y$. Spin singlet SC gap $\Delta_s(k)$ is in the A_{1g}, B_{1g} symmetry. We found that the strong orbital fluctuations develop at $J/U \lesssim 0.1$. This value is almost equal to $J/U = 9.5 \times 10^{-2}$ obtained in FeSe by the first principles study.

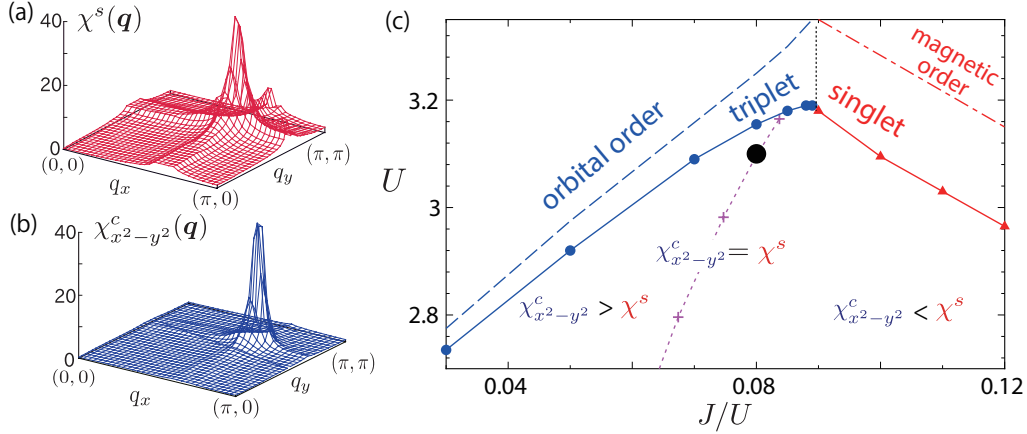


Figure 13: (a) Momentum dependence of total spin susceptibility $\chi^s(\mathbf{q})$ and (b) that of quadrupole susceptibility $\chi_{x^2-y^2}^c(\mathbf{q})$, which show strong peak around $\mathbf{q} \approx (2\pi/3, 2\pi/3)$. (c) Low temperature phase diagram calculated by fRG+cRPA study.

● key facts

- * 1 Both p-h and p-p susceptibilities are obtained by solving fRG equation for 3-point vertex.
- * 2 Quadrupole orbital fluctuations are enhanced by χ -VC in fRG method.
- * 3 Triplet SC state emerges near the boundary of orbital and spin ordered phases.

2.4 Superconductivity by fRG+cRPA

Here, we analyze the origin of the SC state based on the linearized gap equation with pairing interaction by the fRG+cRPA method [24]. The band basis gap equation on the Fermi surface is written by

$$\lambda_{t(s)} \Delta_{t(s)}(\mathbf{k}) = - \int \frac{d\mathbf{k}'}{v_{\mathbf{k}'}} V_{t(s)}^{\omega_c}(\mathbf{k}, \mathbf{k}') \Delta_{t(s)}(\mathbf{k}') \ln \frac{1.13\omega_c}{T}, \quad (2.25)$$

Here, the momenta \mathbf{k}, \mathbf{k}' is on the Fermi surface. $v_{\mathbf{k}} (= d\xi_{\mathbf{k}}/dk)$ is Fermi velocity. Here, we only consider the gap function with even frequency. Then, triplet (singlet) SC gap has odd (even) parity. $\lambda_{t(s)}$ gives eigenvalue for triplet (singlet) SC. $V_{t(s)}^{\omega_c}$ is effective SC pairing interaction by fRG+cRPA with low energy cutoff; $\Lambda_l = \omega_c$ ($l = \ln(\Lambda_0/\omega_c)$). We set the low cutoff ω_c so as to satisfy $\omega_c > T$. Then, p-h susceptibilities $\hat{\chi}^{s,c}(\mathbf{q})$ saturate and only p-p fluctuations drastically develop when $\Lambda_l < \omega_c$. In the derivation of Eq.(2.25), we used the general relation

$$\int_{-\omega_c}^{\omega_c} d\epsilon_{\mathbf{k}'} \frac{1}{2\epsilon_{\mathbf{k}'}} \text{th}(\epsilon_{\mathbf{k}'}/2T) = \ln(1.13\omega_c/T). \quad (2.26)$$

The SC pairing interaction is directly calculated from 4-point vertex Γ_{RG} till the lower-energy cutoff $\Lambda_l = \omega_c$ written as

$$V_{t,\text{RG}}(\mathbf{k}, \mathbf{k}') = -\frac{1}{4}\Gamma_{\text{RG}}^s(\mathbf{k}, \mathbf{k}'; -\mathbf{k}', -\mathbf{k}) - \frac{1}{4}\Gamma_{\text{RG}}^c(\mathbf{k}, \mathbf{k}'; -\mathbf{k}', -\mathbf{k}), \quad (2.27)$$

$$V_{s,\text{RG}}(\mathbf{k}, \mathbf{k}') = \frac{3}{4}\Gamma_{\text{RG}}^s(\mathbf{k}, \mathbf{k}'; -\mathbf{k}', -\mathbf{k}) - \frac{1}{4}\Gamma_{\text{RG}}^c(\mathbf{k}, \mathbf{k}'; -\mathbf{k}', -\mathbf{k}). \quad (2.28)$$

Here, we set $\omega_c = 12T = 6 \times 10^{-3}$. Obtained pairing interaction $V_{t(s),\text{RG}}$ automatically include various scattering processes as listed in Fig.14(a). For instance, the single- and crossing-fluctuation-exchange terms are written by type-A and B, respectively, while p-p ladder term is shown as Type-C, which is expected to be small when $\omega_c \gg T_c$. The black triangle shows the vertex correction for SC paring neglected in Migdal-Eliashberg (ME) scheme, which we call U -VC. Typical example of U -VC is represented in Fig.

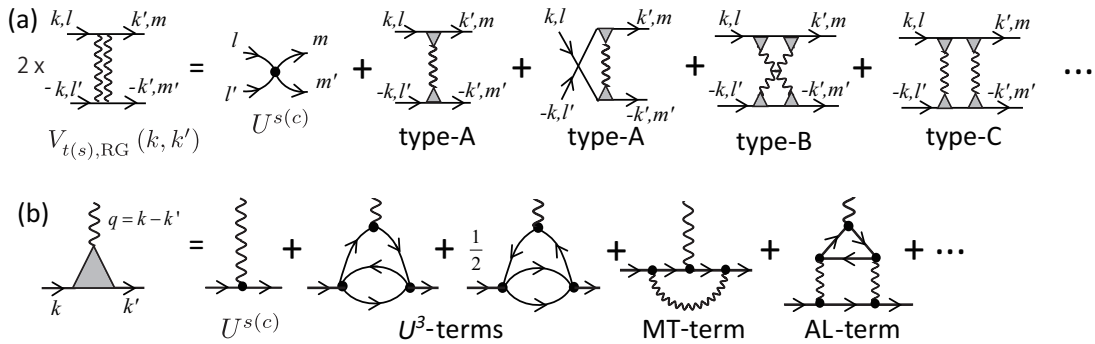


Figure 14: (a) Effective SC pairing interaction given by fRG method. Type-A(B) shows single (crossing)-fluctuation-exchange term. Type-C is the p-p ladder term. The black triangle shows U -VC beyond ME-scheme. (b) Typical diagrams for the U -VC. Double counting is carefully avoided.

14(b). To study general properties of VC, fRG is useful since both χ - and U -VC are taken into account in the equal footings within the parquet type scattering. This is one of the big merits in fRG method.

Hereafter, we set $U = 3.10$, $J/U = 0.08$ and show some numerical results. We solve SC gap equation in Eq.(2.25) by using the pairing interaction $\hat{V}_{t(s),RG}$ with U -VC given as Eqs.(2.27)-(2.28). Figures 15(a) and (b) are obtained gap functions of spin triplet SC $\Delta_t(\theta)$ and singlet SC $\Delta_s(\theta)$, where θ is angle of Fermi surfaces. Eigenvalues are $\lambda_t = 0.47$ and $\lambda_s = 0.26$. We get triplet (singlet) gap function in E_{1u} (A_{1g}) representation, which is consistent with the SC fluctuations given by Eq.(2.22) based on the fRG+cRPA. Therefore, present gap equation is essentially equivalent to fRG method. In addition, averaged SC pairing interaction is derived by using the obtained solution of the gap equation;

$$\bar{\lambda}_{t(s)} = \frac{\int \frac{d\mathbf{k}}{v_{\mathbf{k}}} \int \frac{d\mathbf{k}'}{v_{\mathbf{k}'}} V_{t(s)}^{\omega_c}(\mathbf{k}, \mathbf{k}') \Delta_{t(s)}(\mathbf{k}') \Delta_{t(s)}(\mathbf{k})}{\int \frac{d\mathbf{k}}{v_{\mathbf{k}}} \Delta_{t(s)}(\mathbf{k}) \Delta_{t(s)}(\mathbf{k})}, \quad (2.29)$$

where the transition temperature T_c is written as $T_{c,t(s)} \simeq 1.13\omega_c \exp(-1/\bar{\lambda}_{t(s)})$. In Fig.15(c), obtained gap function $\bar{\lambda}_{t(s)}$ as a functions of Λ_l . Here, the gap structures are fixed to that in Figs.15(a), (b). We find that scaling curve of $\bar{\lambda}_{t(s)}$ almost saturates when the scaling energy Λ_l is lower than T . The vertical dotted line corresponds to T in Fig.15(c) and (d). The relation $\bar{\lambda}_t \sim 3\bar{\lambda}_s$ holds, irrespective of $\chi^s(\mathbf{Q}) \sim \chi_{x^2-y^2}^c(\mathbf{Q})$.

In order to study the essential properties of U -VC, effective SC interaction within ME scheme is also calculated. In this case, U -VC is dropped. For this purpose, $\hat{\chi}_{RG}^{c(s)}$ with cutoff $\Lambda_l = \omega_c$ is used to form the SC interaction. By using the $\hat{\chi}_{RG}^{c(s)}$, the pairing interaction is defined as,

$$\hat{V}_{s(t),\chi}(\mathbf{k}, \mathbf{k}') \equiv \frac{3}{4} \hat{\Gamma}_{\chi}^s(\mathbf{k}, \mathbf{k}') \left(-\frac{1}{4} \hat{\Gamma}_{\chi}^s(\mathbf{k}, \mathbf{k}') \right) - \frac{1}{4} \hat{\Gamma}_{\chi}^c(\mathbf{k}, \mathbf{k}') - \left(\frac{1}{2} \hat{U}^s \right) \quad (2.30)$$

$$\Gamma_{\chi, ll' mm'}^s(\mathbf{k}, \mathbf{k}') = \left(\hat{U}^s + \hat{U}^s \hat{\chi}_{RG}^s(\mathbf{k} - \mathbf{k}') \hat{U}^s \right)_{ll' mm'} - \left(\frac{1}{2} \hat{U}^c \hat{\chi}_{RG}^c(\mathbf{k} + \mathbf{k}') \hat{U}^c - \frac{1}{2} \hat{U}^s \hat{\chi}_{RG}^s(\mathbf{k} + \mathbf{k}') \hat{U}^s \right)_{lml'm'} \quad (2.31)$$

$$\Gamma_{\chi, ll' mm'}^c(\mathbf{k}, \mathbf{k}') = \left(\hat{U}^c + \hat{U}^c \hat{\chi}_{RG}^c(\mathbf{k} - \mathbf{k}') \hat{U}^c \right)_{ll' mm'} - \left(\frac{1}{2} \hat{U}^c \hat{\chi}_{RG}^c(\mathbf{k} + \mathbf{k}') \hat{U}^c + \frac{3}{2} \hat{U}^s \hat{\chi}_{RG}^s(\mathbf{k} + \mathbf{k}') \hat{U}^s \right)_{lml'm'} \quad (2.32)$$

In this case, U -VC is neglected in the SC pairing interaction, while χ -VC is included. By using $V_{s(t),\chi}$, we solve linearized gap equation. Effective interaction is plotted in Fig.15(d). Here, $\Delta_{t(s)}(\mathbf{k})$ is fixed as well as Fig.15(c). Note that similar solution is obtained even if $V_{t(s),\chi}$ is used for SC pairing interaction. From the present result, $3\bar{\lambda}_t \sim \bar{\lambda}_s$ holds. Therefore, we conclude that $\bar{\lambda}_t \gg \bar{\lambda}_s$ emerges thanks to U -VC. Thus, triplet SC is mediated by the important role of U -VC.

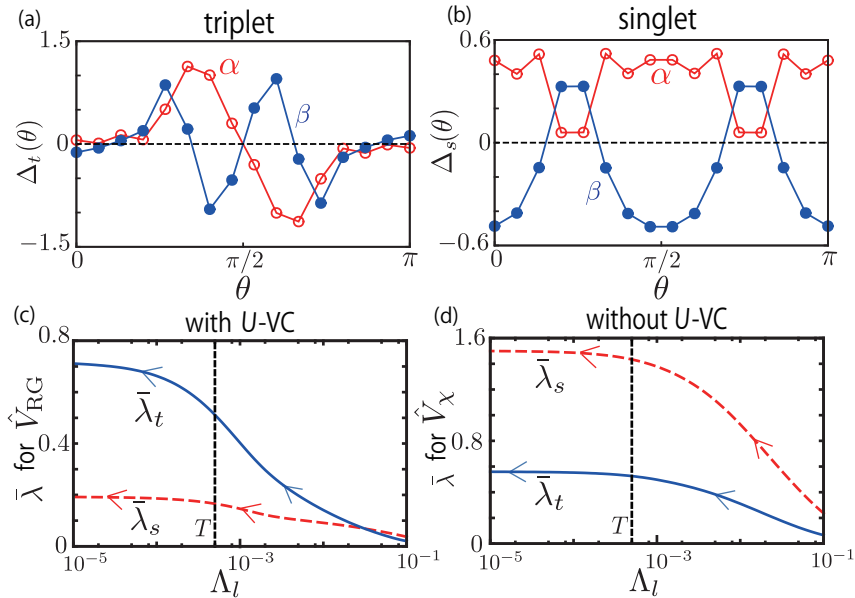


Figure 15: (a) E_{1u} -type triplet SC gap function and (b) A_{1g} -type singlet SC gap function on the Fermi surface. Averaged SC pairing interaction for (c) $V_{t(s),\text{RG}}$ and (d) $V_{t(s),\chi}$ as a functions of Λ_l .

● key facts

- * 1 We compare 2-types of SC pairing interaction. One of that is fully renormalized 4-point vertex. The another one is given by χ_{RG} without U -VC.
- * 2 Triplet SC state is stabilized by the significant roles of U -VC.

Discussion

2.5 Analysis of the U -VC

In more detail, to understand the origin of U -VC, we focus on the momentum dependence of many body effects. Figures 16(a)-(d) show the obtained inter-band pairing interactions, which means that both \mathbf{k} and \mathbf{k}' are on the same Fermi surface. Note that intra-band interaction is much smaller than inter-band one. Here, i_α and i_β are patch index on Fermi surface α and β , respectively. Solid ellipses in Fig.8(c) corresponds to the major nesting vector $(i_\alpha, i_\beta) = (6, 37), (8, 38), (10, 39)$, depicted by the arrows at $\mathbf{k} - \mathbf{k}' \approx \mathbf{Q} \equiv (2\pi/3, 2\pi/3)$. We find that $\Gamma_\chi^{s(c)}(\mathbf{k}, \mathbf{k}')$ has positive value at $\mathbf{k} - \mathbf{k}' \approx \mathbf{Q}$ as shown in Figs.16(a) and (b). These peaks corresponds to that of $\chi^s(\mathbf{q})$ and $\chi_{x^2-y^2}^c(\mathbf{q})$. However, the relation $\Gamma_\chi^s(\mathbf{k}, \mathbf{k}') \gg \Gamma_\chi^c(\mathbf{k}, \mathbf{k}')$ holds. Therefore, the repulsive interaction due to Γ_χ^s is much larger than attractive interaction due to Γ_χ^c for spin singlet SC pairing. For this reason, the relation $\bar{\lambda}_s \gg \bar{\lambda}_t$ holds if we neglect the U -VC.

On the other hand, above mentioned situation will drastically change by considering U -VC. Figures 16(c) and (d) show $\Gamma_{\text{RG}}^s(\mathbf{k}, \mathbf{k}')$ and $\Gamma_{\text{RG}}^c(\mathbf{k}, \mathbf{k}')$ in the presence of U -VC. Both spin and charge channel interaction form large positive values at $\mathbf{k} - \mathbf{k}' \approx \mathbf{Q}$. Moreover, $\Gamma_{\text{RG}}^c(\mathbf{k}, \mathbf{k}')$ is larger than $\Gamma_{\text{RG}}^s(\mathbf{k}, \mathbf{k}')$. Therefore, the spin (charge) channel pairing interaction is suppressed (enhanced) by introducing the U -VC. As a result, $\bar{\lambda}_t \simeq \bar{\lambda}_s$ is satisfied by considering U -VC correctly as seen in Fig.15(c). We comment that large negative value at $(i_\alpha, i_\beta) = (6 + 16, 37), (8 + 16, 38), (10 + 16, 39)$ comes from $\hat{\chi}^c(\mathbf{k} + \mathbf{k}')$ at $\mathbf{k} + \mathbf{k}' \approx \mathbf{Q}$ given by 3rd terms of the rhs in Eq.(2.31) and (2.32).

Figure 16(e) shows the ratio of $\Gamma_\chi^c(\mathbf{k}, \mathbf{k}')/\Gamma_\chi^s(\mathbf{k}, \mathbf{k}')$ and $\Gamma_{\text{RG}}^c(\mathbf{k}, \mathbf{k}')/\Gamma_{\text{RG}}^s(\mathbf{k}, \mathbf{k}')$ at $\mathbf{k} - \mathbf{k}' \approx \mathbf{Q}$ as a functions of U . In weakly correlated region around $U \approx 0$, the ratio reaches -1 , which means $\hat{U}^{s(c)} \approx +(-)U$ derived from Eq.(2.4). Therefore, the bare Coulomb interaction is dominant over p-h fluctuations in weak coupling region. In contrast, the ratio becomes large positive value at $U \gtrsim 2$ for Γ_{RG} whereas

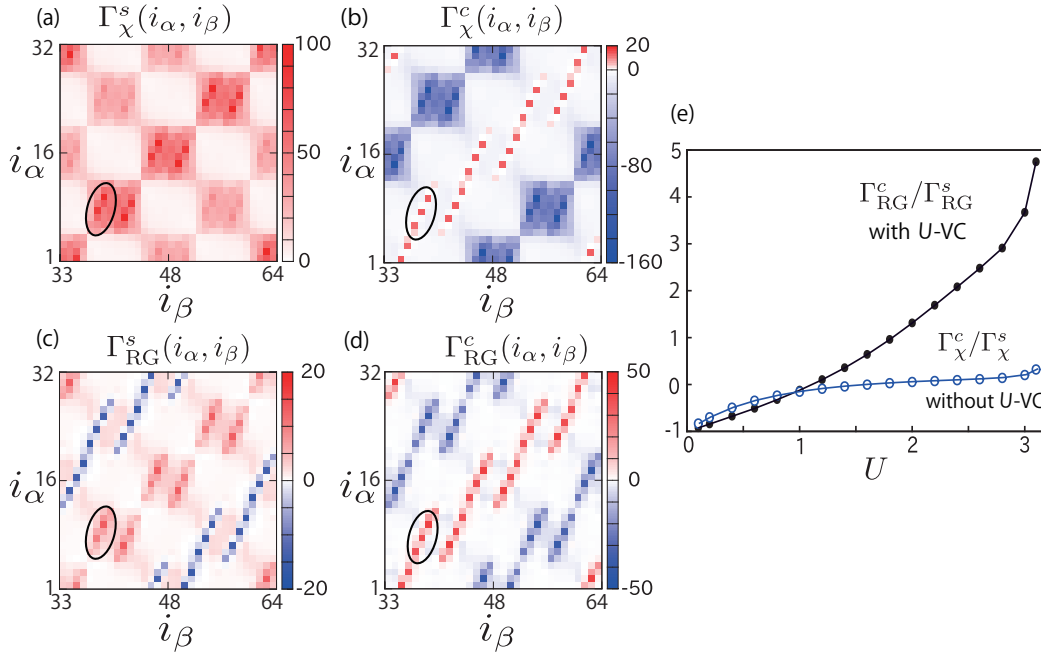


Figure 16: Inter-band SC pairing interactions for (a) spin and (b) charge channel without U -VC. That for (c) spin and (d) charge channel with U -VC. (i_α, i_β) denotes patch index on Fermi surface α and β . (e) The ratio $\Gamma_\chi^c/\Gamma_\chi^s$ and $\Gamma_{RG}^c/\Gamma_{RG}^s$ as a functions of U . They are averaged over the ellipsoidal area.

that for Γ_χ remains small. Thus, $\Gamma_{RG}^{c(s)}$ is enhanced (suppressed) thanks to the U -VC in the strongly correlated region.

In conclusion, the spin (charge) channel of SC paring interaction is drastically suppressed (enlarged) by the U -VC. We comment that the momentum dependence of $\Gamma_{RG}(\mathbf{k}, \mathbf{k}')$ and $\Gamma_\chi(\mathbf{k}, \mathbf{k}')$ are very similar. It reveal that single-fluctuation-exchange term of Type-A is quite important, since multi-fluctuation-exchange process of type-B give different momentum dependence. In the present study, we consider χ -VC and U -VC on the same footing. As a result, we revel that the χ -VC enhance the orbital fluctuation, while U -VC enhance the SC paring interaction induced by orbital fluctuation.

● key facts

- * 1 Single-fluctuation-exchange process brings dominant contribution to SC paring interaction.
- * 2 Charge (spin) channel of SC paring interaction is enhanced (suppressed) by U -VC.

2.6 Diagrammatic method vs fRG analysis

In this section, we perform diagrammatic analysis to understand the microscopic origin of the SC phase diagram obtained in Fig.13. In particular, we consider the U -VC given by MT and AL terms in Fig.14(b), which give the 1st and 2nd order of the fluctuation, respectively. The schematic expression of charge (spin) channel U -VC is given by

$$U^{c,MT}(q) \propto \{\chi^c(q) + 3\chi^s(q)\} \quad U^{s,MT}(q) \propto \{\chi^c(q) - \chi^s(q)\} \quad (2.33)$$

$$U^{c,AL}(q) \propto \sum_p \{\chi^c(q+p)\chi^c(q) + 3\chi^s(q+p)\chi^s(q)\} \quad U^{s,AL}(q) \propto \sum_p \{2\chi^s(q+p)\chi^c(q)\} \quad (2.34)$$

The detailed expression is given in Appendix A. Effective enhancement factor caused by U -VC for the paring interaction is defined by

$$r^{c(s)} \equiv \left(\frac{U^{c(s)}(\mathbf{k}, \mathbf{k}') + U^{c(s),AL}(\mathbf{k}, \mathbf{k}') + U^{c(s),MT}(\mathbf{k}, \mathbf{k}')}{U^{c(s)}(\mathbf{k}, \mathbf{k}')} \right)^2 \quad (2.35)$$

Figure 17(a) shows obtained $r^{c(s)}$ at $\mathbf{k} - \mathbf{k}' \approx \mathbf{Q}$ as a function of the spin Stoner factor α_S . Note that α_S is defined as the largest eigenvalue of $\hat{U}^s \hat{\chi}^0(\mathbf{q})$ and $\chi^s(\mathbf{Q}) \propto (1 - \alpha_S)^{-1}$. Thus, α_S reaches unity at the magnetic transition temperature. As shown in Fig.17(a), r^c gradually increases around the magnetic QCP ($\alpha_S \approx 1$). For this reason, we conclude that the strong enhancement comes from orbital channel of AL-type VC. AL term is approximately given by $\sum_{\mathbf{q}} \chi^s(\mathbf{q} + \mathbf{Q}) \chi^s(\mathbf{q}) \sim (1 - \alpha_S)^{-1}$ as given in Eq.(2.34). In spite of that, $U^{s,AL}$ is negligibly small since it is proportional to $\sum_{\mathbf{q}} \chi^s(\mathbf{q}) \chi^c(\mathbf{q} + \mathbf{Q})$. r^s is suppressed by U -VC where $r^s \ll 1$. Then, we verified that the suppression mainly comes from the $O(U^3)$ -term as shown in Fig.17(c). Moreover, this $O(U^3)$ -term is significant in multi orbital SCES since it is scaled as $\sim (2N_{\text{orb}} - 1)$. N_{orb} is the number of orbitals. Note that double counting due to the $O(U^3)$ -terms is carefully eliminated.

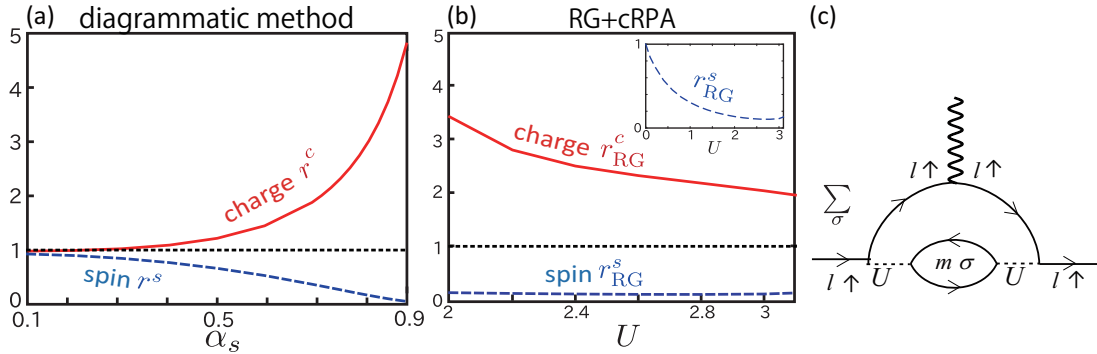


Figure 17: Enhancement factor for SC pairing interaction by (a) diagrammatic method and (b) fRG+cRPA. (c) $O(U^3)$ -term scaled as $\sim (2N_{\text{orb}} - 1)$. $U = U', J = 0$ is assumed for simplicity.

Figure 17(b) shows enhancement factor for SC pairing interaction directly obtained by fRG+cRPA, which is defined as

$$r_{\text{RG}}^{c(s)} \equiv \frac{\Gamma_{\text{RG}}^{c(s)}(\mathbf{k}, \mathbf{k}')}{\Gamma_{\chi}^{c(s)}(\mathbf{k}, \mathbf{k}')} \quad (2.36)$$

$r_{\text{RG}}^{c(s)}$ comes to be the square of U -VC at $U \gtrsim 2.5$ where single-fluctuation-exchange term dominates over the others. The obtained relations $r_{\text{RG}}^c \gg 1$, $r_{\text{RG}}^s \ll 1$ are consistent with the results based on the diagrammatic method. Note that r_{RG}^c diverges at $U \approx 1.5$ since Γ_{χ}^c changes its sign as shown in Eq.(2.32).

● key facts

- * 1 We compare the U -VC obtained by fRG+cRPA with that by diagrammatic calculation.
- * 2 Charge channel pairing interaction is strongly enhanced by AL-type U -VC.
- * 3 Spin channel pairing interaction is suppressed by $O(U^3)$ -term.

Conclusion

In the Sec.2, we studied two-orbital Hubbard model by performing the fRG+cRPA method to understand fundamental properties of many body effects beyond RPA+ME theory. As a result, we found that orbital-fluctuation-mediated SC phase emerges due to the significant roles of χ -VC and U -VC based on the fRG+cRPA and diagrammatic analysis.

Especially, χ -VC enlarges the orbital fluctuations and orbital ordered phase appears in the realistic parameter region, while only spin ordered phase emerges within RPA study. Thus, we conclude that χ -VC beyond RPA is important in multi-orbital SCES. In addition, to go beyond ME scheme, we analyze SC gap equation by considering VC in SC pairing interaction, which is called U -VC. Thanks to the U -VC, orbital-fluctuation-mediated SC interaction is magnified in the strong coupling regime. In particular, AL-type U -VC brings major contribution to the enhancement, which is verified by comparing the result

of fRG with that of diagrammatic method. On the other hand, spin-fluctuation-mediated SC interaction is significantly suppressed by $O(U^3)$ -term. This suppression does not contradict development of spin fluctuations in multi orbital SCES since U -VC comes to be important only in low energy region, while p-h fluctuations are calculated by performing summation along wide energy range. Therefore, $\chi^s(\mathbf{q})$ develop from high energy process in renormalization, whereas U -VC is enlarged at low energy region.

We also revealed that the significant contribution in forming the Cooper pairs comes from the single-fluctuation-exchange term, since obtained momentum dependence was explained consistently for both $\Gamma_{\text{RG}}^{s(c)}(\mathbf{k}, \mathbf{k}')$ and $\Gamma_{\chi}^{s(c)}(\mathbf{k}, \mathbf{k}')$. On the other hand, absolute values of them were quite different. Therefore, significance of U -VC is clearly verified. As a result, SC phase induced by orbital fluctuations will appear in various multiorbital SCES, such as in Fe-, Ru-based and organic superconductor.

Also, our study predict that attractive pairing interaction mediated by electron-phonon coupling will be enhanced by charge channel U -VC. For instance, T_c of single layer FeSe can be increased.

The main results of the present study are summarized as follows;

- (i) Based on the fRG+cRPA study, we revealed that many body effects beyond RPA+ME play important roles to understand the orbital ordered phase and SC phase in multiorbital SCES.
- (ii) Orbital-fluctuation-mediated TSC phase appear in the presence of moderate orbital and spin fluctuations ($\chi^s \approx \chi^c$).
- (iii) Orbital fluctuations develop due to the enhancement factor given by χ -VC beyond RPA study.
- (iv) Single-fluctuation-exchange term with AL-type U -VC mainly contribute to the orbital fluctuation mediated SC paring.

References

- [1] R. Tazai, Y. Yamakawa, T. Tsuchiisu, H. Kontani, Phys. Rev. B **94**, 115155 (2016).
- [2] N. E. Bickers and S. R. White, Phys. Rev. B **43**, 8044 (1991).
- [3] S. Onari and H. Kontani, Phys. Rev. Lett. **109**, 137001 (2012).
- [4] S. Onari, Y. Yamakawa and H. Kontani, Phys. Rev. Lett. **112**, 187001 (2014).
- [5] Y. Yamakawa, S. Onari and H. Kontani, Phys. Rev. X **6**, 021032 (2016).
- [6] M. Tsuchiizu, Y. Ohno, S. Onari, and H. Kontani, Phys. Rev. Lett. **111**, 057003 (2013).
- [7] M. Tsuchiizu, Y. Yamakawa, S. Onari, Y. Ohno, and H. Kontani, Phys. Rev. B **91**, 155103 (2015).
- [8] A.P. Mackenzie and Y. Maeno, Rev. Mod. Phys. **75**, 657 (2003).
- [9] Y. Maeno, S. Kittaka, T. Nomura, S. Yonezawa, and K. Ishida, J. Phys. Soc. Jpn. **81**, 011009 (2012).
- [10] M. Sigrist, Prog. Theor. Phys. Suppl. **160**, 1 (2005).
- [11] K. Ishida, H. Mukuda, Y. Kitaoka, K. Asayama, Z. Q. Mao, Y. Mori, and Y. Maeno, Nature **396**, 658 (1998).
- [12] T. Nomura and K. Yamada, J. Phys. Soc. Jpn. **69**, 3678 (2000); T. Nomura and K. Yamada, J. Phys. Soc. Jpn. **71**, 1993 (2002).
- [13] Q. H. Wang, C. Platt, Y. Yang, C. Honerkamp, F. C. Zhang, W. Hanke, T. M. Rice and R. Thomale, Europhys. Lett. **104**, 17013 (2013).
- [14] S. Raghu, A. Kapitulnik and S. A. Kivelson, Phys. Rev. Lett. **105**, 136401 (2010).
- [15] T. Scaffidi, J. C. Romers, and S. H. Simon, Phys. Rev. B **89**, 220510 (2014).
- [16] I. A. Firmo, S. Lederer, C. Lupien, A. P. Mackenzie, J. C. Davis, and S. A. Kivelson, Phys. Rev. B **88**, 134521 (2013).
- [17] T. Takimoto, Phys. Rev. B **62**, R14641(R) (2000).
- [18] M. Braden, Y. Sidis, P. Bourges, P. Pfeuty, J. Kulda, Z. Mao, and Y. Maeno, Phys. Rev. B **66**, 064522 (2002).
- [19] W. Metzner, M. Salmhofer, C. Honerkamp, V. Meden, and K. Schönhammer, Rev. Mod. Phys. **84**, 299 (2012).
- [20] C. J. Halboth and W. Metzner, Phys. Rev. Lett. **85**, 5162 (2000).
- [21] C. Honerkamp and M. Salmhofer, Phys. Rev. Lett. **87**, 187004 (2001); C. Honerkamp and M. Salmhofer, Phys. Rev. B **64**, 184516 (2001).
- [22] A. A. Abrikosov, L. P. Gorkov, and I. E. Dzyaloshinskii, *Methods of Quantum Field Theory in Statistical Physics*, (Dover, New-York, 1975).
- [23] M. Tsuchiizu, Y. Yamakawa, and H. Kontani, Phys. Rev. B **93**, 155148 (2016)
- [24] J. Reiss, D. Rohe, and W. Metzner, Phys. Rev. B **75**, 075110 (2007); J. Wang, A. Eberlein, and W. Metzner, Phys. Rev. B **89**, 121116(R) (2014).

3 Cooperation of el-ph and AFM fluctuations for SC state

Introduction

In this section, we study the microscopic origin of fully gapped s -wave SC phase near the magnetic QCP based on the beyond RPA+ME theory.

In general, it was believed that the spin fluctuations work as a repulsion for Cooper pairs in spin singlet SC and harmful for conventional BCS-like s -wave SC. On the other hand, recent improved experiments discovered that fully gapped s -wave SC phase without sign reversal can appear in some SCES near magnetic instability. Especially, high T_c s -wave state was observed in heavily electron-doped FeSe with $T_c \sim 100\text{K}$ [1, 2], and A_3C_{60} (A =K, Rb, Cs) with $T_c \sim 30\text{K}$ [3]. In these materials, el-ph interaction is expected to work as a glue of Cooper pairs as discussed in some previous researches in Refs. [4]-[10]. Even so, there remains important question; what brings high- T_c s -wave state against large spin fluctuations or why s -wave Cooper pairs survive against strong on-site Coulomb interaction. Another fundamental properties of these s -wave system is that they have orbital degrees of freedom. Therefore, it is naturally expected that SC pairing interaction of s -wave phase can be induced owing to orbital fluctuations as well as el-ph interaction.

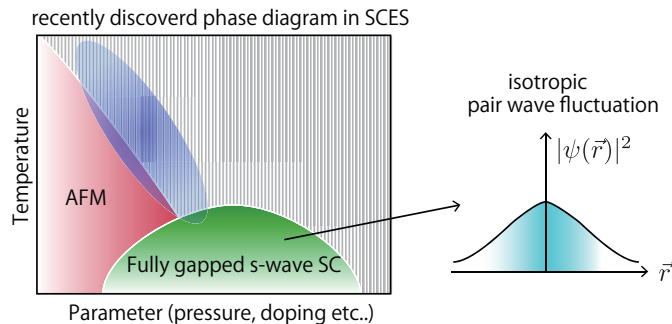


Figure 18: Recently discovered SC phase diagram in some multiorbital SCES.

To reveal the counter intuitive phenomena, we analyze multi orbital Hubbard-Holstein (HH) models by considering the VC and small el-ph coupling in the presence of strong magnetic fluctuations. As a result, we discover that phonon-mediated orbital fluctuations are enlarged due to χ -VC. In addition, charge-channel attractive interaction is magnified by U -VC, where it becomes significant when the interaction has crucial momentum dependence (non-local nature). Thanks to both χ - and U -VC, isotropic SC phase is mediated by small el-ph attraction near AFM-QCP against strong Coulomb repulsive interaction. In both VC, significant contribution comes from the AL-type scattering process, which comes from orbital-spin interference. Also, direct on-site Coulomb repulsion between intra-orbital Cooper pairs is drastically suppressed by “multi-orbital screening effect”. Our proposed pairing mechanism can explain characteristic SC phase diagram in typical s -wave compounds, such as Fe-based, A_3C_{60} as well as heavy fermion system CeCu_2Si_2 , which will be discussed in Sec.3.

Model

3.1 Hubbard-Holstein model (B_{1g} phonon)

Here, we start from two-orbital HH model on 2D square lattice;

$$\hat{H} = \hat{H}_{el} + \hat{H}_{ph},$$

$$\hat{H}_{el} = \sum_{\mathbf{k}\sigma} \sum_{lm} \xi_{\mathbf{k}}^{lm} d_{\mathbf{k}l\sigma}^\dagger d_{\mathbf{k}m\sigma} + \frac{1}{4} \sum_i \sum_{l'l'mm'} \sum_{\sigma\sigma'\rho\rho'} U_{l'l'mm'}^{\sigma\sigma'\rho\rho'} d_{i'l'\sigma'}^\dagger d_{i'l\sigma} d_{im\rho} d_{im'\rho'}^\dagger \quad (3.1)$$

where \hat{H}_{el} is composed of the kinetic and on-site Coulomb interaction term. i denotes index for lattice site, $d_{\mathbf{k}l\sigma}^\dagger$ ($d_{\mathbf{k}l\sigma}$) is the creation (annihilation) operator for d_{xz} or d_{yz} -electrons with wave number \mathbf{k} ,

orbital l , spin σ . $l, m = 1$ (2) corresponds to orbital index for d_{xz} (d_{yz}). We comment that our present results originates from multi-orbital nature of the electrons system. Therefore, the result slightly changes if we use 1-orbital HH model as shown in Appendix B. $\xi_{\mathbf{k}}^{lm}$ is defined as $\xi_{\mathbf{k}}^{11} = -2t \cos k_x - 2t'' \cos k_y$, $\xi_{\mathbf{k}}^{22} = -2t \cos k_y - 2t'' \cos k_x$, $\xi_{\mathbf{k}}^{12} = \xi_{\mathbf{k}}^{21} = -4t' \sin k_x \sin k_y$. After that, the hopping parameters are fixed at $(t, t', t'') = (1, 0.1, 0.1)$. Energy unit is $t = 1$, and the filling of d -electron takes $n_d = 2.30$. Obtained Fermi surfaces so called Fermi surface α and β , are given in Fig.22(a). θ is angle parameter for \mathbf{k} on each Fermi surfaces. Multi orbital on-site Coulomb interaction \hat{U} includes intra-orbital U , inter-orbital U' , Hund's coupling J , and pair hopping J' [10]. Spin- dependent bare 4-point vertex $\hat{U}^{\sigma\sigma'\rho\rho'}$ is uniquely decomposed into spin- and charge-channel as $\hat{U}^{\sigma\sigma'\rho\rho'} = \frac{1}{2}\hat{U}^s \vec{\sigma}_{\sigma\sigma'} \cdot \vec{\sigma}_{\rho'\rho} + \frac{1}{2}\hat{U}^c \delta_{\sigma,\sigma'} \delta_{\rho',\rho}$. $\hat{U}^{s(c)}$ denotes spin (charge) channel of 4-point vertex function. The detailed explanation for the Coulomb interaction was explained in Sec.2.

In the present study, we consider the effective el-ph interaction in B_{1g} symmetry, which is given by

$$\hat{H}_{\text{ph}} = \omega_D \sum_i b_i^\dagger b_i + \eta \sum_i (b_i^\dagger + b_i)(\hat{n}_i^{xz} - \hat{n}_i^{yz}), \quad (3.2)$$

where \hat{n}_i^l is quantum operator for electrons number with orbital l . Phonon creation (annihilation) operator is written by b_i^\dagger (b_i). Coefficient η denotes coupling constant between d -electrons and B_{1g} -phonon. ω_D is Debye frequency of phonon. Then, retarded interaction via el-ph coupling is given by

$$V = -g(\omega_j) \sum_i (\hat{n}_i^{xz} - \hat{n}_i^{yz})(\hat{n}_i^{xz} - \hat{n}_i^{yz}) \quad \left(g(\omega_j) = g \frac{\omega_D^2}{\omega_D^2 + \omega_j^2} \right) \quad (3.3)$$

where $g \equiv \frac{2\eta^2}{\omega_D}$ (> 0) and $\omega_j = 2j\pi T$ is the Boson Matsubara frequency. We show schematic expression of possible B_{1g} phonon in Fig.19(b). Note that $n_{xz} \neq n_{yz}$ holds if the B_{1g} -orbital order occur.

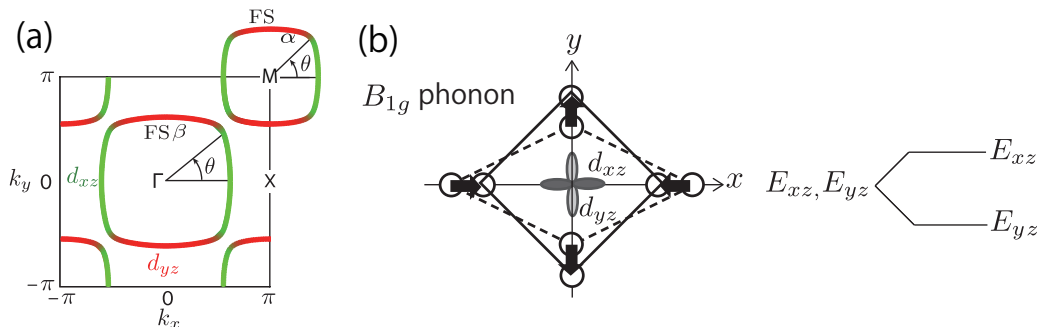


Figure 19: (a) Obtained Fermi surfaces for $n_d = 2.3$. It is quite similar to that in Sec.2 (b) The B_{1g} -type electron-phonon coupling caused by in-plane distortion.

Next, we derive the matrix elements of 4-point vertex due to the B_{1g} phonon included in the p-h excitation. Figure 20 shows the first-order correction for p-h excitation process at $\omega = 0$. In Figs.21(a) and (b), diagrammatic definition of the phonon-mediated interaction $\hat{C}_g^{\sigma\sigma\rho\rho}$ with spin-dependency, which is given by

$$C_{g,l'l'mm'}^s = \begin{cases} g & (l = l' = m = m') \\ -g & (l = m \neq l' = m') \\ 0 & (\text{otherwise}), \end{cases} \quad (3.4) \quad C_{g,l'l'mm'}^c = \begin{cases} +g & (l = l' = m = m') \\ -2g & (l = l' \neq m = m') \\ +g & (l = m \neq l' = m') \\ 0 & (\text{otherwise}), \end{cases} \quad (3.5)$$

where $\hat{C}_g^{c(s)} \equiv \hat{C}_g^{\uparrow\uparrow\uparrow\uparrow} + (-)\hat{C}_g^{\uparrow\uparrow\downarrow\downarrow}$. This spin dependence originates from the Pauli exclusion principle and Eq.(3.3). Here, we assume the relation $\omega_D \gg W_{\text{band}}$. Therefore, $g(\omega_j)$ is replaced with the constant value g . In this case, both bubble and ladder diagrams contribute to p-h fluctuations. If opposite situation ($\omega_D \ll W_{\text{band}}$) occurs, ladder-type scattering process should be small. Especially, p-h excitation due to ladder term is proportional to $-T \sum_k G_{lm}(k+q)G_{m'l'}(k)\theta(\omega_D - |\epsilon|)$. This contribution must be smaller than that without energy cutoff reduced by $\theta(\omega_D - |\epsilon|)$. Therefore, phonon-mediated 4-point vertex under

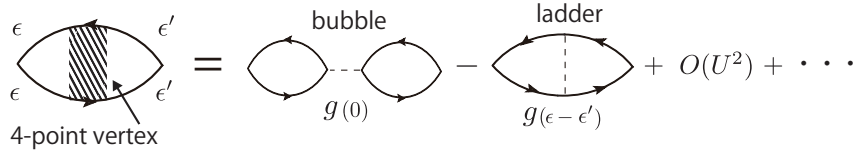
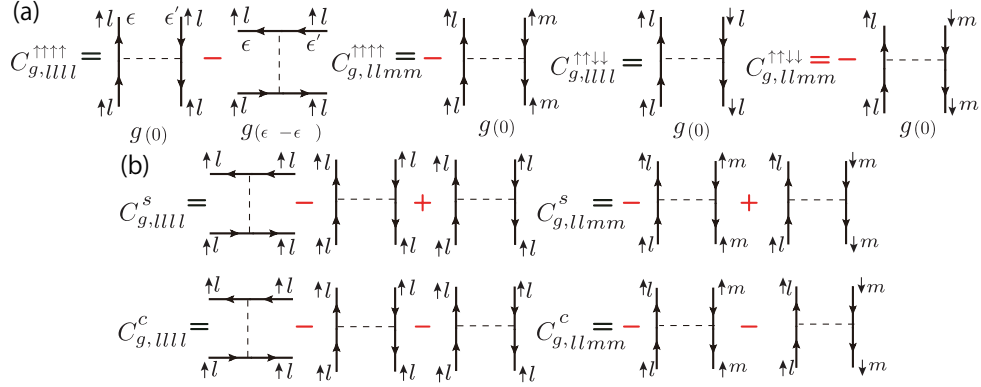


Figure 20: The diagrammatic expression for the first order correction included in p-h fluctuations.

Figure 21: (a), (b) The diagrammatic expression for the bare 4-point vertex function due to the B_{1g} -type el-ph coupling. Here, we put $l \neq m$.

the condition of $\omega_D \ll W_{\text{band}}$ is rewritten

$$C_{g,ll'mm'}^s = 0 \quad (\text{all element}), \quad (3.6) \quad C_{g,ll'mm'}^c = \begin{cases} +2g & (l = l' = m = m') \\ -2g & (l = l' \neq m = m') \\ 0 & (\text{otherwise}). \end{cases} \quad (3.7)$$

Then, \hat{C}_g^c in Eq.(3.7) is given by

$$C_{g,ll'mm'}^c = -2g(2\delta_{l,m} - 1)\delta_{l,l'}\delta_{m,m'} \quad (3.8)$$

Totally, 4-point vertex $C^{s(c)}$ for spin (charge) channel due to the el-ph end Coulomb interaction is given by

$$\hat{C}^s \equiv \hat{U}^s \quad \hat{C}^c \equiv \hat{U}^c - \hat{C}_g. \quad (3.9)$$

As a result, spin channel 4-point vertex is independent of the g for $\omega_D \ll W_{\text{band}}$.

● key facts

- * 1 We introduce 4-point vertex \hat{C}_g induced by B_{1g} phonon mediated interaction.
- * 2 Under the condition of $\omega_D \ll W_{\text{band}}$, \hat{C}_g works as a charge channel 4-point vertex.

Method & Result

3.2 B_{1g} -orbital fluctuations

In this section, we derive spin and charge susceptibilities considering χ -VC by performing self-consistent VC (SC-VC) method. In the following numerical analysis, the parameters are fixed at $J/U = 0.08$, $T = 5 \times 10^{-2}$, 32×32 \mathbf{k} -meshes and 256 Matsubara frequencies. Within SC-VC scheme, spin (charge) susceptibilities are given by

$$\hat{\chi}^{s(c)}(q) = \hat{\Phi}^{s(c)}(q)(\hat{1} - \hat{C}^s(c)\hat{\Phi}^{s(c)}(q))^{-1}, \quad (\hat{\Phi}^{s(c)}(q) = \hat{\chi}^0(q) + \hat{X}^{s(c)}(q)) \quad (3.10)$$

The irreducible susceptibility $\hat{\chi}^0$ is calculated by

$$\chi_{ll'mm'}^0(q) = -T \sum_k G_{lm}(k+q)G_{m'l'}(k), \quad (3.11)$$

where Green function $G_{lm}(k)$ is in the orbital basis without self energy effects Σ . $\hat{X}^{s(c)}(q)$ denotes χ -VC induced by the AL process introduced in Eq.(2.34) in the previous section (Sec.2), which contains the 3-point vertex function $\hat{\Lambda}^{s(c)}$. In the present SC-VC study, we obtain $\hat{X}^c(q)$ self-consistently, while $\hat{X}^s(q)$ is neglected since it is not so important as discussed in Sec.2. Here, spin (charge) Stoner factor $\alpha_{S(C)}$ is defined as the largest eigenvalue obtained from the following equation

$$\left\{ \hat{C}^{s(c)} \hat{\Phi}^{s(c)}(q) \right\} \vec{v} = \lambda \vec{v}. \quad (3.12)$$

Figures 22 (a) and (b) show obtained spin and charge susceptibility calculated by SC-VC method. Here, total spin susceptibility is defined as $\chi^s(\mathbf{q}) = \sum_{lm} \chi_{llmm}^s(\mathbf{q})$, while B_{1g} -orbital susceptibility is given by $\chi_{x^2-y^2}^c(\mathbf{q}) = \sum_{lm} (-1)^{l+m} \chi_{llmm}^c(\mathbf{q})$, which has operator of B_{1g} -type order parameter ($\hat{n}_{xz} - \hat{n}_{yz}$). In these results, we fix the parameters at $(U, g) = (2.1, 0.15)$ and $(\alpha_S, \alpha_C) = (0.92, 0.93)$. We find that B_{1g} orbital susceptibility has large value almost equivalent to spin susceptibility. Then, $\chi^s \approx \chi^c$ realize even in the presence of quite small g . For instance, $\alpha_C \lesssim 1$ is satisfied when $g \approx 0.15$ ($\lesssim 0.1U$) in the case of $\alpha_S \gtrsim 0.9$. This fact can be understood by following approximate equation

$$\chi_{x^2-y^2}^c(\mathbf{Q}) \sim \Phi^c(\mathbf{Q}) [1 - (2U' - U + 4g)\Phi^c(\mathbf{Q})]^{-1}, \quad (\alpha_C \lesssim 1) \quad (3.13)$$

where $\Phi^c(\mathbf{Q})$ corresponds to irreducible susceptibility with intra-orbital channel. Thanks to the existence of U' , charge channel Stoner factor; $\alpha_C = (2U' - U + 4g)\Phi^c(\mathbf{Q})$ reaches unity in the presence of small B_{1g} -phonon. Moreover, minimal value of g to realize $\alpha_C = 1$ decrease when $\Phi^c(\mathbf{Q}) \gg \chi^0(\mathbf{Q})$ holds due to the AL-type χ -VC. In this case, strong orbital fluctuations develop thanks to the cooperation between small B_{1g} -phonon and many body effects due to χ -VC. Especially, B_{1g} -phonon can cooperate with anti-ferro spin susceptibilities via χ -VC. In contrast, we need large $g \ll U$ to obtain χ^c without χ -VC based on RPA method. We comment that charge-channel of χ -VC at $q = 0$ is written as $T \sum_p \{3\chi^s(p)^2 + \chi^c(p)^2\}$ in SC-VC method. Thus, the contribution of $\chi^s(q)$ overwhelms that of $\chi^c(q)$ even at $\alpha_S \sim \alpha_C$. Therefore, we safely put $g = 0$ in χ -VC.

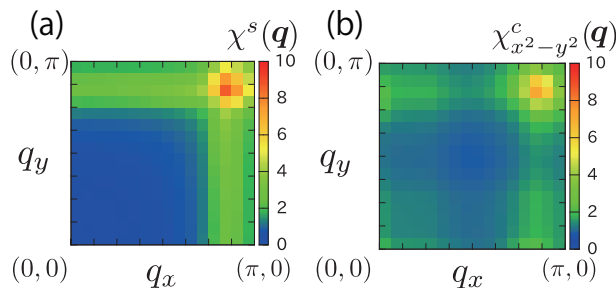


Figure 22: (a) Total spin susceptibility $\chi^s(\mathbf{q})$. (b) Orbital susceptibility $\chi_{x^2-y^2}^c(\mathbf{q})$ belonging to B_{1g} -symmetry at $(\alpha_S, \alpha_C) = (0.92, 0.93)$ and $(U, g) = (2.1, 0.15)$.

● key facts

- * 1 Strong orbital fluctuations χ^c are induced by the small B_{1g} phonon $g \lesssim U/10$.
- * 2 Microscopic origin of strong χ^c is cooperation between B_{1g} phonon and spin susceptibility. The mechanism comes from the significant roles of χ -VC.

3.3 Superconductivity

Now, we analyze SC state beyond Migdal-Eliashberg (ME) scheme. Linearized gap equation is given by

$$\lambda \Delta^a(\theta, \epsilon_n) = -\frac{\pi T}{(2\pi)^2} \sum_{a'\epsilon_m} \int_0^{2\pi} \frac{d\theta'}{v_{a'\theta'}} \left| \frac{\partial \mathbf{k}_{a'\theta'}}{\partial \theta'} \right| \frac{\Delta^{a'}(\theta', \epsilon_m)}{|\epsilon_m|} V^{aa'}(\theta\epsilon_n, \theta'\epsilon_m), \quad (3.14)$$

where $\Delta^a(\theta, \epsilon_n)$ is spin singlet SC gap function on the Fermi surface α, β , λ is eigenvalue of the gap equation, and $V^{aa'}(\theta\epsilon_n, \theta'\epsilon_m)$ is SC interaction in the band basis. $\mathbf{k}_{a\theta}$ is the Fermi momentum on Fermi surface a , and $v_{a\theta}$ is the Fermi velocity.

The SC paring interaction is calculated by $\hat{\chi}^{s(c)}(q)$ in SC-VC method,

$$\hat{V}(k, k') = \frac{3}{2} \hat{V}^s(k, k') - \frac{1}{2} \hat{V}^c(k, k') - \hat{C}^s, \quad (3.15)$$

which is transformed into $V^{aa'}(\theta\epsilon_n, \theta'\epsilon_m)$ by multiplying unitary matrix of $u_{la}(k)$. Here,

$$\hat{V}^{s(c)}(k, k') = \hat{\Lambda}^{s(c)}(k, k') \left\{ \hat{C}^{s(c)} \hat{\chi}^{s(c)}(k - k') \hat{C}^{s(c)} + \hat{C}^{s(c)} \right\} \hat{\Lambda}^{s(c)*}(-k, -k') \quad (3.16)$$

$\hat{\Lambda}^{s(c)}$ is the AL-type 3-point vertex function for SC paring interaction, which we call U -VC. The relation $\Lambda_{ll'mm'}^{s(c)*} \equiv \Lambda_{m'l'm'l}^{s(c)}$ holds. We set $g = 0$ for the calculation of $\hat{\Lambda}$, since U -VC from χ^s dominates over that from χ^c even in the case of $\alpha_S \sim \alpha_C$ in the same way of χ -VC.

Here, we show numerical result of U -VC. In Figs.23(a) and (b), charge- and spin-channel enhancement factors are plotted, which is defined as

$$\left| \Lambda_{aa'}^{s(c)}(\theta, \theta') \right|^2 \equiv \left| \sum_{l'l'm} \Lambda_{ll'mm}^{s(c)}(k, k') u_{la}^*(\theta) u_{l'a'}(\theta') \right|^2. \quad (3.17)$$

Here, we put $U = 2.1$ ($\alpha_S = 0.92$) and $\epsilon_n = \epsilon_{n'} = \pi T$. We find $|\Lambda^c|^2 \gg 1$ when $\theta \approx \theta'$ or $\theta \approx \theta' \pm \pi$, which meant that orbital character of θ and θ' is the same. In contrast, $|\Lambda^s|^2 \ll 1$ holds. α_S -dependent of them is plotted in Fig.23(c). The obtained relation $|\Lambda^c|^2 \gg 1$ is understood by charge-channel AL-type U -VC, which is given by $\Lambda^{\text{AL},c}(q) \propto \sum_p \chi^s(p) \chi^s(p+q)$. The diagrammatic explanation is shown in Fig.23 (d).

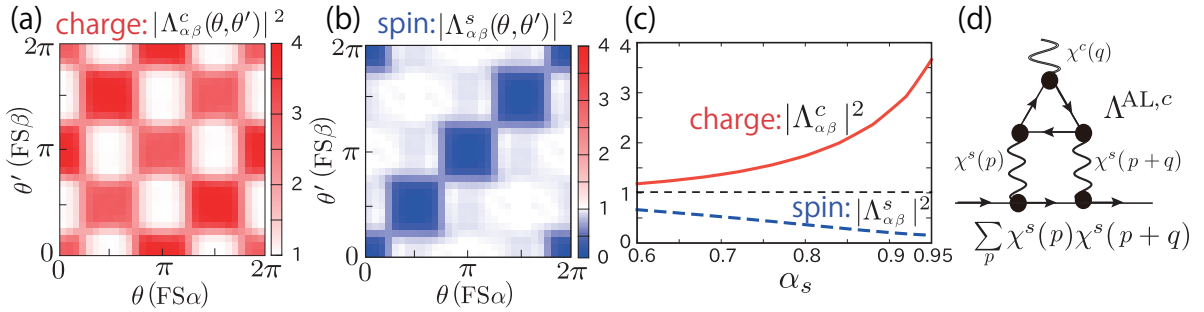


Figure 23: (a)(b) U -VC for charge channel and spin channel at the lowest frequency. Fermi point is represented by angular θ (θ') on the Fermi surface α (β). (c) Obtained U -VC as a function of α_S at $\theta = \theta' = 0$. (d) Feynman diagram of AL-term in charge channel.

Now, we discuss our numerical results by solving the gap equation (4.47). Note that el-ph interaction works as static attraction since we set $g(\omega_j) = g$ as we discussed in the previous section. Therefore, retardation effect is neglected, which cause underestimation of T_c for the s -wave SC paring. Moreover, we only consider lowest energy term as U -VC and χ -VC and crossing pairing interaction is excluded since it was not important shown in Sec.2. Our main conclusion does not change by these simplification.

In Fig.24(a), we show SC phase diagram from the linearized gap equation. 3 types of s -wave states are plotted in Figs. 24(b)-(d) Note that $d_{x^2-y^2}$ -wave phase appears with small α_s ($\alpha_s \leq 0.85$). As a result, fully gapped s_{++} state without any sign reversal is realized for a wide region around $\alpha_C \sim \alpha_S \geq 0.8$,

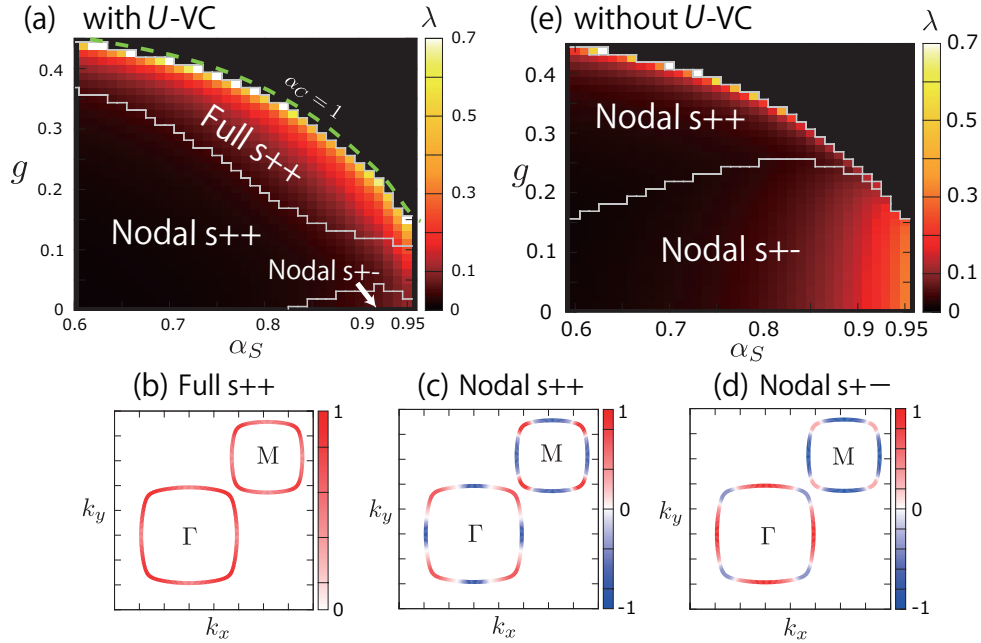


Figure 24: (a) Obtained SC phase diagram given by maximum eigenvalue of the gap equation in the presence of U -VC. Obtained gap structures on each Fermi surfaces for the (b) fully gapped s_{++} state, (c) nodal s_{++} state, and (d) nodal s_{+-} state. The antiferromagnetic (orbital) ordered phase occurs when $\alpha_{S(C)} \geq 1$. (e) Obtained phase diagram in the absence of U -VC. (f) α_S dependence of λ at $g = 0.2$.

which comes from enlarged (suppressed)-attraction (repulsion) due to $|\Lambda^{c(s)}|^2$. In contrast, as we show in Fig.24(e), the full-gap s_{++} state disappears in the absence of U -VC. For this reason, significant roles of U -VC for s -wave pairing mechanism is clearly confirmed, which means that Migdal Eliashberg (ME) theorem fails. The violation of ME theorem occurs due to the strong \mathbf{q} -dependence of SC pairing interaction irrespective of its small energy scale. The eigenvalue for fully gapped s_{++} state drastically increases as α_S get larger, while λ for s_{++} and s_{+-} states remains very small. Therefore, T_c for nodal s -wave states should be very low. As a result, s_{++} wave state is stabilized by charge-channel SC interaction;

$$V^c \simeq \frac{1}{2} \{U - 4g + (2U' - U + 4g)^2 \chi_{x^2-y^2}^c(\mathbf{Q})\} |\Lambda^c|^2. \quad (3.18)$$

Here, large negative (attractive) pairing interaction comes from $|\Lambda^c|^2 \gg 1$ around $\alpha_C \lesssim 1$ owing to AL-type χ -VC.

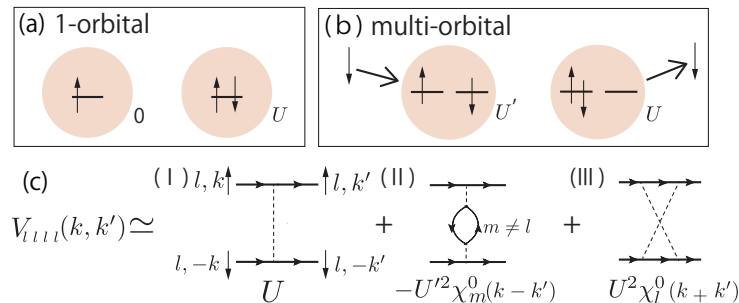


Figure 25: Depairing processes to intra-orbital Cooper pairs caused by on-site Coulomb interaction in the case of (a) 1-orbital or (b) 2-orbital systems. In multi-orbital system, energy loss in forming intra-orbital Cooper pairs is drastically reduced from U to $\sim (U - U')$ thanks to the “multi-orbital screening effect”. (c) SC pairing interaction up to the 2nd order terms of U . The process (II) appear only in the multi-orbital systems.

Finally, we comment on “multi-orbital screening effect” in the multi-orbital SCES. We find that effect of on-site Coulomb repulsion for isotropic Cooper pair is strongly reduced by multi orbital nature of the system. In Figs.25(a) and (b), schematic depairing processes for intra-orbital Cooper pairs are plotted in the case of 1- and 2-orbital system, respectively. To simplify the discussion, Hund’s coupling J is omitted. The energy loss to form intra-orbital Cooper pairs is U in 1-orbital system. On the other hand, it is reduced to $\sim (U - U')$ if we consider multi-orbital system. This reduction comes from screening among d -electrons with different orbitals as shown in Fig.25(b). Therefore, multi-orbital screening effects play important roles for forming s -wave or on-site SC Cooper pairs. Figure 25(c) shows the 2nd order term of U in SC interaction for intra-orbital Cooper pair. Approximately, we obtain

$$V_{lll}^{\uparrow\downarrow\uparrow\downarrow}(k, k') \propto \sum_m U - U'^2 \chi_{mmmm}^0(k - k') + U^2 \chi_{llll}^0(k + k') \quad (l \neq m), \quad (3.19)$$

where we assume $G_{lm} = G_l \delta_{l,m}$ for simplicity. Scattering process (II) exists only in the multi-orbital systems. Due to (II), direct Coulomb depairing term (I) is reduced. The screening effect becomes prominent when $U' \chi_m^0 \sim O(1)$ for $l \neq m$. In addition, depairing effect is further reduced by retardation effect due to the ω -dependence of el-ph interaction.

● key facts

- * 1 Fully gapped s_{++} -wave SC phase appears near magnetic QCP due to U -VC and χ -VC.
- * 2 Origin of s_{++} -wave state is cooperation between B_{1g} phonon and antiferro spin fluctuation.

Discussion

3.4 Local approximation for U -VC

Now, we explain that the k -dependence of U -VC is important to obtain s_{++} -wave SC state. To begin with, figure 26 (a) represents SC phase diagram in α_S - α_C space. In this case, we consider momentum dependence correctively. Thus, it is almost equivalent to that in α_S - g space in Fig.24(a). On the other hand, we obtain U -VC by using the local approximation, which is given by the averaged over in \mathbf{k} -space on Fermi surfaces,

$$\hat{\Lambda}_{\text{loc}}^{s(c)}(\epsilon_n, \epsilon_{n'}) = \langle \hat{\Lambda}^{s(c)}(k, k') \rangle_{\mathbf{k}, \mathbf{k}'}. \quad (3.20)$$

Figure 26(b) is obtained by considering $\hat{\Lambda}_{\text{loc}}^x(\epsilon_n, \epsilon_{n'})$. Fully gapped s_{++} -wave region disappears in this case. In particular, obtained phase diagram is quite similar to that when U -VC is neglected as shown in Fig.24(e). Therefore, we conclude that the momentum dependence of U -VC is significant in terms of s -wave SC pairing mechanism.

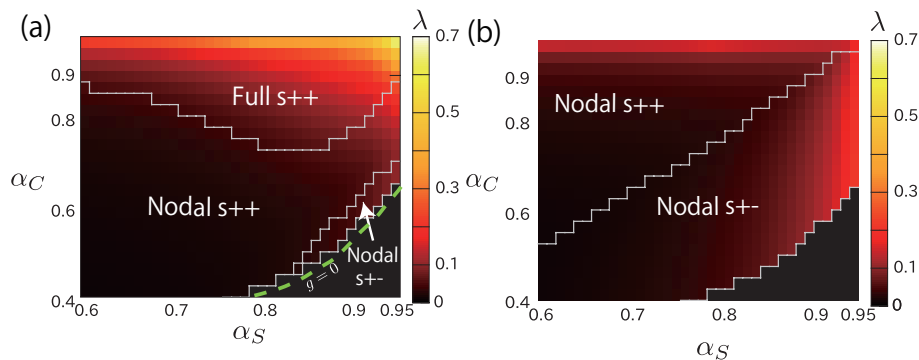


Figure 26: (a) SC phase diagram plotted in α_S - α_C space. This is almost equal to that in α_S - g space as shown in Fig.24(a). (b) Phase diagram calculated by considering local approximation type of U -VC.

● key facts

- * 1 s_{++} -wave SC state does not appear if we treat U -VC by using local approximation.
- * 2 \mathbf{k} -dependence of U -VC is important to understand the SC pairing mechanism.

3.5 Filling dependence

In the previous section, we analyze the SC phase diagram at fixed filling n_d . In this section, we discuss filling dependence of SC phase diagram. Figure 27 shows obtained SC phase diagram including both spin singlet and triplet SC region as a function of chemical potential μ as well as el-ph interaction g . Here, $n_d = 2.3$ is equivalent to $\mu = 0.5$. On the each point, U is set for satisfying the condition of $\alpha_S = 0.94$. Charge Stoner factor α_C increase by $g (< 0.98)$.

In Fig.27(a), SC phase diagram is plotted where U -VC is correctly considered. Present 2-orbital model brings rich SC states. Fully gapped s_{++} -wave phase appears for a wide range of filling parameter. It is noteworthy that TSC phase emerges around $\mu \simeq 1$, which is equivalent to the previous work by fRG+cRPA study (in Sec.2). On the other hand, s_{++} -wave SC phase disappears if U -VC is dropped given in Fig.27(b). Therefore, U -VC plays important roles for realizing the fully gaped s_{++} wave pairs for wide parameter region.

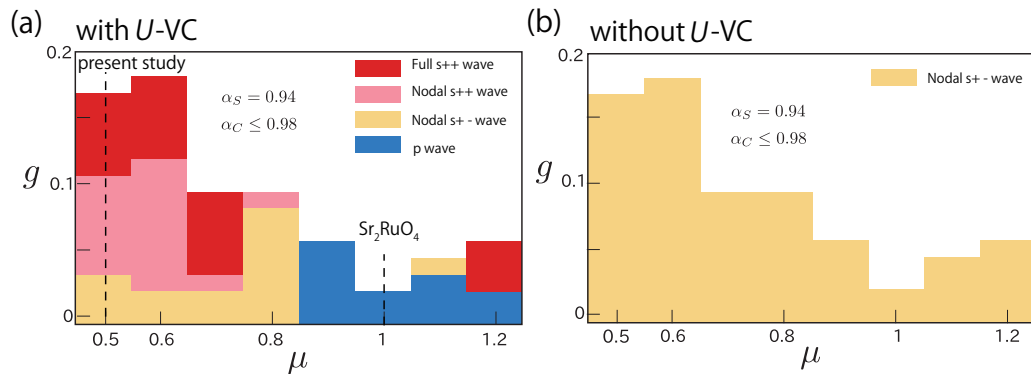


Figure 27: Phase diagram of spin singlet and triplet SC phase (a) considering or (b) neglecting U -VC in μ - g space. At each point, U is set to satisfy $\alpha_S = 0.94$. Filling parameter used in Sec.2 ($n_d = 2.67$) corresponds to $\mu = 1$, here. White colored region represents $\alpha_C > 0.98$.

● key facts

- * 1 U -VC brings rich variety of SC state, including TSC phase.
- * 2 Fully gapped s -wave SC state appears in wide parameter region.

3.6 Retardation & impurity effects

In the previous section, we neglect the retardation effect, which means that the relation $g(\omega) = \text{constant}$ is assumed. However, the present simplification brings underestimation of the fully gaped s_{++} wave phase. In this section, we consider retardation effect given by $\omega_D \ll T$, that is, $g(\omega_j) = g\delta_{j,0}$. In this case, retardation effects get prominent. In fact, obtained SC phase is given in Fig.28. s -wave SC region is drastically expanded due to the retardation effect compared with Fig.26(a). Therefore, the retardation effects is important to obtain s -wave SC state.

Next, we analyze the SC phase in the presence of dilute non magnetic impurities based on T -matrix approximation, since it is generally known that impurities sensitively affect to SC state. Linearized gap

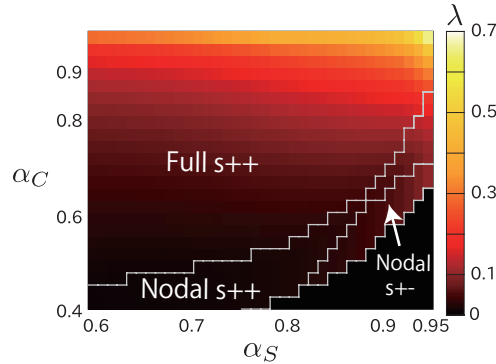


Figure 28: SC phase diagram by considering strong retardation effect. s_{++} -wave region is drastically expanded thanks to retardation effect.

equation in the band basis in the presence of impurities is given by

$$\lambda \Delta^a(\mathbf{k}, \epsilon_n) = \frac{-T}{(2\pi)^2} \sum_{a' \epsilon_m \mathbf{k}'} |G_{a'}(\mathbf{k}', \epsilon_m)|^2 \Delta^{a'}(\mathbf{k}', \epsilon_m) \left[V^{aa'}(\mathbf{k}, \epsilon_n, \mathbf{k}', \epsilon_m) - \frac{n_{\text{imp}}}{T} |T_{aa'}(\mathbf{k}, \mathbf{k}', \epsilon_m)|^2 \delta_{n,m} \right] \quad (3.21)$$

which is diagrammatically shown in Fig.29(a). n_{imp} denotes concentration of the impurity. $T_{aa'}(\mathbf{k}, \mathbf{k}', \epsilon_m)$ is T -matrix due to the impurity as shown in Fig.29(b). Double line corresponds to the Green function $G_a(\mathbf{k}, \epsilon_n)$ including the impurity-induced self-energy $\Sigma_a(k) = n_{\text{imp}} T_{aa}(\mathbf{k}, \mathbf{k}, \epsilon_n)$, shown in Fig. 29(c).

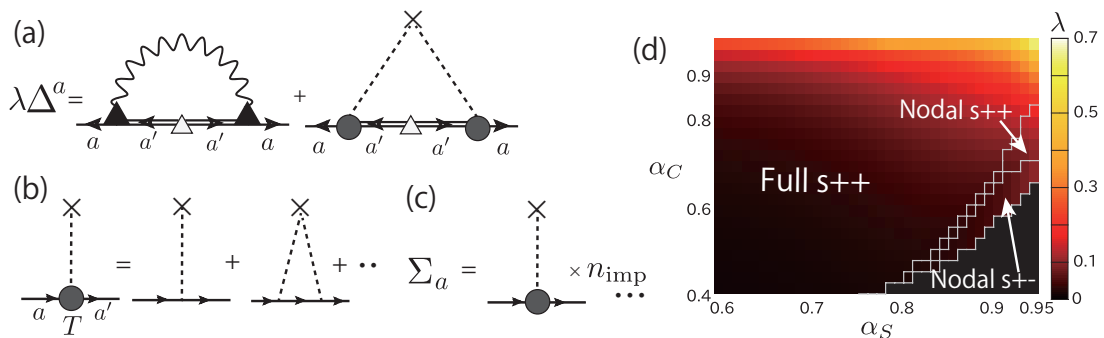


Figure 29: (a) Linearized gap equation with impurities. (b) Diagrammatic expression of T -matrix due to the single impurity. (c) Self-energy included in the Green function mediated by impurity. (d) SC phase diagram at $n_{\text{imp}} = 0.1\%$ in α_S - α_C space. s_{++} -wave region is expanded by doping the impurities.

Figure 29(d) shows the superconducting phase diagram in the α_S - α_C space. We find that the area of the full-gap s_{++} wave state is drastically expanded by the impurity effect even for $n_{\text{imp}} = 0.1\%$.

● key facts

- * 1 Retardation effect due to the B_{1g} phonon stabilizes fully gapped s -wave SC state.
- * 2 Impurity effect enhances the region of s -wave SC phase even at $n_{\text{imp}} = 0.1\%$.

Conclusion

In summary, we proposed possible microscopic origin of the fully gapped s -wave phase in SCES when weak e -ph interaction in B_{1g} -symmetry exist. We demonstrate that orbital fluctuations drastically develop thanks to the cooperation between χ -VC and B_{1g} -type el-ph interaction. Then, orbital-fluctuation-mediated attractive force is enlarged by charge channel type U -VC. On the other hand, repulsion for

Cooper pairs due to spin fluctuations are reduced by spin channel U -VC. Moreover, energy loss caused by on-site Coulomb repulsion between intra-orbital Cooper pairs is reduced by "multi orbital screening effect". In the obtained phase diagram, plain s -wave state with large eigenvalue emerges near the magnetic criticality.

We also explained that momentum dependence of U -VC is important to obtain s -wave SC phase. Note that charge-channel U -VC is also enhanced by AL-type VC even in the case of 1-orbital system as shown in Appendix B. Therefore, Kohn anomaly observed in High- T_c cuprate superconductor can be explained by using our proposed theory. For instance, quantum Monte Carlo (QMC) study was performed based on the 1-orbital Hubbard model on 2D square lattice [11]. We comment that s -wave SC phase is also discussed by using DMFT and VCA method [12]-[13].

The main findings of the present study are listed as follows;

- (i) Based on the 2D HH model, it was uncovered that fully gapped s -wave SC state appears near AFM-QCP against strong Coulomb repulsion.
- (ii) Microscopic origin of s -wave SC state comes from cooperation between spin fluctuations and B_{1g} el-ph interaction due to the important roles of χ -VC.
- (iii) Energy loss due to the on-site Coulomb repulsion is suppressed by multi-orbital screening effect in the case of multiorbital system.
- (iv) Momentum-dependence of U -VC is prominent in forming isotropic Cooper pairs.
- (v) U -VC brings rich variety of SC phase diagram including both spin singlet and triplet SC state.
- (vi) Retardation and impurity effects drastically stabilize s -wave SC phase.

In the following section (Sec.4), we apply our present theory with χ -VC and U -VC for multi-orbital heavy fermion system.

References

- [1] C. H. P. Wen, H. C. Xu, C. Chen, Z. C. Huang, Y. J. Pu, Q. Song, B. P. Xie, Mahmoud Abdel-Hafiez, D. A. Chareev, A. N. Vasiliev, R. Peng, and D. L. Feng, *Nat. Commun.* **7**, 10840 (2016).
- [2] Y. J. Yan, W. H. Zhang, M. Q. Ren, X. Liu, X. F. Lu, N. Z. Wang, X. H. Niu, Q. Fan, J. Miao, R. Tao, B. P. Xie, X. H. Chen, T. Zhang, and D. L. Feng, *Phys. Rev. B* **94**, 134502 (2016).
- [3] Y. Takabayashi and L. Prassides, *Phil. Trans. R. Soc. A* **374**, 20150320 (2016).
- [4] S. Rebec, T. Jia, C. Zhang, M. Hashimoto, D. Lu, R. Moore, and Z. Shen, arXiv:1606.09358.
- [5] Y. Zhou and A. J. Millis, *Phys. Rev. B* **93**, 224506 (2016).
- [6] S. Choi, W.-J. Jang, H.-J. Lee, J. M. Ok, H. W. Choi, A. T. Lee, A. Akbari, H. Suh, Y. K. Semertzidis, Y. Bang, J. S. Kim, and J. Lee, arXiv:1608.00886.
- [7] L. Rademaker, Y. Wang, T. Berlijn, and S. Johnston, *New J. Phys.* **18**, 022001 (2016).
- [8] M. Capone, M. Fabrizio, and E. Tosatti, *Phys. Rev. Lett.* **86**, 5361 (2001).
- [9] Y. Nomura¹, S. Sakai, M. Capone, and R. Arita, *Science Advances* **1**, e1500568 (2015).
- [10] M. Kim, Y. Nomura, M. Ferrero, P. Seth, O. Parcollet, and A. Georges, *Phys. Rev. B* **94**, 155152 (2016).
- [11] Z. B. Huang, W. Hanke, E. Arrigoni, and D. J. Scalapino, *Phys. Rev. B* **68**, 220507(R) (2003).
- [12] O. Bodensiek, R. Zitko, M. Vojta, M. Jarrell, and T. Pruschke, *Phys. Rev. Lett.* **110**, 146406 (2013).
- [13] K. Masuda and D. Yamamoto, *Phys. Rev. B* **91**, 104508 (2015).

4 S-wave superconductivity in CeCu₂Si₂

Introduction

In heavy fermion systems, exotic electronic phenomena are induced by strong Coulomb repulsion and spin-orbit coupling (SOI) in f -electron system. Especially in Ce-based metals, $4f^1$ configuration appears on Ce³⁺ ion. In the presence of strong SOI, total angular momentum $J(=L+S)$ comes to be good quantum number. Energy level of $J=5/2$ state is $\sim 0.3\text{eV}$, which is lower than that of $J=7/2$ state. Therefore, $J=7/2$ state can be neglected at low temperature regime within theoretical study. In the presence of tetragonal CEF, 6-folded states with $J=5/2$ are divided into 3 Kramers doublets. In general, energy scale of CEF splitting is of order $1\sim 10\text{meV}$.

Moreover, higher-ranks of multipole degrees of freedom become active due to the strong SOI in f -electrons. As a result, various multipole phase and quantum fluctuations appear by strong Coulomb interaction [2]-[8]. For instance, orbital degrees of freedom in CeB₆ cause quadrupole (rank 2) and octupole (rank 3) phase transition induced by magnetic field [8, 18]. In addition, hexadecapole (rank 4) and dotriacontapole (rank 5) ordering have been studied in PrRu₄P₁₂ [10] and URu₂Si₂ [11, 12, 13].

In terms of SC pairing mechanism, multipole fluctuations cause unconventional SC states. For example, d -wave SC state appears near the the magnetic criticality in CeMIn₅ ($M=\text{Rh,Co,Ir}$) [14]. On the other hand, SC phase emerges next to the quadrupole order in PrT₂Zn₂₀ ($T=\text{Rh and Ir}$) [15] and PrT₂Al₂₀ ($T=\text{V,Ti}$) [16]. These facts indicate that exotic SC states originates from higher-rank (≥ 2) multipole fluctuations in f -electron systems.

In this section, we focus on CeCu₂Si₂ well known as the first discovered heavy-fermion superconductor [17, 18, 19]. At $P=0$, SC transition appears at $T_c \approx 0.6\text{K}$ near the magnetic QCP [20]. Under the finite pressure ($P \neq 0$), T_c reaches 1.5K around $P_c \approx 4.5\text{GPa}$. Historically, it was believed that CeCu₂Si₂ is a typical d -wave superconductor induced by magnetic fluctuations. However, s -wave SC state was reported by some experiments in CeCu₂Si₂ [21, 22]. After that, fully gapped SC state was confirmed by specific heat, thermal conductivity and penetration depth measurements [23, 24]. Also, T_c was robust against randomness. Therefore, s -wave SC state without sign-reversal is realized in CeCu₂Si₂ [23].

One of the significant challenge for theorists is to reveal the microscopic origin of s -wave phase in heavy fermion (HF) systems, even if large Coulomb repulsion exists. In general, even-rank multipole fluctuations, such as charge (rank 0), quadrupole (rank 2) and hexadecapole (rank 4) operators, induce attractive SC pairing interaction. However, it is quite difficult to explain emergence of even-rank fluctuations as shown in Sec.2 and 3 in terms of orbital fluctuations. To obtain even-rank multipole fluctuations, more than 2 Kramers doublets are required to be degenerate since charge (rank 0) is drastically suppressed by Coulomb repulsion. In fact, 2 Kramers doublets exhibit Kondo resonance below 10K by performing LDA+DMFT study in CeCu₂Si₂ at $P=0$ [25]. We comment that P can change multiorbital nature and it may become one of the key facts in studying interesting P - T phase diagram observed in CeCu₂Si₂ [25, 26, 27].

Based on RPA study, even-rank multipole fluctuations are quite suppressed compared with odd-rank ones. Thus, gap structure is expected to have sign reversal within the ME scheme as discussed in the previous study in Ref.[28]. Through our present study, we reveal that this discrepancy comes from important roles of higher order many body effects due to VC, which is neglected in ME scheme. The violation of ME theorem [34] is induced by MT and AL-VC corresponding to the 1st and 2nd-order corrections with fluctuations [33, 5, 28, 35]. In general, it was naturally expected that moderate even-rank fluctuations bring strong attractive SC pairing interaction owing to AL-type U -VC [35, 36]. However, it is difficult to study the roles of U - or χ -VC by considering all of the multipole degrees of freedom in the presence of strong SOI. Therefore, it has been required to construct a theoretical method to analyze the roles of VC in HF system. We comment that DMFT [11, 25],[37]-[41] has been studied while momentum dependence of VC near AFM-QCP is not fully considered.

In this section (Sec.4), we propose a microscopic pairing mechanism of s -wave SC phase in multipole HF systems CeCu₂Si₂ considering χ -VC and U -VC. First, we reveal that various types of multipole fluctuations develop simultaneously near the AFM-QCP. It comes from the cooperation of strong SOI and on-site Coulomb repulsion. Secondly, we show that the enhanced multipole fluctuations give prominent VC in HF systems. In particular, VC enhance attractive pairing interaction due to even-rank multipole fluctuations. As a result, s -wave SC appears even in the HF system, when moderate (phonon-induced) quadrupole or hexadecapole fluctuations exist. Therefore, present results can be responsible for the

s-wave SC state observed in CeCu₂Si₂.

Compared with 3*d*-electron systems, the violation of SU(2) symmetry in the spin-space affect the low temperature physics in 5*d* or *f*-electron systems, significantly. Thus, the same footing cannot be applied to the present model in HF system. To overcome this difficulty, we introduce a natural 2-orbital periodic Anderson model (PAM), in which the pseudo-spin has axial rotational symmetry. This fact enable us to calculate VC accurately even in the presence of multipole degrees of freedom. Therefore, we study χ -VC and *U*-VC in the present model with 16 type multiple operators (rank 0~5).

Model

4.1 $\Gamma_7^{(1)}$ - $\Gamma_7^{(2)}$ Periodic Anderson Model

We consider $4f^1$ ($L = 3, S = 1/2$) electrons on Ce-ion in CeCu₂Si₂. In the presence of strong SOI, 4*f* orbitals (14 degeneracy) are split into $J = 3/2$ (8 degeneracy) and $J = 5/2$ (6 degeneracy) where J is total angular momentum. When we consider $4f^1$ (less than half) state, $J = 5/2$ becomes ground states. Furthermore, $J = 5/2$ states split into 3 Kramers doublets as shown in Fig.30(a). According to the LDA+DMFT study for CeCu₂Si₂[25], the following two Kramers doublets give dominant DoS around the Fermi energy at ambient pressure. They are expressed in the J_z basis as,

$$\begin{aligned} |f_1 \downarrow\rangle &= a|+\frac{5}{2}\rangle + b|-\frac{3}{2}\rangle, \\ |f_1 \uparrow\rangle &= a|-\frac{5}{2}\rangle + b|+\frac{3}{2}\rangle, \\ |f_2 \uparrow\rangle &= -a|+\frac{3}{2}\rangle + b|-\frac{5}{2}\rangle, \\ |f_2 \downarrow\rangle &= -a|-\frac{3}{2}\rangle + b|+\frac{5}{2}\rangle, \end{aligned} \quad (4.1)$$

where \downarrow (\uparrow) represents pseudo spin up (down). a and $b = \sqrt{1-a^2}$ are coefficient parameter determined by CEF. We drop the third Kramers doublet $|f_3\rangle = |J_z = \pm\frac{1}{2}\rangle$, since it gives negligibly small weight near the Fermi level.

We use Periodic Anderson Model (PAM) for describing $4f^1$ electrons in CeCu₂Si₂. The kinetic term is given by

$$\hat{H}_0 = \sum_{\mathbf{k}\Sigma} \epsilon_{\mathbf{k}} c_{\mathbf{k}\Sigma}^\dagger c_{\mathbf{k}\Sigma} + \sum_{\mathbf{k}l\sigma} E_{l\mathbf{k}} f_{\mathbf{k}l\sigma}^\dagger f_{\mathbf{k}l\sigma} + \sum_{\mathbf{k}l\Sigma\sigma} \left(V_{\mathbf{k}l\Sigma\sigma}^* f_{\mathbf{k}l\sigma}^\dagger c_{\mathbf{k}\Sigma} + V_{\mathbf{k}l\Sigma\sigma} c_{\mathbf{k}\Sigma}^\dagger f_{\mathbf{k}l\sigma} \right) \quad (4.2)$$

where $c_{\mathbf{k}\Sigma}^\dagger$ ($c_{\mathbf{k}\Sigma}$) is a creation (annihilation) operator for conductive electron with momentum \mathbf{k} , spin Σ and energy $\epsilon_{\mathbf{k}}$. $f_{\mathbf{k}l\sigma}^\dagger$ ($f_{\mathbf{k}l\sigma}$) is a creation (annihilation) operator for *f*-electron with \mathbf{k} , orbital $l = 1, 2$, pseudo-spin σ , and energy $E_{l\mathbf{k}}$. We set $\epsilon_{\mathbf{k}} = 2t_{ss}(\cos k_x + \cos k_y) + \epsilon_0$, $t_{ss} = -1.0$, $V_{\mathbf{k}l\Sigma\sigma}$ is the hybridization term between *f*-electron and *s*-electron. In this study, we consider 2D square lattice model as shown in Fig.30(b). Both *f*- and *s*-orbital are on Ce-ion. $V_{\mathbf{k}l\Sigma\sigma}$ is calculated by using Slater-Koster table [46];

$$\begin{aligned} V_{\mathbf{k}f_1\uparrow\uparrow} &= -\sqrt{\frac{3}{14}}t_{sf}(a\sqrt{5}+b)(\sin k_y - i \sin k_x), \\ V_{\mathbf{k}f_1\downarrow\downarrow} &= \sqrt{\frac{3}{14}}t_{sf}(a\sqrt{5}+b)(\sin k_y + i \sin k_x), \\ V_{\mathbf{k}f_2\uparrow\uparrow} &= \sqrt{\frac{3}{14}}t_{sf}(a - \sqrt{5}b)(\sin k_y - i \sin k_x), \\ V_{\mathbf{k}f_2\downarrow\downarrow} &= -\sqrt{\frac{3}{14}}t_{sf}(a - \sqrt{5}b)(\sin k_y + i \sin k_x). \end{aligned} \quad (4.3)$$

Hereafter, to simplify the analysis, we put $a = 1, b = 0$. Then, we obtain simple expression;

$$V_{\mathbf{k}l\Sigma\sigma} = \sigma(-1)^l t_{sf}^l (\sin k_y - i\sigma \sin k_x) \delta_{\sigma,\Sigma}, \quad (4.4)$$

where $\delta_{\sigma,\Sigma}$ is Kronecker delta function. Note that pseudo spin is conserved ($V_{\uparrow\downarrow} \neq 0$) since the present system is 2D and has space inversion symmetry. The detailed derivation of Eq.(4.4) is explained in Appendix C. The imaginary terms come from strong SOI considered in the ground states in Eq.(4.1). We put $\mu = -5.52 \times 10^{-3}$, temperature $T = 0.02$ and the hopping parameter $t_{sf} = 0.7$. Then, f -electron number is $n_f = 0.9$ and s -electron number is $n_s = 0.3$. In this case, $(t_{sf}^{f_1}, t_{sf}^{f_2}) = (0.724, 0.324)$, which means that the 2-orbitals have different itinerancy.

We show the obtained band structure, Fermi surface and density of states (DoS) in Fig.31(a), (b) and (c), respectively. The chemical potential corresponds to $\epsilon = 0$. In addition, we set $E_{1\mathbf{k}} = 0.2$ and $E_{2\mathbf{k}} = 0.1$ by considering CEF splitting. (Detailed discussion is written in Sec.) $|t_{ss}|$ is of order 1eV since $W_D \sim 10\text{eV}$ in CeCu₂Si₂ [28]. The width of quasi-particle band (=the lowest band) is $W_D^{qp} \sim 1$. Large Fermi surface is obtained and the relation $D^{f_1}(0) \simeq D^{f_2}(0)$ is satisfied.

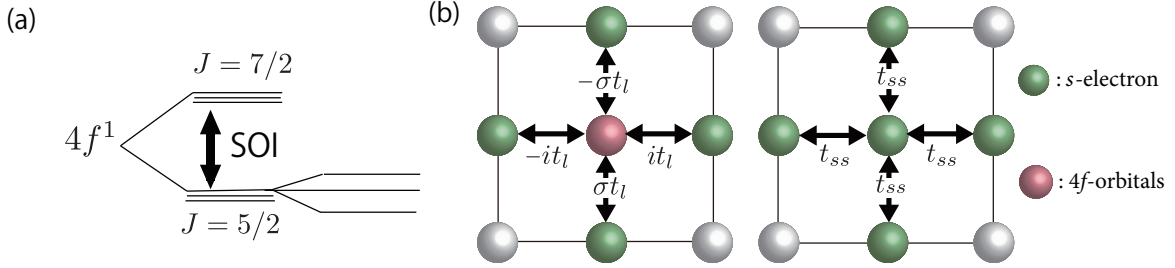


Figure 30: (a) The nearest neighbor hopping integrals given by s - s and s - f hoppings. We use $\sigma = 1(-1)$ for pseudo-spin up (down) and $t_l \equiv (-1)^{l-1}t_{sf}$.

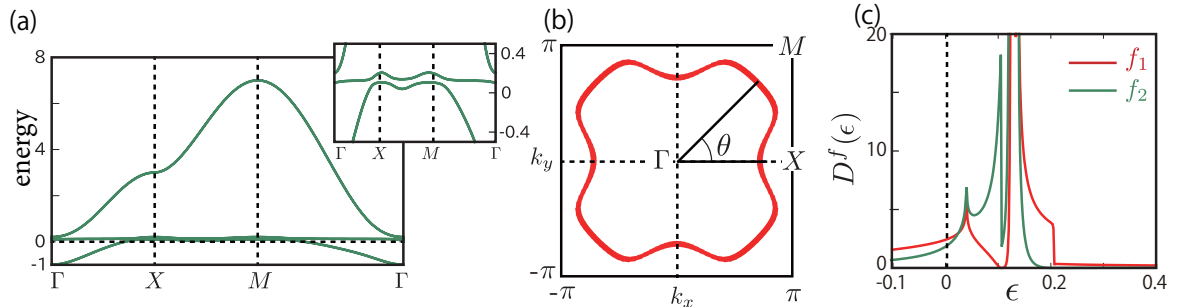


Figure 31: (a) Band dispersion along high-symmetry line. (b) Obtained Fermi surface at $n_f = 0.9$. (c) Partial DoS of f_l -electrons. The red (green) line corresponds to f_1 (f_2)-orbital.

In addition, we introduce on-site Coulomb interaction among f -electrons:

$$\hat{H}_U = r \cdot \frac{1}{4} \sum_i \sum_{ll'mm'} \sum_{\sigma\sigma'\rho\rho'} U_{ll'mm'}^{\sigma\sigma';\rho\rho'} f_{il\sigma}^\dagger f_{il'\sigma'} f_{im\rho} f_{im'\rho'}^\dagger \quad (4.5)$$

where i is site index. \hat{U} is the interaction matrix normalized as $U_{11;11}^{\uparrow\downarrow;\uparrow\downarrow} = 1$. Note that \hat{U} in Eq.(4.5) is antisymmetrized; $U_{ll'mm'}^{\sigma\sigma';\rho\rho'} = (-1)U_{mm';ll'}^{\rho\rho';\sigma\sigma'}$. We obtain the value of \hat{U} by performing the unitary transformation from l_z -basis Coulomb interaction: \bar{U} , which is given by

$$\begin{aligned} \bar{U}_{l_z l_z'; l_z'' l_z'''} &= \frac{e^2}{4\pi\epsilon_0} \int d\vec{r} \int d\vec{r}' \frac{u_{l_z}^*(\vec{r}) u_{l_z'''}^*(\vec{r}') u_{l_z}(\vec{r}') u_{l_z''}(\vec{r})}{|\vec{r} - \vec{r}'|} \\ &= \sum_p a_{l_z l_z' l_z'' l_z'''}^p F^p, \end{aligned} \quad (4.6)$$

where $u_{l_z}(\vec{r}) (=R(r)\Theta_{l_z}(\theta)e^{il_z\phi})$ is the wave function of f -electron which has eigenvalue of orbital angular momentum l_z . F^p is Slater integral introduced in Ref.[46], which is defined as

$$F^p = \frac{e^2}{4\pi\epsilon_0} \int dr \int dr' R^2(r) R^2(r') r_{\min}^p r_{\max}^{-(p+1)} r^2 r'^2, \quad (4.7)$$

where $r_{\min} = \min\{r, r'\}$ and $r_{\max} = \max\{r, r'\}$. We put $(F^0, F^2, F^4, F^6) = (5.3, 9.09, 6.927, 4.756)$ in unit eV by referring Ref.[47]. The derivation of a^p is written in Appendix D. Pseudo spin is conserved in Eq.(4.5) while SU(2) is broken with SOI. In this case, \hat{U} is uniquely decomposed into in-plane (s), out-of plane (s \perp) spin and charge (c) channel, which is defined as

$$\hat{U}^{\sigma\sigma';\lambda\lambda'} = \frac{1}{2}\hat{U}^s(\sigma_{\sigma\sigma'}^x\sigma_{\lambda'\lambda}^x + \sigma_{\sigma\sigma'}^y\sigma_{\lambda'\lambda}^y) + \frac{1}{2}\hat{U}^{s\perp}\sigma_{\sigma\sigma'}^z\sigma_{\lambda'\lambda}^z + \frac{1}{2}\hat{U}^c\sigma_{\sigma\sigma'}^0\sigma_{\lambda'\lambda}^0, \quad (4.8)$$

where $\vec{\sigma} = (\sigma^x, \sigma^y, \sigma^z)$ is Pauli matrix vector in the pseudo-spin space, and σ^0 is identity matrix. $\hat{U}^{s,s\perp,c}$ is defined as

$$\begin{cases} \hat{U}^s = \hat{U}^{\uparrow\uparrow;\uparrow\uparrow} - \hat{U}^{\uparrow\uparrow;\downarrow\downarrow} \\ \hat{U}^{s\perp} = \hat{U}^{\uparrow\downarrow;\uparrow\downarrow} \\ \hat{U}^c = \hat{U}^{\uparrow\uparrow;\uparrow\uparrow} + \hat{U}^{\uparrow\uparrow;\downarrow\downarrow}. \end{cases} \quad (4.9)$$

The matrix elements of $\hat{U}^{s,s\perp,c}$ are summarized in TABLE 1. They are related to general Hubbard model and composed of $\{U^{1(2)}U'JJ^\perp J'J^{x1(2)}\}$ in Eq.(32).

s	type	value	s \perp	type	value	c	type	value
$U_{11;11}^{0;s}$	U^1	1.0	$U_{11;11}^{0;s\perp}$	U^1	1.0	$U_{11;11}^{0;c}$	$-U^1$	-1.0
$U_{22;22}^{0;s}$	U^2	0.90	$U_{22;22}^{0;s\perp}$	U^2	0.90	$U_{22;22}^{0;c}$	$-U^2$	-0.90
$U_{lm;lm}^{0;s}$	$U' - J + J^\perp$	0.80	$U_{lm;lm}^{0;s\perp}$	$U' - J^{x1}$	0.68	$U_{lm;lm}^{0;c}$	$U' - J - J^\perp$	0.80
$U_{ll;mm}^{0;s}$	$J - J^{x1}$	-0.12	$U_{ll;mm}^{0;s\perp}$	J^\perp	0.0	$U_{ll;mm}^{0;c}$	$J - 2U' + J^{x1}$	-1.5
$U_{lm;ml}^{0;s}$	$J' - J^{x2}$	0.20	$U_{lm;ml}^{0;s\perp}$	$J' - J^{x2}$	0.20	$U_{lm;ml}^{0;c}$	$-J' + J^{x2}$	-0.20

Table 1: Matrix elements of Coulomb interaction for s (left), s \perp (middle), and c-channel (right) for $l \neq m$. $J = J'$, $J^\perp = 0$ and $J^{x1} = -J^{x2}$ are satisfied.

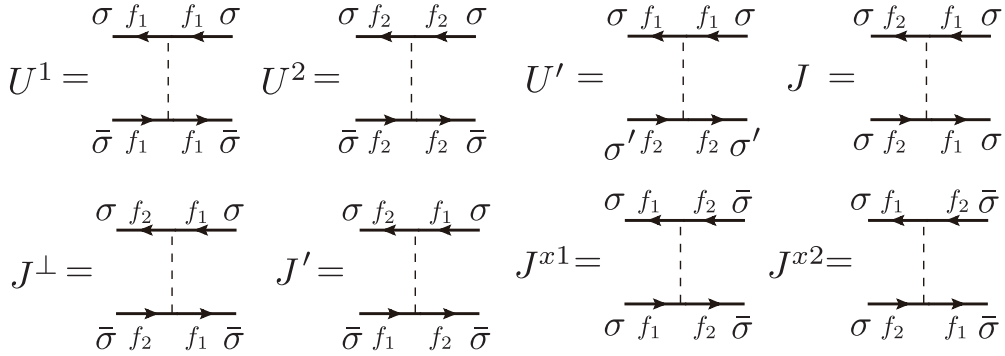


Figure 32: Definition of multi-orbital Coulomb interaction in the pseudo-spin representation; $U^1, U^2, U', J, J^\perp, J', J^{x1}$, and J^{x2} .

● key facts

- * 1 We consider 2-orbital PAM.
- * 2 s-f mixing has imaginary part due to SOI.
- * 3 Pseudo spin is conserved in 2D model with NN hopping.
- * 4 Coulomb interaction is expressed by s, s \perp and c-channel.

4.2 Multipole symmetry

In the present model in Eq.(4.1), there are 16-type active order parameters $Q(= 1 \sim 16)$ in the multipole basis. They are expressed as monopole (rank 0), dipole (rank 1), quadrupole (rank 2), octupole (rank

3), hexadecapole (rank 4) and dotriacontapole (rank 5) and classified into each irreducible representation (IR); ($\Gamma = A_1^+, A_2^+, E^+, A_1^-, A_2^-, E^-$) as shown in 1st, 2nd, 3rd-columns in TABLE 4 [13]. Each multipole operator \hat{O}^Q of rank k are composed of 4×4 tensor $J_q^{(k)}$ ($q = -k \sim k$) [8, 48] which is defined as

$$[J_{\pm}, J_q^{(k)}] = \sqrt{(k \mp q)(k \pm q + 1)} J_{q \pm 1}^{(k)} \quad (4.10)$$

$$J_k^{(k)} = (-1)^k \sqrt{\frac{(2k-1)!!}{(2k)!!}} J_+^k. \quad (4.11)$$

Detailed derivation of \hat{O}^Q from $J_q^{(k)}$ is given in Appendix E. The matrix representations of each \hat{O}^Q is summarized in 4th-column in TABLE 4. $\hat{\sigma}^\mu, \hat{\tau}^\mu$ ($\mu = x, y, z$) are Pauli matrix in the pseudo spin and orbital basis (f_1, f_2), respectively. $\hat{\sigma}^0, \hat{\tau}^0$ are identity matrix. They are classified into TRS even or odd as follows,

$$\{\sigma^0\}, \{\tau^0, \tau^z, \tau^x\} = \text{TRS even} \quad / \quad \{\sigma^z, \sigma^x, \sigma^y\}, \{\tau^y\} = \text{TRS odd} \quad (4.12)$$

Note that the present 2-orbital system has space inversion symmetry. Then, even (odd)-rank operators correspond to electric (magnetic) channel since they are time reversal even (odd). The 5th column in TABLE 4 shows corresponding pseudo spin channel of \hat{O}^Q , which is defined by Eq.(4.9).

IR(Γ)	rank(k)	multipole(Q)	matrix(\hat{O}^Q)	ch
A_1^+	0	$\hat{1}$	$\hat{\sigma}^0 \hat{\tau}^0$	c
	2	\hat{O}_{20}	$\hat{\sigma}^0 (2.00 \hat{\tau}^0 + 3.00 \hat{\tau}^z)$	
	4	\hat{H}_0	$\hat{\sigma}^0 (-5.73 \hat{\tau}^0 + 11.5 \hat{\tau}^z - 12.8 \hat{\tau}^x)$	
A_2^+	4	\hat{H}_z	$-19.8 \hat{\sigma}^z \hat{\tau}^y$	s
E^+	2	$\hat{O}_{yz(zx)}$	$-(+) 3.87 \hat{\sigma}^{x(y)} \hat{\tau}^y$	s_{\perp}
A_1^-	5	\hat{D}_4	$29.8i \hat{\sigma}^0 \hat{\tau}^y$	c
A_2^-	1	\hat{J}_z	$\hat{\sigma}^z (0.50 \hat{\tau}^0 + 2.00 \hat{\tau}^z)$	s
	3	\hat{T}_z	$\hat{\sigma}^z (9.00 \hat{\tau}^0 - 1.50 \hat{\tau}^z)$	
	5	\hat{D}_z	$-29.8 \hat{\sigma}^z \hat{\tau}^x$	
E^-	1	$\hat{J}_{x(y)}$	$-1.12 \hat{\sigma}^{x(y)} \hat{\tau}^x$	s_{\perp}
	3	$\hat{T}_{x(y)}$	$\hat{\sigma}^{x(y)} (3.75 \hat{\tau}^0 - 3.75 \hat{\tau}^z + 5.03 \hat{\tau}^x)$	
	5	$\hat{D}_{x(y)}$	$\hat{\sigma}^{x(y)} (23.0 \hat{\tau}^0 - 6.56 \hat{\tau}^z - 3.14 \hat{\tau}^x)$	

Table 2: Irreducible representation and 16-type active multipoles in the present 2-orbital model. Operator with rank k corresponds to 2^k -pole. Each operator is classified into s, s_{\perp} and c-ch.

Now, on-site Coulomb interaction in Eq.(4.5) is rewritten by using multipole;

$$U^{QQ'} = (\vec{O}^Q)^\dagger \hat{U} \vec{O}^{Q'}. \quad (4.13)$$

\vec{O}^Q is 16×1 vector, where $(\vec{O}^Q)_{4(L-1)+M}$ corresponds to $(\hat{O}^Q)_{L,M}$. In TABLE 3, obtained value for U^{QQ} is shown. The magnetic ch of the Coulomb interaction U^{QQ} ($Q = J, T, D$) is larger than electric ones ($Q = C, O, H$). For this reason, RPA can't explain electric phase, while higher-order many body effects bring various electric phase observed in transition metals, such as Fe-based compounds.

Q	C	O_{20}	H_0	H_z	$O_{yz(zx)}$	Q	J_z	T_z	$D_{z(4)}$	$J_{x(y)}$	$T_{x(y)}$	$D_{x(y)}$
U_0^Q	-1.3	-0.18	0.17	0.34	0.27	U_0^Q	0.56	0.44	0.55	0.49	0.49	0.50

Table 3: Normalized Coulomb interaction $U^Q (\equiv U^{QQ})$ for multipole channel Q .

● key facts

- * 1 There are 16 type active (independent) multipole orders Q .
- * 2 Even (odd)-rank of Q are classified into electric (magnetic) ch in aspect of TRS even (odd).
- * 3 Magnetic ch of Coulomb interaction is larger than electric ones.
- * 4 Higher rank of magnetic ch Coulomb interactions are large as well as dipole ones.

Method & Result

4.3 Green function

Here, we introduce 1-particle Green functions defined by Hamiltonian of Eq.(4.2). free c- and f-electron's Green functions without s-f mixing are given as

$$G^{0c}(k) = \frac{1}{i\epsilon_n - \epsilon_{\mathbf{k}} + \mu} \quad (4.14)$$

$$G_l^{0f}(k) = \frac{1}{i\epsilon_n - E_{l\mathbf{k}} + \mu} \quad (4.15)$$

By solving Dyson equation (Diagrammatic expression is in Fig.33), we obtain the Green functions

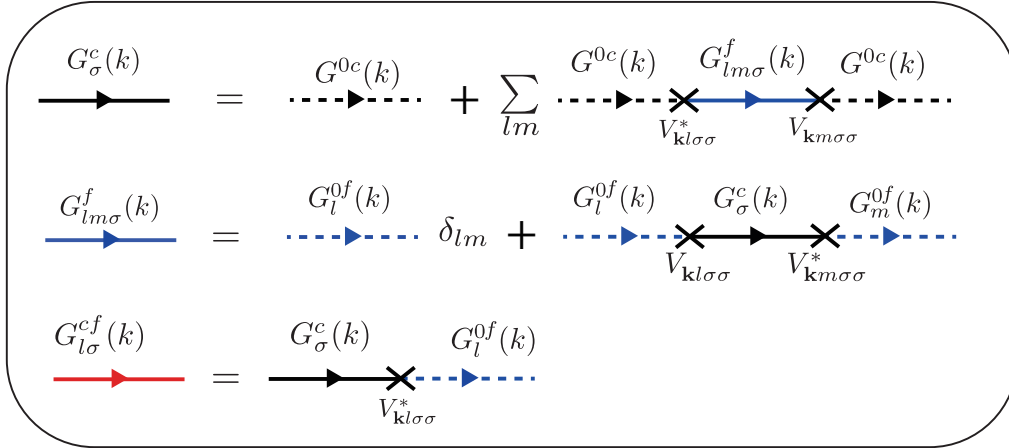


Figure 33: Dyson equation of the present model.

including s-f mixing;

$$G_\sigma^c(k) = G^{0c}(k) + G^{0c}(k) \sum_{lm} (V_{kl\sigma\sigma}^* G_{lm\sigma}^f(k) V_{km\sigma\sigma}) G^{0c}(k) \quad (4.16)$$

$$G_{lm\sigma}^f(k) = G_l^{0f}(k) \delta_{lm} + G_l^{0f}(k) V_{kl\sigma\sigma}^* G_\sigma^c(k) V_{km\sigma\sigma} G_m^{0f}(k) \quad (4.17)$$

$$G_{l\sigma}^{cf}(k) = G_\sigma^c(k) V_{kl\sigma\sigma}^* G_l^{0f}(k) \quad (4.18)$$

where (l, m) takes 1 or 2, $k = (\mathbf{k}, \epsilon_n) = (\mathbf{k}, (2n+1)\pi T)$ and μ is the chemical potential. In the present 2-orbital model, we neglect the self energy due to the strong Coulomb interaction among f -electrons. It works as renormalization factor for the energy scale of the electrons system. In this case, we need small Coulomb interaction compared with the present study. $V_{kl\sigma\sigma}^* V_{km\sigma\sigma}$ in Eq.(4.16) and (4.17) are given by

$$V_{kl\sigma\sigma}^* V_{km\sigma\sigma} = t_{sf}^l t_{sf}^m (-1)^{l+m} (\sin^2 k_y + \sin^2 k_x). \quad (4.19)$$

Then, we obtain

$$V_{\mathbf{k}l\uparrow\uparrow}^* V_{\mathbf{k}m\uparrow\uparrow} = V_{\mathbf{k}l\downarrow\downarrow}^* V_{\mathbf{k}m\downarrow\downarrow}. \quad (4.20)$$

For this reason, the Green functions G^c and G^f become independent of spin index:

$$\begin{aligned} G_{lm}^f(k) &\equiv G_{lm\uparrow}^f(k) = G_{lm\downarrow}^f(k), \\ G^c(k) &\equiv G_{\uparrow}^c(k) = G_{\downarrow}^c(k). \end{aligned} \quad (4.21)$$

We comment that $\hat{G}^f(k)$ is written by using $\hat{\sigma}$ and $\hat{\tau}$, which is described as

$$\hat{G}^f \propto \hat{\sigma}^0(\hat{\tau}^0 - c\hat{\tau}^x), \quad (4.22)$$

where c denotes the coefficient parameter. Therefore, $\hat{G}^f(k)$ is classified into electric ch based on Eq.(4.13).

● key facts

- * 1 Green functions with s-f mixing ($\hat{G}^f, \hat{G}^c, \hat{G}^{cf}$) are obtained by Dyson equation.
- * 2 \hat{G}^f and \hat{G}^c are independent of spin index.
- * 3 \hat{G}^f is proportion to $\hat{\sigma}^0(\hat{\tau}^0 - c\hat{\tau}^x)$.

4.4 Multipole susceptibility

In this section, we calculate f-electrons susceptibility in various way. First, the irreducible susceptibility (1-loop p-h excitation) is defined as

$$\chi_{ll'mm'}^0(q) = \int_0^\beta d\tau \left\langle T_\tau f_{\mathbf{k}l'\sigma}^\dagger(\tau) f_{\mathbf{k}+q\sigma}(\tau) f_{\mathbf{k}+q\sigma}^\dagger(0) f_{\mathbf{k}m'\sigma}(0) \right\rangle_{\hat{H}_0} \quad (4.23)$$

where $\omega_j = 2j\pi T$ is the Boson Matsubara frequency. T_τ is T -product for imaginary time τ , where $T_\tau A_{\tau_1} A_{\tau_2} = A_{\tau_1} A_{\tau_2} (\tau_1 > \tau_2), -A_{\tau_2} A_{\tau_1} (\tau_1 < \tau_2)$. By using the Green function, it is rewritten as

$$\chi_{ll'mm'}^0(q) = -T \sum_k G_{lm}^f(k+q) G_{m'l'}^f(k), \quad (4.24)$$

where $q = (\mathbf{q}, \omega_j) = (\mathbf{q}, 2j\pi T)$. Note that $\hat{\chi}^0(q)$ is independent of spin index due to the Eq.(4.15).

Next, we define total f -electrons susceptibility considering the Coulomb interaction in TABLE 1.

$$\chi_{ll'mm'}^{\sigma\sigma'\gamma\gamma'}(q) = \int_0^\beta d\tau \left\langle T_\tau f_{\mathbf{k}l'\sigma}^\dagger(\tau) f_{\mathbf{k}+q\sigma}(\tau) f_{\mathbf{k}+q\sigma}^\dagger(0) f_{\mathbf{k}m'\sigma}(0) \right\rangle_{\hat{H}_0 + \hat{H}_U} \quad (4.25)$$

If we use RPA, the total susceptibilities in the basis of pseudo spin channel (s, s_\perp, c) are given by

$$\hat{\chi}^{ch}(q) = \hat{\chi}^0(q) (\hat{1} - u\hat{U}^{ch} \hat{\chi}^0(q))^{-1}, \quad (4.26)$$

where $ch = s, s_\perp, c$. $\hat{\chi}^0(q)$, $\hat{\chi}^{ch}(q)$ and \hat{U}^{ch} are 4×4 matrices. The definition of \hat{U}^{ch} is given in Eq.(4.9). Here, we define the pseudo-spin Stoner factor α_S^{ch} as the largest eigenvalue of $u\hat{U}^{ch} \hat{\chi}^0(q)$, which is defined as

$$\lambda_{ch,q}^i \vec{x}_{ch,q}^i = u\hat{U}^{ch} \hat{\chi}^0(q) \vec{x}_{ch,q}^i, \quad (4.27)$$

$$\alpha_S \equiv \max_{ch} \{\alpha_{ch}\} \equiv \max_{q,i} \{\lambda_{ch,q}^i\}, \quad (4.28)$$

where $\lambda^i(\vec{x}^i)$ denotes the i -th eigenvalue (eigenvector) of Eq.(4.27) In the present model, each matrix element of \hat{U}^s and that of \hat{U}^{s_\perp} in TABLE 1 are the same except for $(lmlm)$ and $(llmm)$ elements. For this reason, $\hat{\chi}^s \approx \hat{\chi}^{s_\perp}$ and $\alpha_S^s \approx \alpha_S^{s_\perp}$ are satisfied.

● key facts

- * 1 Susceptibility $\hat{\chi}^{ch}$ and Stoner factor α_S^{ch} are defined for s, s_\perp, c -channel.

Now, we define the multipole susceptibility for Q ;

$$\chi^{Q,Q'}(q) \equiv \sum_{\substack{kl'l'mm' \\ \sigma\sigma'\gamma\gamma'}} \int_0^\beta d\tau \left\langle T_\tau f_{\mathbf{k}l'\sigma'}^\dagger(\tau) O_{l\sigma;l'\sigma'}^Q f_{\mathbf{k}+q,l\sigma}(\tau) f_{\mathbf{k}+q,m\gamma}^\dagger(0) O_{m'\gamma';m\gamma}^{Q'} f_{\mathbf{k}m'\gamma'}(0) \right\rangle e^{i\omega_j\tau}, \quad (4.29)$$

where $\sigma, \sigma', \gamma, \gamma'$ are indexes of pseudo spin. In the present 2D model,

$$\chi^{Q,Q'}(q) = 0 \quad \text{if } \Gamma \neq \Gamma' \quad (Q \in \Gamma, Q' \in \Gamma') \quad (4.30)$$

is satisfied. This fact is a great merit in analysis. On the other hand, in 3D models, $\chi^{Q,Q'}(q) \neq 0$ even if $\Gamma \neq \Gamma'$. In aspect of TRS, $\chi^{Q,Q'}$ is classified into magnetic (TRS odd) or electric (TRS even) channel, which is expressed as

$$\begin{aligned} \text{Magnetic ch: } & \chi^{Q,Q'}(q) \quad \text{for } Q, Q' \in A_1^+, A_2^+, E^+, \\ \text{Electric ch: } & \chi^{Q,Q'}(q) \quad \text{for } Q, Q' \in A_1^-, A_2^-, E^-, \end{aligned} \quad (4.31)$$

Note that the absolute value of $\chi^{Q,Q'}(q)$ becomes larger as rank of Q get higher. To compare among different rank of multipole susceptibilities, we define normalized multipole operator as

$$\hat{\Theta}^Q \equiv \hat{O}^Q / \sqrt{\text{Tr}(\hat{O}^Q \hat{O}^{Q*})}. \quad (4.32)$$

Then, the normalized susceptibility is given as

$$\chi_{\hat{\Theta}}^{Q,Q'}(q) \equiv \chi^{Q,Q'}(q) \quad (\hat{O}^Q, \hat{O}^{Q'} \text{ in Eq.(4.29)} \rightarrow \hat{\Theta}^Q, \hat{\Theta}^{Q'}) \quad (4.33)$$

In addition, we define 16×16 multipole susceptibility $\hat{\chi}^{Q,Q'}(q)$ with orbital and pseudo spin indexes,

$$\begin{aligned} \chi_{ll'mm'}^{Q,Q'\sigma\sigma'\gamma\gamma'}(q) & \equiv a^{Q,Q'}(q) O_{l\sigma;l'\sigma'}^Q O_{m'\gamma';m\gamma}^{Q'}, \\ \Leftrightarrow \hat{\chi}^{Q,Q'}(q) & \equiv a^{Q,Q'}(q) \vec{O}^Q \vec{O}^{Q'\dagger}, \end{aligned} \quad (4.34)$$

where $a^{Q,Q'}(q)$ is calculated as follows. First, we solve the following characteristic equation;

$$\hat{\chi}(q) \vec{v}^i(q) = \lambda^i(q) \vec{v}^i(q), \quad (4.35)$$

where $\lambda^i(q)$ is i -th real eigen value ($i = 1 \sim 16$). $\vec{v}^i(q)$ is 16-dimensional eigen vector normalized as $|\vec{v}^i| = 1$. In the present model, $\vec{v}^i(q)$ is uniquely characterized by IR. Then, $\vec{v}^i(q)$ for $i \in \Gamma$ is expanded in the basis of the multipole matrices as follows;

$$\vec{v}^i(q) = \sum_{Q \in \Gamma} b^{i,Q}(q) \vec{O}^Q \quad i \in \Gamma, \quad (4.36)$$

where the coefficient $b^{i,Q}(q)$ is uniquely determined. Note that $\{\vec{O}^Q\}$ forms complete basis but not orthogonal basis within the same Γ . Then, $a^{Q,Q'}$ is given by

$$a^{Q,Q'}(q) = \sum_{i \in \Gamma} b^{i,Q}(q) \lambda^i(q) b^{i,Q'*}(q). \quad (4.37)$$

As a result, $\hat{\chi}^{Q,Q'}(q)$ in Eq.(4.34) is obtained. $\hat{\chi}(q)$ is reproduced as

$$\hat{\chi}(q) = \sum_{Q,Q'} \hat{\chi}^{Q,Q'}(q) \quad (4.38)$$

We note that $\hat{\chi}^{Q,Q'}(q)$ is independent of normalized condition of the multipole operator \hat{O}^Q since it reproduce 16×16 matrix form of $\hat{\chi}(q)$. It is a great merit in analysis.

multipole susceptibilities	$\chi^{Q,Q'}(q)$	$\chi_{\Theta}^{Q,Q'}(q)$	$\hat{\chi}^{Q,Q'}(q)$
Indexes	q, Q, Q'		q, Q, Q', l, σ
Rank dependence	depend	in-depend	
Normalized condition dependence	depend		in-depend

● key facts

- * 1 3-types of multipole susceptibilities $\chi^{Q,Q'}$, $\chi_{\Theta}^{Q,Q'}$ and $\hat{\chi}^{Q,Q'}$ are obtained.
- * 2 In the case of $\Gamma \neq \Gamma'$, $\chi^{Q,Q'}$, $\chi_{\Theta}^{Q,Q'}$, $\hat{\chi}^{Q,Q'}$ go to zero for $Q \in \Gamma, Q' \in \Gamma'$.
- * 3 It is convenient to use $\chi_{\Theta}^{Q,Q'}$ for comparing among different rank multipole susceptibilities.
- * 4 $\hat{\chi}^{Q,Q'}$ is uniquely determined independently of normalized condition of \hat{O}^Q .

Here, we perform RPA based on multi orbital PAM introduced in Sec.4. In this calculation, we use 32×32 \mathbf{k} -meshes and 128 Matsubara frequencies.

In Fig.34(a), we show \mathbf{q} -dependence of $\chi^{Q,Q'}(\mathbf{q}, 0)$ at $u = 0.31$ ($\alpha_S = 0.90$) for the magnetic dipole ch as Q, Q' ; $\chi^{J_z, J_z}(\mathbf{q}, 0) \in A_2^-$ and $\chi^{J_x, J_x}(\mathbf{q}, 0) \in E^-$. We find that $\chi^{J_z, J_z}(\mathbf{q}, 0)$ is much larger than $\chi^{J_x, J_x}(\mathbf{q}, 0)$ at $\mathbf{q} = (0, 0)$ while they are almost the same around the peak at $\mathbf{q} \simeq (\pi/2, \pi/2)$. Thus, the uniform magnetic susceptibility shows strong Ising anisotropy, which is actually observed in CeCu₂Si₂. We verified that the peak at $\mathbf{q} \simeq (\pi/2, \pi/2)$ originates from nesting vector on the large Fermi surface as shown in Fig.31. In this result, α_S is given by magnetic (=odd-rank) susceptibility $\chi^{Q,Q'}(\mathbf{q}, 0)$ for $Q, Q' \in A_2^-$, that is, $\alpha_S = \alpha_{A_2^-}$. The relation $1 \gtrsim \alpha_{A_2^-} \gtrsim \alpha_{E^-}$ is satisfied.

Next, we calculate $\chi_{\Theta}^{Q,Q'}(q)$ to compare among the different ranks of multipole susceptibility. In Fig.34(b), we show α_S dependences of the maximum value of magnetic multipole susceptibilities $\tilde{\chi}_{\max}^Q \equiv \max_{\mathbf{q}} \{\chi_{\Theta}^{Q,Q'}(\mathbf{q}, 0)\}$. α_S linearly increases in proportion to u . The most divergent $\tilde{\chi}_{\max}^Q$ is that for $Q = T_x$. This fact is consistent with RPA result based on the first-principles model in Ref[28]. Secondly, $\tilde{\chi}_{\max}^Q$ for $Q = D_z, J_x, T_z, D_4$ is also strongly enlarged. Therefore, various magnetic multipole (including higher-rank) susceptibilities are simultaneously enlarged in RPA. This is a characteristic feature of f -electron systems with strong SOI [13]. We find that the inter-rank magnetic multipole susceptibilities, such as $\chi_{\Theta}^{J_z, T_z}$, are also enlarged.

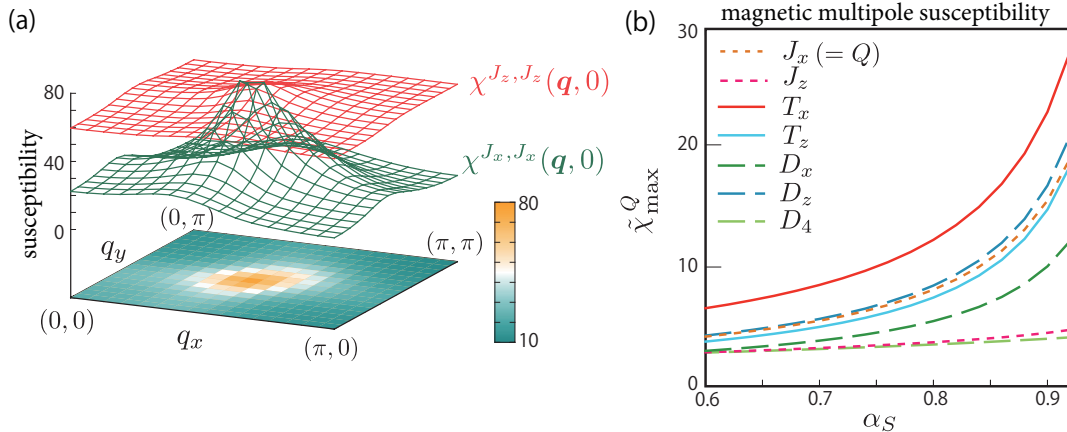


Figure 34: (a) \mathbf{q} dependence of the magnetic dipole susceptibility. $\chi^{J_z, J_z}(\mathbf{q}, 0) \gg \chi^{J_x, J_x}(\mathbf{q}, 0)$ is satisfied at $\mathbf{q} = (0, 0)$. (b) α_S dependence of magnetic multipole susceptibility. Higher-rank magnetic multipole susceptibilities are strongly enlarged as well as dipole ones.

● key facts

- * 1 We obtain Ising-like dipole susceptibility $\chi^{J_z, J_z}(\mathbf{q}, 0) \gg \chi^{J_x, J_x}(\mathbf{q}, 0)$ at $\mathbf{q} = (0, 0)$, while they are almost the same around the peak at $\mathbf{q} \simeq (\pi/2, \pi/2)$.
- * 2 Higher-ranks magnetic multipole fluctuations develop due to the strong SOI.

4.5 Phonon mediated interaction

In this section, we introduce A_1^+ (= identical representation) phonon mediated interaction. The effective interaction is introduced by

$$\hat{V}^{\text{Ph}} = 2g(\omega_j)\vec{C}_{A_1^+}\vec{C}_{A_1^+}^\dagger, \quad (4.39)$$

$$g(\omega_j) \equiv \tilde{g} \frac{\omega_D^2}{\omega_D^2 + \omega_j^2}, \quad (4.40)$$

where \hat{V}^{Ph} is 16×16 matrix and $\tilde{g} = \frac{2\eta^2}{\omega_D} (> 0)$. ω_D is the phonon frequency. η is the coupling constant between electrons and phonon. $\hat{C}_{A_1^+}$ is the 16×1 tensor where $(\vec{C}_{A_1^+})_{4(L-1)+M} \equiv (\hat{C}_{A_1^+})_{L,M}$ for $L = (l, \sigma)$. $\hat{C}_{A_1^+}$ is given by a linear combination of multipole operators belong to A_1^+ in TABLE 4. It is expressed as

$$\hat{C}_{A_1^+} \equiv \hat{\sigma}^0(\alpha\hat{\tau}^0 + \beta\hat{\tau}^z + \gamma\hat{\tau}^x), \quad (4.41)$$

which includes monopole $\hat{1}$, quadrupole \hat{O}_{20} and hexadecapole \hat{H}_0 . For instance, the A_1^+ interaction can be induced by oscillation of c -axis length [49]. The schematic picture of the A_1^+ oscillation is shown in Fig.35. In the present study, we drop ω_j -dependence of $g(\omega_j)$ for simplicity, that is, we neglect the retardation effect. This fact leads to underestimation of the attractive superconducting pairing interaction or T_c of s -wave SC phase as discussed in Sec.3. Note that T_c of s -wave SC will increase, if the retardation effect is considered. In this case, the bare Coulomb interaction \hat{U} is replaced with \hat{U}^{eff} ;

$$u\hat{U} \rightarrow u\hat{U} + 2g(0)\vec{C}_{A_1^+}\vec{C}_{A_1^+}^\dagger. \quad (4.42)$$

This replacement enhance electric (=even-rank) multipole fluctuations since the A_1^+ interaction is classified into even-rank multipole interaction. On the other hand, the magnetic (=odd-rank) multipole susceptibilities are independent of the phonon mediated interaction.

Hereafter, we mainly show the numerical result of $(\alpha, \beta, \gamma) = (0, 1, -1)$. We verified that the main results are qualitatively same as those of $(\alpha, \beta, \gamma) = (0, 1, 1)$.

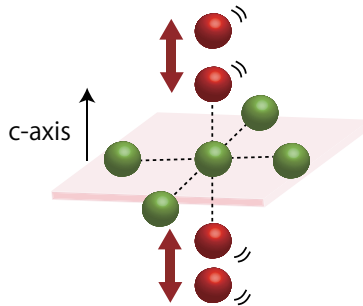


Figure 35: (a) Schematic picture of A_1^+ phonon mediated interaction.

● key facts

- * 1 We consider A_1^+ phonon mediated interaction.
- * 2 A_1^+ interaction induces electric ($\hat{1}, \hat{O}_{20}, \hat{H}_0$) multipole fluctuations.
- * 3 We neglect retardation effect.
- * 4 Attractive pairing interaction will be enhanced if retardation effect is considered.

4.6 SC gap equation

In this section, we introduce SC gap equation in Migdal-Eliashberg approximation. First, we define SC paring interaction \hat{V}^{ch} in $s, s\perp, c$ basis, which is given as

$$\hat{V}^{ch}(q) \equiv u^2 \hat{U}^{ch} \hat{\chi}^{ch}(q) \hat{U}^{ch} + u \hat{U}^{ch}. \quad (4.43)$$

Then, pseudo spin-singlet paring interaction \hat{V}^{sing} is given by

$$\hat{V}^{\text{sing}}(q) = \hat{V}^{\text{s}\perp}(q) + \frac{1}{2} \hat{V}^s(q) - \frac{1}{2} \hat{V}^c(q) - u \hat{U}^{\text{s}\perp}. \quad (4.44)$$

The 4th terms is needed to avoid double counting. Therefore, the linearized gap equation in the orbital basis is given by

$$\lambda \Delta_{ll'}(k) = -T \sum_{k', mm' nn'} G_{mn}^f(k') G_{m'n'}^f(-k') \Delta_{nn'}(k') V_{lmm'l'}^{\text{sing}}(k - k'), \quad (4.45)$$

where $\Delta_{ll'}(k)$ is the gap function and λ is the eigenvalue. Note that $\lambda = 1$ at $T = T_c$. The diagrammatic expression of the gap equation is shown in Fig.36. In Eq.(4.45), V^s and $V^{\text{s}\perp}$ bring sign change between $\Delta(k)$ and $\Delta(k')$, while uniform (S-wave) gap function is favorable for V^c .

Next, we derive the gap equation in the band basis, which is given by

$$\lambda \Delta_a(k) = -T \sum_{k', b} G_b(k') G_b(-k') \Delta_b(k') V_{ab}^{\text{sing}}(k, k'), \quad (4.46)$$

where a, b is band index. After the integration along energy-axis, we obtain

$$\lambda \Delta(\mathbf{k}, \epsilon_n) = -\frac{\pi T}{(2\pi)^2} \sum_{\epsilon_m} \oint \frac{d\mathbf{k}'}{v_{\mathbf{k}'}} \frac{\Delta(\mathbf{k}', \epsilon_m)}{|\epsilon_m|} V^{\text{sing}}(k, k'), \quad (4.47)$$

where $\Delta(\mathbf{k}, \epsilon_n)$ is the gap function on Fermi surface and $v_{\mathbf{k}}$ is Fermi velocity. Here, the band index is omitted since we consider 1-band system as shown in Fig.31. The band basis paring interaction in Eq.(4.47) is obtained as follows,

$$V^{\text{sing}}(k, k') \equiv V^{\uparrow\downarrow\uparrow\downarrow}(k, k') - V^{\uparrow\uparrow\downarrow\downarrow}(k, k') \quad (4.48)$$

where \uparrow or \downarrow denote pseudo-spin of the Kramers doublet in the Bloch function. $V^{\uparrow\downarrow\uparrow\downarrow}(\uparrow\uparrow\downarrow\downarrow)$ is obtained by performing the unitary transformation of the paring interaction in the orbital basis;

$$V^{\uparrow\downarrow\uparrow\downarrow}(\uparrow\uparrow\downarrow\downarrow)(k, k') = \sum_{ll'mm'} \sum_{\sigma\sigma'\gamma\gamma'} V_{ll'mm'}^{\sigma\sigma'\gamma\gamma'}(k, k') u_{l\sigma}^{\uparrow*}(\mathbf{k}) u_{m'\lambda'}^{\downarrow*}(-\mathbf{k}) u_{m\lambda}^{\uparrow(\downarrow)}(-\mathbf{k}') u_{l'\sigma'}^{\downarrow(\uparrow)}(\mathbf{k}'), \quad (4.49)$$

where $u_{l\sigma}^{\uparrow(\downarrow)}(\mathbf{k})$ is the unitary matrix connecting between $f_{\mathbf{k}l\sigma}^{\uparrow}$ and the quasi-particle creation operator $f_{\mathbf{k}\uparrow(\downarrow)}^{\uparrow}$. In the presence of the time reversal symmetry, following relation is satisfied [50];

$$u_{l\sigma}^{\uparrow}(-\mathbf{k}) = (2\delta_{\uparrow\sigma} - 1) u_{l\bar{\sigma}}^{\downarrow}(\mathbf{k})^*. \quad (4.50)$$

To understand the result of Eq.(4.48) intuitively, we consider a simple system without SOI. In this case, $u_{l\sigma}^{\uparrow(\downarrow)}(\mathbf{k}) = \delta_{\uparrow(\downarrow), \sigma} \bar{u}_l(\mathbf{k})$. Then, we replace Eq.(4.48) with

$$V^{\text{sing}}(k, k') = \left\{ \hat{V}^{\text{s}\perp}(k, k') + \frac{\hat{V}^s(k, k')}{2} - \frac{\hat{V}^c(k, k')}{2} \right\} \bar{u}_l^*(\mathbf{k}) \bar{u}_{m'}(\mathbf{k}) \bar{u}_m^*(\mathbf{k}') \bar{u}_{l'}(\mathbf{k}'); \text{witout SOI.}$$

Here, we obtain similar expression as Eq.(4.44), if we neglect the effect of SOI in the unitary transformation matrix u . In conclusion, s and $s\perp$ -channel interaction work as repulsive interaction, while c -channel one works as attraction.

Finally, we define the multipole-decomposed SC paring interaction in the same way as $\hat{\chi}^{Q, Q'}$ in Eq.(4.34). It is expressed as

$$\hat{V}^{ch, QQ'}(q) \equiv d^{ch, Q, Q'}(q) \vec{O}^Q \vec{O}^{Q'\dagger} \left(\hat{V}^{QQ'}(q) \equiv d^{Q, Q'}(q), \vec{O}^Q \vec{O}^{Q'\dagger} \right), \quad (4.51)$$

where $d^{Q,Q'}(q), d'^{Q,Q'}(q)$ is obtained by solving the characteristic equation;

$$\hat{V}^{ch}(q)\vec{v}^{i,ch}(q) = \lambda^{i,ch}(q)\vec{v}^{i,ch}(q), \quad \left(\hat{V}(q)\vec{v}^i(q) = \lambda^i(q)\vec{v}^i(q)\right) \quad (4.52)$$

Note that $\hat{V}^{ch,QQ'} = 0$ for $ch \notin \Gamma$ in the case of $Q, Q' \in \Gamma$.

Figure 36: The linearized gap equation within Migdal-Eliashberg approximation. Blue rectangles show bare Coulomb interaction U .

● key facts

- * 1 We define linearized gap equation in Migdal-Eliashberg approximation.
- * 2 s, s_{\perp} -ch (c -ch) interaction works as repulsive (attractive) pairing interaction.
- * 3 SC pairing interaction is decomposed into multipole ch.

4.7 U -VC

In this section, we consider higher order many body effects beyond Migdal Eliashberg approximation. They are expressed as the 3-point vertex correction for bare Coulomb interaction U . Therefore, we call the vertex corrections U -VC. In the present model, U -VC satisfy the pseudo-spin conservation. Thus, the pairing interaction for s, s_{\perp}, c -channel in Eq.(4.44) is replaced with

$$\hat{V}_{U-VC}^{ch}(k, k') = \hat{\Lambda}_{k,k'}^{ch} \hat{V}^{ch}(k - k') \hat{\Lambda}_{-k, -k'}^{ch\dagger}, \quad (4.53)$$

$$(\hat{\Lambda}_{k,k'}^{ch\dagger})_{l'l'mm'} \equiv (\hat{\Lambda}_{k,k'}^{ch})_{m'm'l'l}. \quad (4.54)$$

Here, $\hat{V}^{ch}(q)$ is given in Eq.(4.43). $\hat{\Lambda}_{k,k'}^{ch}$ is the enhancement factor due to AL-type U -VC given by $\hat{L}_{k,k'}^{ch}$, whose diagrammatic expression is shown in Fig.37. In the present study, MT-type U -VC is negligible compared to AL-type one. For this reason, we calculate only AL-type U -VC.

$$(\hat{\Lambda}_{k,k'}^{ch})_{l'l'mm'} = \delta_{lm} \delta_{l'm'} + (\hat{L}_{k,k'}^{ch})_{l'l'mm'}. \quad (4.55)$$

The 2nd term is neglected within Migdal-Eliashberg approximation. Analytic expression of $\hat{L}_{k,k'}^{ch}$ is given as

$$(\hat{L}_{k,k'}^{ch})_{l'l'mm'} \equiv \frac{T}{2} \sum_{p, abcdef} \sum_{ch1, ch2} B_{abcdef}^{mm'}(k - k', p) a_{ch1, ch2}^{ch} V_{lacd}^{ch1}(k - k' + p) V_{bl'ef}^{ch2}(-p), \quad (4.56)$$

$$\Leftrightarrow \hat{L}_{k,k'}^{ch} = \frac{T}{2} \sum_{p, ch1, ch2} a_{ch1, ch2}^{ch} \hat{B}(k - k', p) \hat{V}^{ch1}(k - k' + p) \hat{V}^{ch2}(-p). \quad (4.57)$$

where

$$\left\{ \begin{aligned} B_{abcdef}^{mm'}(q, p) &= \frac{1}{4} G_{ab}^f(k' - p) \left\{ C_{cdef}^{mm'}(q, p) + C_{efcd}^{mm'}(q, q + p) \right\}, \\ C_{cdef}^{ab}(q, p) &= -T \sum_{k'} G_{ca}^f(k' + q) G_{bf}^f(k') G_{ed}^f(k' - p). \end{aligned} \right. \quad (4.58)$$

Here, $a \sim f$ are orbital indices while p denotes wave number. $a_{ch1, ch2}^{ch}$ is coefficient parameter where

$$(a_{s,s}^c, a_{s_{\perp}, s_{\perp}}^c, a_{c,c}^c) = (1, 2, 1) \quad (4.59)$$

Then, we obtain

$$\hat{L}^c \propto \hat{V}^s \hat{V}^s + 2\hat{V}^{\text{sl}} \hat{V}^{\text{sl}} + \hat{V}^c \hat{V}^c. \quad (4.60)$$

We comment that $\hat{V}^s \hat{V}^s + 2\hat{V}^{\text{sl}} \hat{V}^{\text{sl}}$ becomes large near magnetic QCP due to the development of spin fluctuations. In conclusion, charge-ch of U -VC is enlarged by the square of spin fluctuations $O(\{\chi^{s(\text{sl})}\}^2)$ near magnetic QCP. We call this nontrivial effect "mode-coupling" between spin and charge channel, which is originate from many body effects beyond Migdal-Eliashberg approximation.

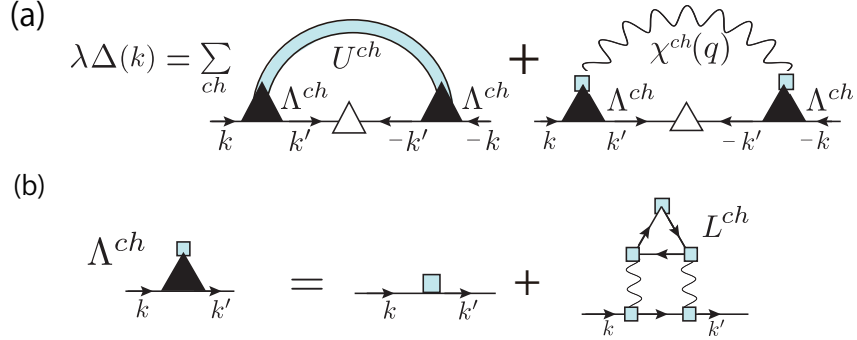


Figure 37: (a) Linearized gap equation in the present study. The black triangle shows 3-point vertex correction (U -VC). (b) U -VC due to the AL process.

Next we define multipole-decomposed U -VC, which is expressed

$$(\hat{\Lambda}_{k,k'}^{ch,QQ'})_{ll'mm'} = \delta_{lm}\delta_{l'm'} + (\hat{L}_{k,k'}^{ch,QQ'})_{ll'mm'} \quad (4.61)$$

By replacing \hat{V}^{ch} in Eq.(7.7) with $\hat{V}^{ch,Q}$, we obtain

$$\hat{L}_{k,k'}^{ch,QQ'} \equiv \frac{T}{2} \sum_{ch1,ch2} a_{ch1,ch2}^{ch} \hat{B}(k-k',p) \left\{ \hat{V}^{ch1,Q}(k-k'+p) \hat{V}^{ch2,Q'}(-p) + \frac{Q \rightarrow Q'}{Q' \rightarrow Q} \right\}. \quad (4.62)$$

The diagrammatic expression of Eq.(4.63) is given in Fig.38(a). Note that

$$\hat{L}_{k,k'}^{ch} \approx \sum_{\{Q,Q'\}} \hat{L}_{k,k'}^{ch,QQ'}. \quad (4.63)$$

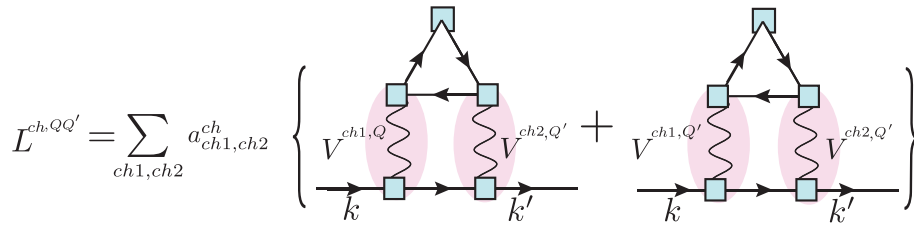


Figure 38: Multipole-decomposed U -VC for Q, Q' .

● key facts

- * 1 We consider AL-type U -VC beyond Migdal Eliashberg approximation.
- * 2 Charge-ch of U -VC is enlarged by spin fluctuations $\propto (\chi^s)^2$ near magnetic QCP.
- * 3 U -VC can be expressed in multipole basis as well as spin basis.

Here, we show numerical results of U -VC. In this calculation, we use 16×16 \mathbf{k} -meshes and 128 Matsubara frequencies. In Figs.39 (a) and (b), we show the α_S dependence of maximum value of the enhancement factor on the Fermi surface,

$$\hat{\Lambda}^{ch,\max} \equiv \max_{\mathbf{k},\mathbf{k}'} |\hat{\Lambda}_{\mathbf{k},\mathbf{k}'}^{ch}| \quad (\epsilon_n = \epsilon_{n'} = \pi T), \quad (4.64)$$

Note that $\Lambda_{ll'mm'}^{ch,max} = \Lambda_{l'l'm'm'}^{ch,max}$ is satisfied. We plot only charge-ch U -VC ($\hat{\Lambda}^c$) since it is much larger than spin-ch one near the magnetic QCP. In the present numerical study, we put $g = 0$ in $\hat{\Lambda}^{ch}$, since the contribution from χ^c is negligibly smaller than that from χ^s and χ^{sl} [35]. Obtained results show that U -VC work as large enhancement factors for the charge-ch coupling constant ($|\hat{\Lambda}^c| \gg 1$) near the magnetic QCP ($\alpha_S \lesssim 1$). This behavior originates from the relation

$$\hat{\Lambda}_{k,k'}^c \propto \sum_p \hat{\chi}^s(k-k'+p)\hat{\chi}^s(p) + 2\hat{\chi}^{sl}(k-k'+p)\hat{\chi}^{sl}(p).$$

This is qualitatively similar to d -electron systems without SOI as shown in Sec.3. In conclusion, U -VC in f -electron systems give significant contribution as well as in d -electron systems.

On the other hand, there are some significant differences from d -electron systems. In fact, in the present f -electron system, (i) various orbital components of U -VC are equally enlarged, and (ii) the magnitude of U -VC are even larger than in d -electron systems at the same α_S . These results originate from higher-rank magnetic multipole fluctuations as shown below.

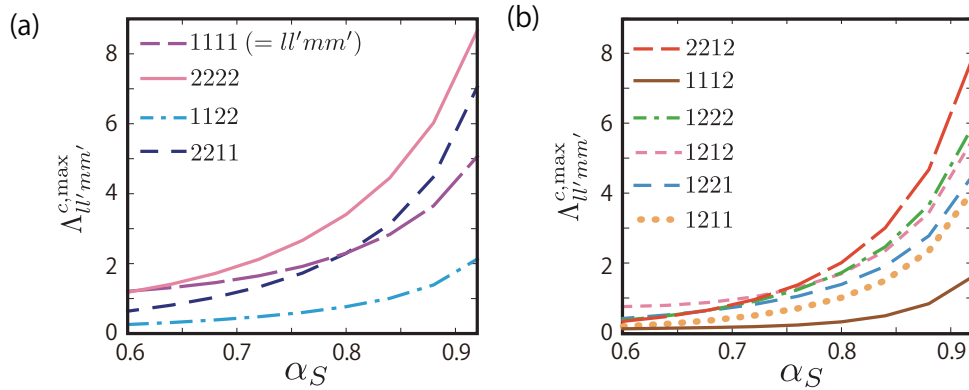


Figure 39: (a) (b) α_S dependence of charge-channel U -VC. Various orbital components are enlarged near the magnetic QCP ($\alpha_S \lesssim 1$).

Next we show the obtained result in Figs.40(a)-(d), we show the maximum of multipole-decomposed U -VC defined as

$$\hat{\Lambda}^{ch,QQ'} \equiv \max_{\mathbf{k},\mathbf{k}'} |(\hat{\Lambda}_{\mathbf{k},\mathbf{k}'}^{ch,QQ'})| \quad (\epsilon_n = \epsilon_{n'} = \pi T) \quad (4.65)$$

We consider only magnetic(=odd rank) multipole ch for Q, Q' since the contributions from electric multipole ch are negligibly small within RPA. Note that $\hat{\Lambda}^{c,QQ'} = 0$ if $\Gamma \neq \Gamma'$ for $Q(Q) \in \Gamma(\Gamma')$ in the present model. Figures 40(a) and (b) show the orbital-diagonal component of U -VC given by $\Lambda_{2222}^{c,QQ'}$. It has peak at $(Q, Q') = (T_x, T_x)$. Subsequently, $(Q, Q') = (J_z, T_z), (T_z, T_z), (D_z, D_z)$ are also enlarged. In Figs.40(c) and (d), we show orbital-off-diagonal component given by $\Lambda_{1211}^{c,QQ'}$. It takes large value for $(Q, Q') = (T_x, D_x), (T_z, D_z), (D_z, D_z), (T_x, T_x), (J_z, D_z)$. Therefore, higher-ranks of multipole fluctuations lead to the strong enhancement of U -VC.

To summarize the obtained result, both orbital-diagonal and off-diagonal components of charge-channel U -VC are enlarged. In addition, higher-ranks of multipole fluctuations contribute to the enhancement of U -VC. These facts lead to above-mentioned differences (i) and (ii) unlike $3d$ -electron system. Thus, we conclude that the U -VC in f -electron system plays more significant roles due to the strong SOI compared with d -electron systems.

● key facts

- * 1 Charge channel pairing interaction is enhanced by U -VC.
- * 2 Various orbital components of U -VC are equally enlarged.
- * 3 Higher-ranks of multipole fluctuations contribute to the enhancement of U -VC.

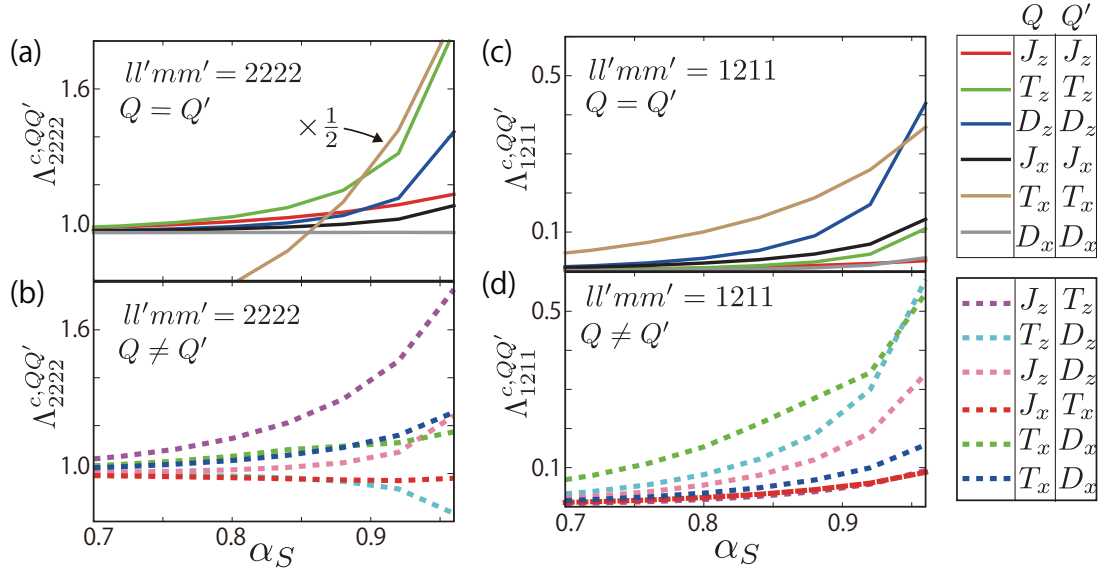


Figure 40: (a)(c) Obtained U -VC for $Q = Q'$ and (b)(d) $Q \neq Q'$, higher-ranks of multipole fluctuations contribute to the enhancement of U -VC.

4.8 SC phase diagram

Now, we show obtained superconducting phase diagram by solving the gap equation in Eq.(4.47). We solve the gap equation in the presence of both u and g , by the following replacement,

$$u\hat{U} \rightarrow u\hat{U} + 2g(0)\vec{C}_{A_1^+}\vec{C}_{A_1^+}^\dagger \quad (4.66)$$

in $\hat{V}(k - k')$ in Eq.(4.53). Figures 41(a)-(b) are obtained phase diagrams, which is given by the largest eigenvalue and symmetry of eigenvector. In the presence of U -VC, fully gapped s -wave state without any sign reversal emerges when $\alpha_S \lesssim 1$ and $\alpha_C \lesssim 1$ as shown in Fig.41(a). The region of s -wave phase gets wider as the magnetic fluctuations develop. These results originate from the fact that the charge-channel attractive interaction is strongly enhanced by the charge-channel U -VC, which is enlarged due to the magnetic (odd-rank) multipole fluctuations when $\alpha_S \lesssim 1$. In fact, charge-channel attractive interaction is expressed as

$$-\frac{1}{2}\hat{V}_{U-VC}^c \propto -\frac{1}{2}|\hat{\Lambda}^c|^2\{\hat{U}^c\hat{\chi}^c\hat{U}^c + \hat{U}^c\}, \quad (4.67)$$

which takes large negative (=attractive) value when $\alpha_C \lesssim 1$ [35]. In addition, we find that quite small $g(0)$ is enough for realizing the s -wave superconductivity. For instance, s -wave state emerges even at $g(0) = 0.025$. This is much smaller than Coulomb interaction $u = 0.31$ at $\alpha_S = 0.9$. Obtained gap functions of s -wave states is almost isotropic as shown in Fig.41(b).

In contrast, the s -wave region in Fig.41(a) is drastically reduced if we neglect U -VC as shown in Fig.41(c). In this case, $d_{x^2-y^2}$ -wave state appears in wide parameter region. Obtained gap functions of $d_{x^2-y^2}$ -wave state is expressed in Fig.41 (d). It has accidental nodes in addition to the symmetry nodes. Furthermore, the eigenvalue λ for $d_{x^2-y^2}$ -wave state in Fig.41(c) is much smaller than that for s -wave state in Fig.41(a), so T_c of $d_{x^2-y^2}$ -wave state should be low. We comment that the obtained large eigenvalues λ in Fig.41 (a),(c) are overestimated since the self-energy effects (such as the mass-renormalization and the quasi particle damping) are dropped in the gap equation. Then, realistic T_c should be lower than obtained result.

In conclusion, once the small electron-phonon interaction exist, fully gapped s -wave superconducting state appears in f -electron system near the magnetic QCP. This counter-intuitive result is given by the large U -VC caused by multiple (higher-rank) multipole fluctuations.

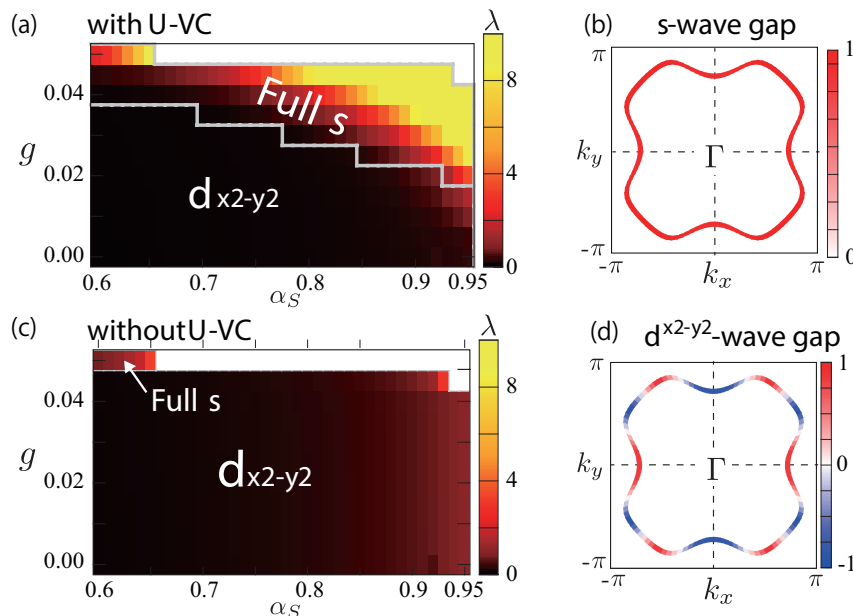


Figure 41: (a) Phase diagram in the presence of U - VC . The s -wave state emerges due to the significant contribution from U - VC . The white region corresponds to $\alpha_C > 1$. (b) The gap function on Fermi surface for s -wave state. (c) Phase diagram in the absence of U - VC . Anisotropic $d_{x^2-y^2}$ -wave state appears in wide parameter region. (d) The gap function for $d_{x^2-y^2}$ -wave.

● key facts

- * 1 Fully gapped s -wave SC phase appears near magnetic QCP due to U - VC .
- * 2 Small el-ph coupling is enough to realize s -wave SC state ($g(0) \gg u$).

Discussion

4.9 CEF splitting and f - f hopping

Here, we discuss CEF splitting ΔE between f_1 and f_2 -orbitals, which is given by

$$\Delta E \equiv E_1 - E_2 \quad (4.68)$$

as shown in Fig.42(a). Furthermore, we recall that $|f_1\rangle$ and $|f_2\rangle$ have different itinerancy. $|f_1\rangle$ is relatively itinerant while $|f_2\rangle$ is relatively localized. Therefore, obtained DoS at the Fermi level: $D^{f_i}(0)$ behaves as shown in Fig.42(b). The ratio $D^{f_1}(0)/D^{f_2}(0)$ is much larger than unity at $\Delta E = 0$. Then, the ratio decreases with ΔE . At $\Delta E \simeq 0.12$, the ratio reaches unity.

In Fig.42(c) and (d), we show obtained phase diagram at $\Delta E = 0.06$ and $\Delta E = 0.12$, respectively. The region of s -wave state at $\Delta E = 0.12$ is much wider than that at $\Delta E = 0.06$, which means that s -wave state is favored as ΔE increases. As a result, the condition $D^{f_1}(0) \approx D^{f_2}(0)$ is significant for realizing the s -wave superconducting state. In other words, the multi-orbital nature on Fermi surface is important for realizing s -wave states. Therefore, the s -wave state emerges in the presence of finite CEF splitting of f -levels when the s - f hybridization has orbital dependence. This situation is expected to be realized in CeCu_2Si_2 at $P = 0$ [25].

Next, we discuss the effects of f - f hopping. In the previous sections, we neglected f - f hopping. Here, we introduce the orbital-dependent f - f hopping. In this case, f -electron energy E_l have \mathbf{k} -dependence. As a result, the f_l -orbital weight comes to have θ -dependence on the Fermi surface. The f - f hopping is expressed as

$$\hat{H}_{ff} = \sum_{kl\sigma} E_{lk} f_{kl\sigma}^\dagger f_{kl\sigma}. \quad (E_{lk} = E_l - (-1)^l \delta E_{\mathbf{k}}). \quad (4.69)$$

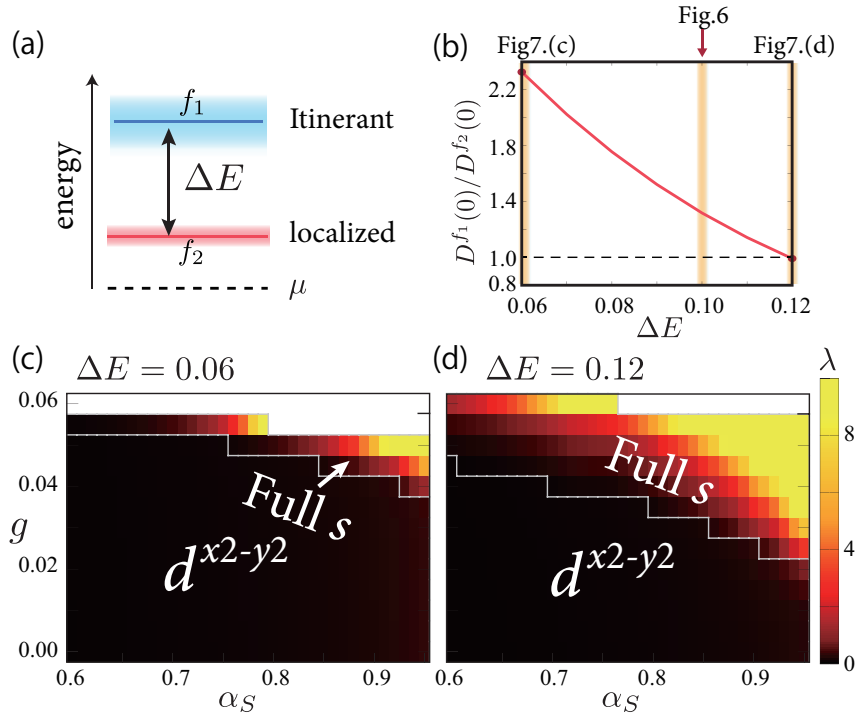


Figure 42: (a) The energy level of the f -orbital states in the present model. (b) ΔE dependence of the ratio of the DoS $D^{f_1}(0)/D^{f_2}(0)$. The ratio goes to unity at $\Delta E \simeq 0.12$. Obtained phase diagram at (c) $\Delta E = 0.06$ and (d) $\Delta E = 0.12$.

Here, $\delta E_{\mathbf{k}}$ is given by small f - f hopping integrals. ($|\delta E_{\mathbf{k}}| < 0.12|t_{ss}|$) Here, we set $E_{1\mathbf{k}} \equiv E_1 + \delta E_{\mathbf{k}}$ and $E_{2\mathbf{k}} \equiv E_2 - \delta E_{\mathbf{k}}$, where the \mathbf{k} -dependence of $\delta E_{\mathbf{k}}$ is shown in Fig.43(a). Technically, to realize the $\delta E_{\mathbf{k}}$, we introduce the intra-orbital f - f hopping up to fifth nearest neighbor hopping integrals according to Ref.[36]. In Fig.43(b), we show the obtained f_l -orbital weight on Fermi surface. It shows strong \mathbf{k} -dependence irrespective of the fact that $|\delta E_{\mathbf{k}}|$ (~ 0.2) is much smaller than t_{sf} ($= 0.7$).

One may suspect that higher rank multipole susceptibilities may be suppressed when the f -orbital weight is \mathbf{k} -dependent, since the orbital off-diagonal components of χ^s may be suppressed. To answer this question, we perform RPA analysis by using PAM model with f - f hopping introduced in Eq.(4.69). Figure 43(c) shows the obtained magnetic multipole susceptibilities. We find that multiple higher-rank magnetic multipole susceptibilities develop, which is quite similar to our result without f - f hopping in Fig.34(b). This unexpected results originate from the fact that many body effects away from Fermi energy also contribute to the multipole susceptibility. This result strongly indicates that U -VC is still important even in the presence of small f - f hopping.

● key facts

- * 1 S-wave SC phase emerges in the presence of CEF splitting ΔE .
- * 2 Multi-orbital nature of Fermi surface is important to realize S-wave SC state. ($D^{f_1}(0) \approx D^{f_2}(0)$)
- * 3 Various magnetic multipole fluctuations develop even for finite f - f hopping.

4.10 Important roles of χ -VC

In the previous section, we neglect many-body effects to f -electron susceptibilities, which is naturally expected in strongly correlated system. This term is given by 3-vertex corrections beyond RPA, which we call χ -VC. Here, we consider the AL term for χ -VC, whose diagrammatic expression is shown in Fig.44.

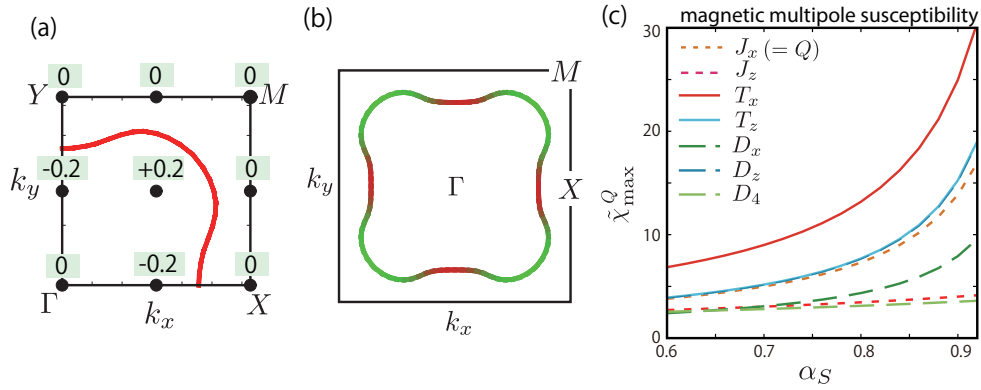


Figure 43: (a) Obtained Fermi surface with f - f hopping. Each number at \mathbf{k} shows intra-orbital energy shift $\delta E_{\mathbf{k}}$. (b) f_l -orbital weight on Fermi surface. The red (green) line corresponds to f_1 (f_2)-orbital. (c) α_S dependence of magnetic multipole susceptibilities, which are almost equal to those in Fig.34(b).

Then, the f -electron susceptibility is given as

$$\hat{\chi}_{\text{AL}}(q) = \hat{\phi}(q)(\hat{1} - u\hat{U}\hat{\phi}(q))^{-1}, \quad (4.70)$$

$$\hat{\phi}(q) \equiv \hat{\chi}^0(q) + \hat{X}^{\text{AL}}(q) \quad (4.71)$$

Since χ -VC is important only for electric (even-rank) multipole susceptibilities, we project out the magnetic channel contribution of χ -VC. We also drop the MT-type VC since its contribution is small. Schematic expression of AL-type χ -VC is given by

$$\hat{X}_{QQ'}^{\text{AL}} \propto \sum_{Q_1 \sim Q_4} \hat{V}^{Q_1, Q_2} \hat{V}^{Q_3, Q_4} (\hat{G}^f)^6 \vec{O}^Q \vec{O}^{Q' \dagger}, \quad (4.72)$$

where we drop the \mathbf{k} -dependence of the matrices. The detailed expression is written in Appendix A. From the symmetry of Green function $\hat{G}^f \propto \hat{\sigma}^0$ in Eq.(4.22), finite contribution comes from

$$\hat{X}_{QQ'}^{\text{AL}} \propto \text{Tr}\{O^Q \cdot O^{Q_1} \cdot O^{Q_4}\} \cdot \text{Tr}\{O^{Q'} \cdot O^{Q_2} \cdot O^{Q_3}\}. \quad (4.73)$$

In the following numerical study, we set $E_1 = E_2 = 0.1$ and $t_{sf}^1 = t_{sf}^2 = 0.62$ to make the analysis simple. Then, the relation $D_1(\epsilon) = D_2(\epsilon)$ holds. We adopt $T = 0.045$, $\mu = -0.143$, $n_f = 0.9$ and $n_s = 0.3$. In addition, we neglect el-ph coupling $g(\omega_j) = 0$. Here, we calculate f -electron susceptibilities in IR $\Gamma (= A_1^+, A_2^+, E^+, A_1^-, A_2^-, E^-)$ by solving the following equation;

$$\hat{\chi}_{\text{AL}}(\mathbf{q}, 0) \vec{w}_{\mathbf{q}}^{\Gamma} = \lambda_{\mathbf{q}}^{\Gamma} \vec{w}_{\mathbf{q}}^{\Gamma} \quad \left(\vec{w}_{\mathbf{q}}^{\Gamma} = \sum_{Q \in \Gamma} b_Q(\mathbf{q}) \vec{Q} \right) \quad (4.74)$$

where $\vec{w}_{\mathbf{q}}^{\Gamma}(\lambda_{\mathbf{q}}^{\Gamma})$ is the eigenvector (eigenvalue) and $b_Q(\mathbf{q})$ is real coefficient. Then, the largest eigenvalue gives the multipole susceptibility for Γ .

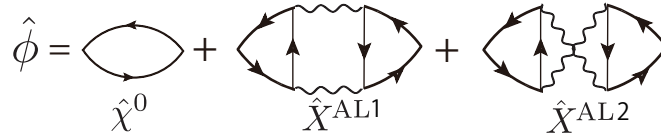


Figure 44: (a) Diagram of irreducible susceptibility with AL-VC.

In Fig.45 (a), we show obtained susceptibilities for each Γ . With increasing u , all the electric fluctuations strongly develop thanks to the AL-type χ -VC. Thus, large electric susceptibilities originate from the interference of magnetic fluctuations. For the electric susceptibilities, the maximum position for $\Gamma = A_1^+$

is $\mathbf{q} \approx (\pi, \pi)$, whereas A_2^+, E^+ has peak at $\mathbf{q} \approx (0, 0)$. For the magnetic susceptibilities, the maximum position for A_2^-, E^- is $\mathbf{q} \approx (\pi/2, \pi/2)$.

Next, we solve the linearized gap equation. In this calculation, we consider both χ -VC and U -VC. On the other hand, we neglect el-ph coupling to simplify the discussion. As explained in the previous section, U -VC for the electric channel is enhanced by various ranks of magnetic multipole fluctuations. Therefore, the pairing interaction due to electric fluctuations is strongly enlarged by U -VC. As shown in Fig.45 (b), $d_{x^2-y^2}$ -wave state is replaced with the s -wave at $u = 0.55$, since S -waves state is mediated by the strong electric fluctuations in Fig.45 (a). The obtained s -wave state is fully gapped without sign reversal, consistently with experiments in CeCu_2Si_2 .

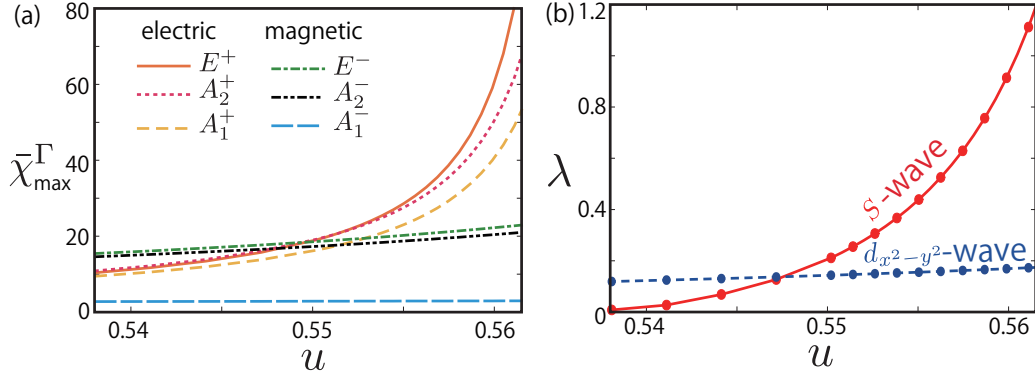


Figure 45: (a) Obtained susceptibility for each IR. Electric susceptibilities ($\Gamma = E^+, A_2^+, A_1^+$) develop due to the AL-VC.(b) Obtained eigenvalue as the function of Coulomb interaction u . The $d_{x^2-y^2}$ -wave state is replaced with the fully gapped s -wave state for $u > 0.55$.

● key facts

- * 1 Electric fluctuations in $\Gamma = E^+, A_2^+, A_1^+$ are enhanced by considering χ -VC.
- * 2 S -wave SC phase emerges near AFM phase even in the absence of el-ph coupling.

4.11 Microscopic origin of S -wave SC

Now, we discuss the origin of the s -wave superconductivity. First, we introduce the Q, Q' -fluctuation-induced pairing interaction in the band basis $V_{\text{sing}}^{\chi, QQ'}(k, k')$, which is given by the unitary formation of

$$\hat{V}_{\text{sing}}^{\chi, QQ'}(k, k') \equiv \left\{ u^2 \hat{\Lambda}_{k, k'}^{ch} \hat{U}^{ch} \hat{\chi}_{\text{AL}}^{ch, Q, Q'}(k - k') \hat{U}^{ch} \hat{\Lambda}_{-k, -k'}^{ch\dagger} \right\}_{\uparrow\uparrow\downarrow\downarrow} - \left\{ \right\}_{\uparrow\downarrow\uparrow\downarrow} \quad (4.75)$$

Then, SC pairing interaction due to the electric multipole fluctuations is given as,

$$V^{\chi, \text{ele}} = \sum_{QQ' \in \text{even}} V^{\chi, QQ'} \left(V^{\chi, QQ'} \equiv \int dk dp V_{\text{sing}}^{\chi, QQ'}(k, k') / \int dk dp \right) \quad (4.76)$$

Here, we introduce 2-types of model for further discussion;

$$\delta E_{\mathbf{k}} \neq 0 \rightarrow \text{Fig.43 (model A)} \quad \delta E_{\mathbf{k}} = 0 \quad (\text{model I}). \quad (4.77)$$

In model I, the orbital weight is perfectly isotropic, whereas the shape of Fermi surface is almost model-independent. In Fig.46 (a), we show obtained SC pairing interaction in the model A. The contribution from the hexadecapole (H_0) fluctuations in the A_1^+ representation is the largest, while other electric fluctuations are also important. In this case, S -wave SC appears with strong Coulomb interaction. For comparison, Fig.46 (b) show the result in the orbital isotropic model in the model I. Surprisingly, multipole fluctuations other than H_0 do not contribute to the s -wave pairing, irrespective that all electric

multipole susceptibilities (E^+ , A_2^+ , A_1^+) develop similarly to Fig.45 (a). In this case, S-wave SC doesn't appear. Then, obtained fact is summarized as;

model A \rightarrow S-wave SC emerges. model I \rightarrow Only D-wave SC emerges.

The reason of these non-trivial facts is explained in the next paragraph. The Fermi surface and its orbital character of each model are shown in Figs.46 (c) and (d).

In addition, we define the pairing interaction due to both electric and magnetic fluctuations (Coulomb repulsion) as

$$\begin{aligned}\hat{V}_{\text{sing}}^{\chi}(k, k') &\equiv \left\{ u^2 \hat{\Lambda}_{k, k'} \hat{U} \hat{\chi}_{\text{AL}}(k - k') \hat{U} \hat{\Lambda}_{-k, -k'}^{\dagger} \right\}_{\uparrow\uparrow\down\downarrow} - \left\{ \quad \quad \quad \right\}_{\uparrow\downarrow\uparrow\downarrow}, \\ \hat{V}_{\text{sing}}^U(k, k') &\equiv \left\{ u^2 \hat{\Lambda}_{k, k'} \hat{U} \hat{\Lambda}_{-k, -k'}^{\dagger} \right\}_{\uparrow\uparrow\down\downarrow} - \left\{ \quad \quad \quad \right\}_{\uparrow\downarrow\uparrow\downarrow}.\end{aligned}\quad (4.78)$$

Figure 47 shows the obtained interactions with lowest frequency ($\epsilon_n = \epsilon_m = \pi T$) averaged over the Fermi surface. Absolute value of $V_{\text{sing}}^{\chi(U)}$ increases with u due to U -VC for the electric channel. However, in model I, the total pairing interaction $V_{\text{sing}}^{\chi} + V_{\text{sing}}^U$ is always negative (=repulsive), so the d -wave state appears. In contrast, in model A, the total pairing interaction becomes positive with u since not only H_0 fluctuations, but also other electric fluctuations contribute to the attractive pairing when $\delta E_{\mathbf{k}} \neq 0$. Therefore, fully-gapped s -wave state is realized in model A for $u > 0.55$, as shown in Fig.45(b). For $u \sim 0.55$, the total pairing interaction is negative at $\epsilon_n = \epsilon_m = \pi T$ as shown in Fig.47(e). Nonetheless, the s -wave state is realized because of the retardation effect due to the strong frequency dependence of V^{sing} , as we explain in the Sec.4.12.

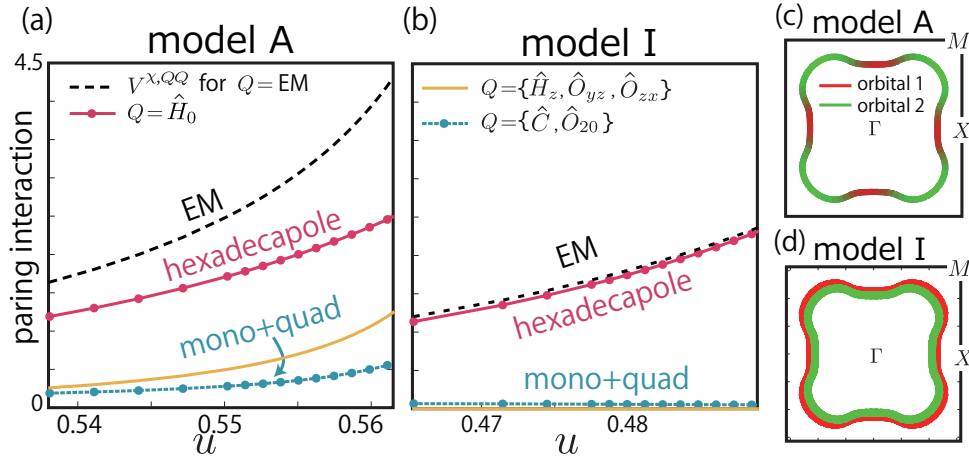


Figure 46: Obtained $V^{\chi, QQ}$ and $V^{\chi, EM}$ due to the EM fluctuations in (a) model A and (b) model I. (c),(d) Orbital character on the Fermi surface.

Finally, we discuss why all the electric fluctuations contribute to the S-wave state in model A, while only D-wave state appears in model I. In both model, electric and magnetic fluctuations are similar since $D_1(\epsilon) \approx D_2(\epsilon)$ holds even if $\delta E_{\mathbf{k}} \neq 0$. In this situation, one may expect that any electric fluctuations brings attractive pairing interaction. However, some elements of the electric susceptibility $\hat{\chi}^{QQ'}(\mathbf{q}, 0)$ can be negative except for monopole, so the cancellation of pairing interaction sometimes occur. (For example, $\chi_{1212}^{\text{sl}, QQ'}(\mathbf{q}) < 0$ for $Q = O_{yz, zx}$.) Therefore, difference between model A and I is that the ‘‘inter-orbital pairing’’ $\langle f_{\mathbf{k}1\uparrow} f_{-\mathbf{k}2\downarrow} \rangle$ is suppressed in model A due to the \mathbf{k} -dependence of the orbital character on the Fermi surface.

Now, we discuss origin of difference between model A and I. The pairing interaction is simplified as

$$\hat{V}^{\mu\nu} = g \vec{O}_{\mu\nu} (\vec{O}_{\mu\nu})^{\dagger}, \quad (4.79)$$

where $g > 0$ and $\hat{O}_{\mu\nu} \equiv \hat{\sigma}_{\mu} \hat{\tau}_{\nu}$ ($\mu, \nu = 0, x, y, z$). All the even rank operators are given by linear combination of $\hat{O}_{\mu\nu}$ with $(\mu\nu) = (00), (0x), (0z), (xy), (yy), (zy)$. The gap equation in the orbital basis is given

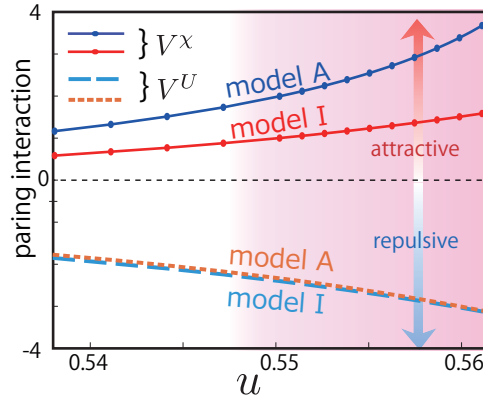


Figure 47: Obtained pairing interactions V^x and V^U . For model I, the horizontal axis is shifted by $+0.073$.

by

$$\lambda \hat{\Delta} \approx T \sum_k g {}^t\hat{O}_{\mu\nu} \hat{G}^f(k) \hat{\Delta} \hat{G}^f(-k) \hat{O}_{\mu\nu} \theta(\omega_c - |\epsilon_n|), \quad (4.80)$$

where ω_c is BCS type cut-off. As we mentioned before, \hat{G}^f is expressed as

$$G_{lm}^f(k) = G_l^{0f}(k) \delta_{lm} + (-1)^{l+m} t_{sf}^2 (\sin^2 k_y + \sin^2 k_x) G_l^{0f}(k) G_m^{0f}(k) G_{\uparrow}^c(k). \quad (4.81)$$

We neglect the first term in Eq. (4.81) since it does not give $-\ln T$ term in gap equation. In this case, we obtain

$$\hat{G} \propto \hat{\sigma}_0 (\hat{\tau}_0 - a \hat{\tau}_x) \quad (4.82)$$

In addition, $G_1^{0f}(k) = G_2^{0f}(k)$ holds in model I, while $G_1^{0f}(k) G_2^{0f}(k) = 0$ due to $|\delta E_{\mathbf{k}}| (\gg t_{sf}^2)$ in model A. Therefore, the symmetry of the Green function is approximately given as

$$a = 1 \quad (\text{model A}), \quad a = 0 \quad (\text{model I}). \quad (4.83)$$

Here, the general gap function is written by

$$\hat{\Delta} \propto i \hat{\sigma}_y (\Delta_0 \hat{\tau}_0 + \Delta_x \hat{\tau}_x). \quad (4.84)$$

By using the Eq.(4.82) and Eq.(4.84), we obtain

$$\hat{G} \hat{\Delta} \hat{G} \propto ((1 + a^2) \Delta_0 - 2a \Delta_x) i \hat{\sigma}_y \hat{\tau}_0 + ((1 + a^2) \Delta_x - 2a \Delta_0) i \hat{\sigma}_y \hat{\tau}_x. \quad (4.85)$$

Therefore, the eigenvalue of the gap equation is given by

$$\lambda = g'(1 + a)^2 \quad \text{for } (\mu\nu) = (00), (0x), \quad (4.86)$$

$$\lambda = g'(1 - a)^2 \quad \text{for } (\mu\nu) = (0z), (xy), (yy), (zy), \quad (4.87)$$

where $g' = g D_1(0) \ln(\omega_c/T)$.

In Fig.48, we summarize the eigenvalue λ for each electric pairing interaction, in the case of $a = 0$ (intra orbital Cooper pair) and $a = 1$ (intra+inter orbital Cooper pair). We note that $\hat{O}_{0z} \propto \hat{O}_{20} - 2\hat{C}$ and $\hat{O}_{0x} \propto -3\hat{H}_0 + 2\hat{O}_{20} + \hat{C}$. In case of $a = 0$, all electric fluctuations contribute to the pairing. In case of $a = 1$, however, only \hat{O}_{0x} and C channels contribute to the pairing. In the present PAM, charge (monopole) fluctuations are small, so they do not contribute to the pairing. Since \hat{O}_{0x} is included only in H_0 hexadecapole, the H_0 fluctuations give dominant s -wave pairing interaction. To summarize, the pairing interaction increases if the inter orbital Cooper pairs are killed by finite $|\delta E_{\mathbf{k}}|$, so the numerical results in Fig.47 are well understood.

We also analyzed more realistic PAM with $E_1^f > E_2^f$ and $t_{sf}^1 > t_{sf}^2$. Even in this case, we obtain H_0 hexadecapole fluctuation mediated fully-gapped s -wave state. Thus, our result discussed in this section will be robust.

model $\hat{P}_{\mu\nu}$	a=0 (intra orbital CP)	a=1 (inter+intra orbital CP)
$\hat{P}_{00} \propto \hat{C}$	g	4g
$\hat{P}_{0z} \propto \hat{O}_{20} - 2\hat{C}$	g	0
$\hat{P}_{0x} \propto 3\hat{H}_0 + 2\hat{O}_{20} + \hat{C}$	g	4g
$\hat{P}_{\mu y} \propto \hat{O}_{zx}, \hat{O}_{yz}, \hat{H}_z$	g	0

Figure 48: Eigenvalue λ due to $\hat{O}_{\mu\nu}$ electric interaction for $a = 0$ (intra orbital Cooper pair) and $a = 1$ (intra+inter orbital pair). Except for \hat{O}_{0x} and $\hat{C} = \hat{O}_{00}$, the electric fluctuations give repulsive interaction for inter-orbital Cooper pair.

● key facts

- * 1 S-wave SC state appears in model A, while only D-wave state appears in model I.
- * 2 Dominant attraction comes from the hexadecapole \hat{H}_0 fluctuation.
- * 3 Important fact for S-wave SC is that all electric fluctuations contribute to the pairing.

4.12 Retardation effect

Here, we discuss important roles of retardation effects. In Fig.49(a), we show the obtained pairing interaction on the Fermi surface defined as

$$V_{\max}^{\text{sing}}(\omega_j) \equiv \max_{\mathbf{k}, \mathbf{k}'} \{V^{\text{sing}}(\mathbf{k}, \pi T, \mathbf{k}', \pi T + \omega_j)\}. \quad (4.88)$$

The pairing interaction is attractive (positive) at $\omega_j = 0$, whereas it becomes to repulsion for $\omega_j > 0$. For this reason, the gap function defined as $\Delta(\epsilon_n) \equiv \max_{\mathbf{k}} \{\Delta(\mathbf{k}, \epsilon_n)\}$ shows the sign-change as the function of ϵ_n , as shown in the inset of Fig.49. This is a hallmark of the retardation effects due to the strong ω_j -dependence of the electric (even-rank) fluctuation. The similar result should be obtained when we consider the cut off energy given by el-ph interaction.

Due to the retardation effect, the direct Coulomb depairing potential is reduced from U to

$$U^* \sim \frac{U}{1 + UD(0)\ln(E_F/\omega_0)}, \quad (4.89)$$

where ω_0 is the energy scale of the electric fluctuations. Since $\omega_0 \ll E_F$, the fully-gapped s -wave superconductivity can be stabilized in HF systems.

To clarify the importance of the retardation effect, we calculate the gap equation for the following pairing interaction only at $|\epsilon_n| = |\epsilon_m| = \pi T$:

$$\tilde{V}^{\text{sing}}(\mathbf{k}, \mathbf{k}') \equiv V^{\text{sing}}(\mathbf{k}, \pi T, \mathbf{k}', \pi T). \quad (4.90)$$

Then, the reduction of the depairing potential ($U \rightarrow U^*$) is not taken into account.

Figure 49(b) shows the eigenvalue for the s -wave state “without retardation effect”, derived from Eq.(4.90). For comparison, we also plot the eigenvalues derived from the frequency-dependent $V^{\text{sing}}(k, k')$. The eigenvalue for the s -wave state derived from $\tilde{V}^{\text{sing}}(\mathbf{k}, \mathbf{k}')$ is smaller than that derived from $V^{\text{sing}}(k, k')$. Thus, the eigenvalue for the s -wave state is significantly enlarged by the reiteration effect ($U \rightarrow U^*$).

● key facts

- * 1 Retardation effect is important to explain S-wave SC phase.
- * 2 This effect comes from the energy dependence of electric fluctuations (or el-ph).

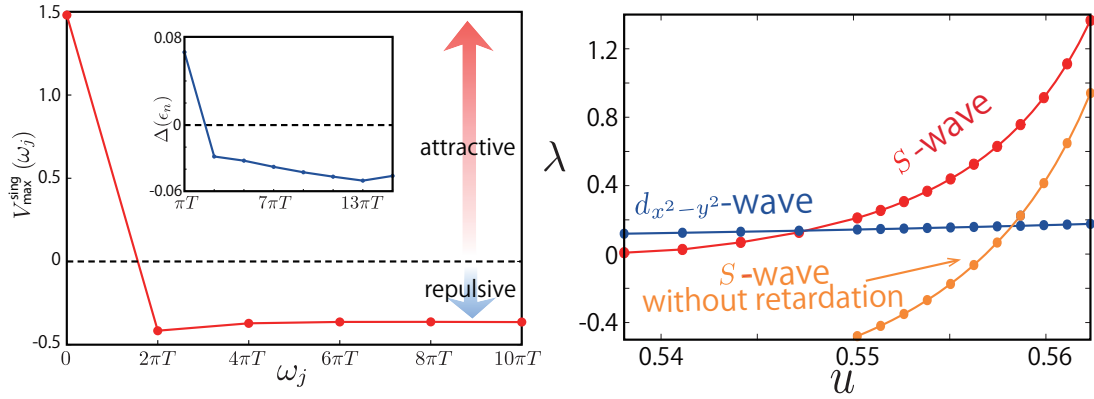


Figure 49: (a) Obtained pairing interaction $V_{\max}^{\text{sing}}(\omega_j)$ and gap function $\Delta(\epsilon_j)$ (inset) as the function of Matsubara frequency. Strong retardation effect is recognized. (b) Obtained eigenvalue as the function of u . The eigenvalue of the *s*-wave state is significantly enlarged by the retardation effect.

Conclusion

In this section, we proposed a microscopic origin of fully gapped *s*-wave superconductivity in multi-orbital HF systems based on beyond ME formalism. In the present $\Gamma_7^{(1)}-\Gamma_7^{(2)}$ quartet PAM, various magnetic multipole fluctuations develop, due to the cooperation between strong SOI and Coulomb interaction as shown in Fig.34. These fluctuations give significant U -VC in SC pairing interaction. Also, we verified that our present result does not change qualitatively compared with those for $\Delta E = 0 \sim 0.2$. In particular, attractive pairing interaction of electric ch is prominently enhanced by U -VC as plotted in Figs.39 and 40. As a result, even-rank multipole fluctuations bring attractive interaction when the system approaches to AFM-QCP. T_c of *s*-wave SC state is strongly enhanced near AFM-QCP in multi-orbital HF systems. In addition, it becomes easier to obtain *s*-wave SC phase when the moderate phonon-induced multipole fluctuations exist as shown in Fig.41. The present mechanism may be responsible for the fully gapped *s*-wave superconducting state realized in CeCu_2Si_2 .

Here, we comment that el-ph coupling is expected in HF systems. In fact, large Gruneisen parameter ($\eta \equiv -d\log T_K/d\log \Omega \sim 30 - 80$) was observed, which means el-ph interaction is significant [51]. Idea of phonon-mediated *s*-wave superconductivity in HF systems has been discussed in Refs.[51, 52, 53]. Now, this scenario becomes more realistic by considering U -VC founded in the Sec.4.

Another possible origin of electric fluctuations is many body effects due to AL-type χ -VC. By considering χ -VC, electric fluctuations drastically develop. After that, attractive SC pairing interaction is enhanced by large U -VC. Based on the present model, H_0 hexadecapole fluctuations dominate over other even-rank fluctuations as a attraction for SC Cooper pairs. Thus, *s*-wave state is caused by the hexadecapole (rank 4) fluctuations. Also, *s*-wave SC phase is stabilized by other electric fluctuations including quadrupole and monopole, when we introducing small δE_{kl} . In this case, the inter-orbital Cooper pairs are killed. Therefore, we revealed that all of χ -VC, U -VC and e -ph interaction enhance T_c of *s*-wave SC, cooperatively. The present pairing mechanism is expected to be important to understand various HF materials.

The main results of the present study are summarized as follows;

- (i) Near the magnetic QCP, several (higher-rank) multipole fluctuations strongly develop simultaneously, whereas dipole susceptibility solely develop in *d*-electron systems.
- (ii) Moderate electric multipole fluctuation develop due to cooperation of the el-ph coupling and many body effects beyond RPA (χ -VC)
- (iii) Development of magnetic multiple multipole fluctuations gives prominent U -VC, which leads to the violation of ME scheme.
- (iv) Owing to U -VC, electric-multipole fluctuations induced *s*-wave SC phase is stabilized when $D^{f1}(0) \approx D^{f2}(0)$. This is a necessary condition in realizing moderate quadrupole or hexadecapole susceptibility.

There remain unsolved future issues. For instance, renormalization of self-energy, which brings strong mass enhancement, is one of the important issue. Also, pressure-induced 2nd SC dome in CeCu_2Si_2 is uncovered problem [27]. In addition, we expect that the present mechanism may be applicable for TSC phase in UPt_3 .

References

- [1] T. Moriya and K. Ueda, Adv. Phys. **49**, 555 (2000).
- [2] Y. Yanase, T. Jujo, T. Nomura, H. Ikeda, T. Hotta, and K. Yamada, Physics Reports **387**, 1 (2003).
- [3] H. Kontani, Rep. Prog. Phys. **71**, 026501 (2008).
- [4] P. Monthoux, D. Pines, and G. G. Lonzarich, Nature **450**, 1177 (2007).
- [5] T. Dahm and L. Tewordt, Phys. Rev. B **52**, 1297 (1995).
- [6] P. Monthoux and D. J. Scalapino, Phys. Rev. Lett. **72**, 1874 (1994).
- [7] T. Takimoto, T. Hotta, and K. Ueda, J. Phys.: Condens. Matter, **15**, S2087 (2003).
- [8] R. Shiina, S. Shiba, and T. Peter, J. Phys. Soc. Jpn. **66**, 1741 (1997).
- [9] H. Kusunose and Y. Kuramoto, J. Phys. Soc. Jpn. **74**, 3139 (2005).
- [10] T. Takimoto, J. Phys. Soc. Jpn. **75**, 034714 (2006).
- [11] K. Haule and G. Kotliar, Nat. Phys. **5**, 796 (2009).
- [12] R. Okazaki, T. Shibauchi, H. J. Shi, Y. Haga, T. D. Matsuda, E. Yamamoto, Y. Onuki, H. Ikeda, and Y. Matsuda, Science **331**, 439 (2011).
- [13] H. Ikeda, M.-T. Suzuki, R. Arita, T. Takimoto, T. Shibauchi, and Y. Matsuda, Nat. Phys. **8**, 528 (2012).
- [14] K. Izawa, H. Yamaguchi, Y. Matsuda, H. Shishido, R. Settai, and Y. Onuki, Phys. Rev. Lett. **87**, 057002 (2001).
- [15] T. Onimaru, K. T. Matsumoto, Y. F. Inoue, K. Umeo, Y. Saiga, Y. Matsushita, R. Tamura, K. Nishimoto, I. Ishii, T. Suzuki, and T. Takabatake, J. Phys. Soc. Jpn. **79**, 033704 (2010).
- [16] A. Sakai and S. Nakatsuji, J. Phys. Soc. Jpn. **80**, 063701 (2011).
- [17] F. Steglich, J. Aarts, C. D. Bredl, W. Lieke, D. Meschede, W. Franz, and H. Schafer, Phys. Rev. Lett. **43**, 1892 (1979).
- [18] H. Q. Yuan, F. M. Grosche, M. Deppe, C. Geibel, G. Sparn, and F. Steglich, Science **302**, 21042107 (2003).
- [19] C. Peiderer, Rev. Mod. Phys. **81**, 1551 (2009).
- [20] K. Ishida, Y. Kawasaki, K. Tabuchi, K. Kashima, Y. Kitaoka, K. Asayama, C. Geibel, F. Steglich, Phys. Rev. Lett. **82**, 5353 (1999).
- [21] S. Kittaka, Y. Aoki, Y. Shimura, T. Sakakibara, S. Seiro, C. Geibel, F. Steglich, H. Ikeda, and K. Machida, Phys. Rev. Lett. **112**, 067002 (2014).
- [22] S. Kittaka, Y. Aoki, Y. Shimura, T. Sakakibara, S. Seiro, C. Geibel, F. Steglich, Y. Tsutsumi, H. Ikeda, K. Machida, Phys. Rev. B **94**, 054514 (2016).
- [23] T. Yamashita, T. Takenaka, Y. Tokiwa, J. A. Wilcox, Y. Mizukami, D. Terazawa, Y. Kasahara, S. Kittaka, T. Sakakibara, M. Konczykowski, S. Seiro, H. S. Jeevan, C. Geibel, C. Putzke, T. Onishi, H. Ikeda, A. Carrington, T. Shibauchi, and Y. Matsuda, Sci. Adv. **3**, e1601667 (2017).
- [24] G. Pang, M. Smidman, J. Zhang, L. Jiao, Z. Weng, E. M. Nica, Y. Chen, W. Jiang, Y. Zhang, W. Xie, H. S. Jeevan, H. Lee, P. Gegenwart, F. Steglich, Q. Si, and H. Yuan, Proc Natl Acad Sci USA **115**, 5343 (2018).
- [25] L. V. Pourovskii, P. Hansmann, M. Ferrero, and A. Georges, Phys. Rev. Lett. **112**, 106407 (2014).
- In the present model, we introduce t_{sf} between the nearest Ce sites in the (001) plane. Then, the relation $|V_{\mathbf{k}f_1\sigma}| \approx 2|V_{\mathbf{k}f_2\sigma}|$ holds according to Slater-Koster tight-binding method [40]. In contrast, Pourovskii [25] consider the hybridization between Ce site at $\vec{r} = 0$ and the nearest neighbor Si sites at $(\pm 1/2, \pm 1/2, \pm c)$, and then the relation $|V_{\mathbf{k}f_2\sigma}| \approx 2|V_{\mathbf{k}f_1\sigma}|$ holds. In both cases, electric multipole fluctuation mediated superconductivity proposed in this paper is realized when $D^{f_1}(0) \simeq D^{f_2}(0)$ at finite ΔE .
- [26] K. Hattori, J. Phys. Soc. Jpn. **79**, 114717 (2010).
- [27] A. T. Holmes, D. Jaccard, and K. Miyake, Phys. Rev. B **69**, 024508 (2004).
- [28] H. Ikeda, M.-T. Suzuki, and R. Arita, Phys. Rev. Lett. **114**, 147003 (2015).
- [29] S. Onari and H. Kontani, Phys. Rev. Lett. **109**, 137001 (2012).
- [30] S. Onari, Y. Yamakawa, and H. Kontani, Phys. Rev. Lett. **116**, 227001 (2016).
- [31] Y. Yamakawa, S. Onari, and H. Kontani, Phys. Rev. X **6**, 021032 (2016).
- [32] J. R. Schrieffer, J. Low Temp. Phys. **99**, 314 (1995).
- [33] M. H. Sharifzadeh Amin and P. C. E. Stamp, Phys. Rev. Lett. **77**, 3017 (1996).
- [34] A. B. Migdal, J. Exptl. Theoret. Phys. **34**, 1438 (1958).
- [35] R. Tazai, Y. Yamakawa, M. Tsuchiizu and H. Kontani, J. Phys. Soc. Jpn. **86**, 073703 (2017).
- [36] Y. Yamakawa, and H. Kontani, Phys. Rev. B **96**, 144509 (2017).
- [37] A. Georges, G. Kotliar, W. Krauth, and M. J. Rozenberg, Rev. Mod. Phys. **68**, 13 (1996).

- [38] G. Kotliar and D. Vollhardt, *Physics today* **57**, 53 (2004).
- [39] K. Held, *Adv. Phys.* **56**, 829 (2007).
- [40] J. H. Shim, K. Haule, and G. Kotliar, *Science* **318**, 1615 (2007).
- [41] J. Otsuki, *Phys. Rev. Lett.* **115**, 036404 (2015).
- [42] K. Takegahara, Y. Aoki, and A. Yanase, *J. Phys. C* **13**, 583 (1980).
- [43] T. Saso and H. Harima, *J. Phys. Soc. Jpn.* **72**, 1131 (2003).
- [44] A. Amorese, N. Caroca-Canales, S. Seiro, C. Krellner, G. Ghiringhelli, N. B. Brookes, D.V. Vyalikh, C. Geibel, and K. Kummer, Arxiv:1803.11068.
- [45] R. Tazai and H. Kontani, unpublished.
- [46] J. C. Slater, *Phys. Rev.* **34**, 1293 (1929).
- [47] M. R. Norman, *Phys. Rev. B* **52**, 1421 (1995).
- [48] T. Inui, Y. Tanabe, and Y. Onodera, Springer, Berlin (1993).
- [49] H. Kontani and S. Onari, *Phys. Rev. Lett.* **104**, 157001 (2010).
- [50] T. Saito, Y. Yamakawa, S. Onari, and H. Kontani, *Phys. Rev. B* **92**, 134522 (2015).
- [51] H. Razafimandimby, P. Fulde, and J. Keller, *Z. Phys. B* **54**, 111 (1984).
- [52] F. J. Ohkawa, *J. Phys. Soc. Jpn.* **56**, 713 (1987).
- [53] K. Miyake, T. Matsuura, H. Jichu, and Y. Nagaoka, *Prog. Theor. Phys.* **72**, 713 (1984).
- [54] R. Tazai, Y. Yamakawa, M. Tsuchiizu, H. Kontani, *Phys. Rev. B* **94**, 115155 (2016).
- [55] M. Tsuchiizu, Y. Yamakawa, S. Onari, Y. Ohno, and H. Kontani, *Phys. Rev. B* **91**, 155103 (2015).

5 Multipole phase

Introduction

In HF systems, there are very interesting phenomena originating from exotic electronic states with strong Coulomb interaction and SOI in f -electrons. In particular, it is well known that AFM fluctuations cause interesting quantum transition and SC phase [1]-[8]. In the case of HF system, various multipole order and fluctuations appear, which is absent in transition metal oxides. One of the typical multipole ordered system is CeB₆. It shows AF-quadrupole order with $\mathbf{q} = (\pi, \pi, \pi)$ around $T_Q = 3.2\text{K}$. Then, magnetic dipole order appears at $T_N = 2.4\text{K}$ [9]-[12]. Moreover, AF-octupole order is induced in small magnetic field [13]-[16]. Therefore, it is expected that various multipole fluctuations appear simultaneously in the $H - T$ phase diagram of CeB₆.

Until now, CeB₆ has been studied intensively based on localized f -electron picture [13]-[19]. However, recent ARPES and neutron inelastic scattering for CeB₆, as well as dHvA for Ce _{x} La _{$1-x$} B₆, uncovered the itinerant nature of the f -electron system above $T \sim T_Q$ [20]-[25]. These findings mean that itinerant property becomes a reasonable starting point to study the multipole physics of CeB₆. In this section, we approach to the long standing problem by considering χ -VC.

If we perform RPA study on the PAM, quadrupole order will not be obtained. In particular, odd-rank (=magnetic) multipole fluctuations emerge, while even-rank (=electric) ones remain small within RPA [24, 26, 27]. This fact originates from the importance of VC, due to the many body effects omitted in RPA. For a long time, Fermi Liquid approach has been succeeded in HF materials, such as CeB₆ [24], URu₂Si₂ [26], and CeCu₂Si₂ [27]. In this case, large Coulomb interaction is renormalized into zU . In many HF systems, $z \ll 1$ is satisfied. Therefore, Fermi liquid theory is applicable even if Coulomb repulsion is quite large.

In the previous study, the lowest-ordered VC with respect to fluctuations, called MT-terms has been studied. Due to the MT-term, rank-5 multipole ordered state is stabilized in URu₂Si₂ [26]. On the other hand, the MT-VC did not affect even-rank multipole fluctuations. Thus, microscopic origin of quadrupole order observed in various compounds remains important issue. For this purpose, CeB₆ is a suitable to reveal a theoretical origin of multipole order in HF systems.

Recently, it has been revealed that AL-VC becomes more important than MT-VC, AL-VC works a trigger for realizing nematic order in Fe-based superconductors [28, 29, 30]. Analytically, AL-VC is related to the magnetic correlation length ξ as ξ^{4-d} in d -dimension systems. Thus, AL-VC plays significant roles near the AFM-QCP, which is verified by fRG study in Sec.2 with higher-order VC in an unbiased way. [31]-[37]. In the previous section (Sec4), we revealed the important role of VC in f -electron system [38, 27]. This fact indicates significance of AL-VC in multipole HF systems, which has not been studied so far.

In this section (Sec.5), we study the microscopic origin of quadrupole order in CeB₆ by using the itinerant f -electron PAM. Here, we introduce effective model composed of Γ_8 quartet f -electrons. Both uniform and AF-octupole fluctuations appear originating from the p-h nesting. It is consistent with neutron experiments. Therefore, AF-quadrupole (O_{xy}) order is stabilized by the interference among different types of magnetic multipole fluctuations. The present proposed theory with AL-VC is expected to be applicable for various HF compounds.

Model

5.1 Γ_8 PAM & multipole symmetry

Here, we introduce 2D PAM for describing CeB₆. For f -electron states, we consider the Γ_8 quartet in $J = 5/2$ space due to the strong SOI [13]:

$$\begin{aligned} |f_1 \downarrow (\uparrow)\rangle &= \sqrt{\frac{5}{6}} | + (-) \frac{5}{2} \rangle + \sqrt{\frac{1}{6}} | - (+) \frac{3}{2} \rangle, \\ |f_2 \downarrow (\uparrow)\rangle &= | + (-) \frac{1}{2} \rangle, \end{aligned} \quad (5.1)$$

where \downarrow (\uparrow) is the pseudo-spin up (down). The kinetic term is given by

$$\hat{H}_0 = \sum_{\mathbf{k}\Sigma} \epsilon_{\mathbf{k}} c_{\mathbf{k}\Sigma}^\dagger c_{\mathbf{k}\Sigma} + \sum_{\mathbf{k}l\sigma} E f_{\mathbf{k}l\sigma}^\dagger f_{\mathbf{k}l\sigma} + \sum_{\mathbf{k}l\sigma\Sigma} \left(V_{\mathbf{k}l\Sigma\sigma}^* f_{\mathbf{k}l\sigma}^\dagger c_{\mathbf{k}\Sigma} + \text{h.c.} \right), \quad (5.2)$$

where $c_{\mathbf{k}\sigma}^\dagger$ is a creation operator for s -electron with momentum \mathbf{k} and spin σ on Ce ion. $\epsilon_{\mathbf{k}}$ is the conduction band dispersion, which we explain in the Appendix F. $f_{\mathbf{k}l\Sigma}^\dagger$ is a creation operator for f -electron with \mathbf{k} , orbital l , pseudo-spin σ and energy E . $V_{\mathbf{k}l\Sigma\sigma}$ is the s - f hybridization term between the nearest Ce sites. Using the Slater-Koster method [40], $V_{\mathbf{k}l\Sigma\sigma}$ is given as

$$V_{\mathbf{k}l\Sigma\sigma} = -\sigma t_{sf}^l (\sin k_y + (-1)^l \sigma i \sin k_x) \delta_{\sigma,\Sigma}, \quad (5.3)$$

where the pseudo-spin is conserved ($\sigma = \Sigma$) in the present 2D model. Detailed explanation of $V_{\mathbf{k}l\Sigma\sigma}$ is written in Appendix F. Hereafter, we set $2|t_{ss}^1| = 1$ as energy unit, and put $t_{sf}^l = \sqrt{18/14} \times (0.78)$, $E = -2.0$, $T = 0.01$, and $\mu = -2.45$. Then, f (s)-electron number is $n_f = 0.58$ ($n_s = 0.69$). We comment that n_f increases if we put the level of E_l lower under the condition $n_f + n_c = \text{const.}$ By this procedure, our main results will not change since the shape of the Fermi surface is essentially unchanged.

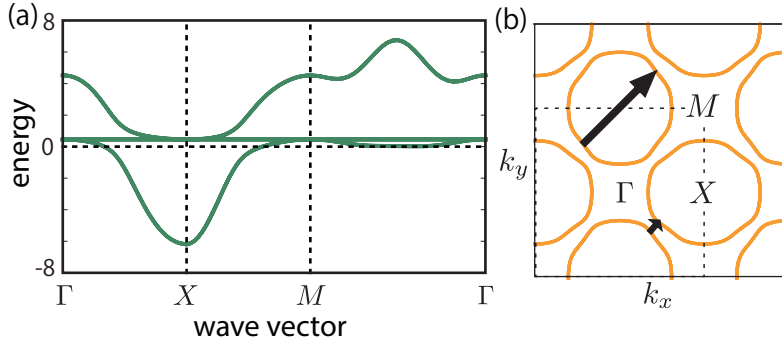


Figure 50: (a) Band dispersion and (b) Fermi surfaces of the present model. Black vector represents major nesting vectors.

Figure 50(a) shows the band structure of the present PAM. The lowest band crosses the Fermi level ($\epsilon = 0$). Since $W_D \sim 5\text{eV}$ in CeB_6 [20, 21, 41, 42], $2|t_{ss}^1| (= 1)$ corresponds to $\sim 0.5\text{eV}$. The bandwidth of itinerant f -electron is $W_D^{qp} \sim |V_{\mathbf{k}l\Sigma\sigma}| \sim 1$. The Fermi surfaces shown in Fig.30(b) are composed of large ellipsoid electron pockets around X,Y points, consistently with recent ARPES studies [20, 21]. We also consider the Coulomb interaction introduced in Eq.(4.5) in Sec.4. The maximum element of \hat{U} is set to unity.

In Γ_8 quartet model, there are 16-type active multipole operators up to rank 3; monopole, dipole (rank 1), quadrupole (rank 2), octupole (rank 3) momenta. The table of irreducible representation (IR) in the D_{4h} point group is shown in TABLE 4. Even rank (odd rank) operators correspond to electric (magnetic) multipole operators.

Here, we define the Coulomb interaction in the multipole basis, which is given by

$$U^{Q,Q'} = (\vec{Q})^\dagger \hat{U} \vec{Q}'. \quad (5.4)$$

Here, \vec{Q} is 16×1 vector TABLE 5 shows the diagonal component $U^Q \equiv U^{Q,Q}$. Electric channels of the Coulomb interaction are much smaller than that for the magnetic channels. Therefore, quadrupole phase can't be explained by the symmetry of Coulomb interaction. The inner product $(\vec{Q})^\dagger \vec{Q}'$ is unity for $Q = Q'$. It is zero when Q and Q' belong to different IR, whereas it is not always zero when $Q \neq Q'$ belong to the same IR [27, 39].

The Green function $\hat{G}^c, \hat{G}^f, \hat{G}^{cf}$ is defined in the same way as Eq.(4.17)~(4.18) in Sec.4. In the present model, $V_{\mathbf{k}l\sigma\sigma}^* V_{\mathbf{k}m\sigma\sigma}$ in the f -electron Green function \hat{G}^f is given by,

$$V_{\mathbf{k}l\sigma\sigma}^* V_{\mathbf{k}m\sigma\sigma} = t_{sf}^l t_{sf}^m (\sin^2 k_y + (-1)^{l+m} \sin^2 k_x + 2(l-m)\sigma i \sin k_x), \quad (5.5)$$

Therefore, the symmetry of the Green function is given by

$$\hat{G}^f \propto \hat{\sigma}^0 (\hat{\tau}^0 + a \hat{\tau}^x) + b \hat{\sigma}^z \hat{\tau}^y \quad (5.6)$$

IR(Γ)	rank(k)	multipole(\hat{Q})	matrix(\hat{O}^Q)	IR in H_z
Γ_1^+	0	$\hat{1}$	$\hat{\sigma}^0 \hat{\tau}^0$	Γ_1
	2	\hat{O}_{20}	$4\hat{\sigma}^0 \hat{\tau}^z$	
Γ_3^+	2	\hat{O}_{22}	$4\hat{\sigma}^0 \hat{\tau}^x$	Γ_3
Γ_4^+	2	\hat{O}_{xy}	$-\hat{\sigma}^z \hat{\tau}^y$	Γ_4
Γ_5^+	2	$\hat{O}_{yz(zx)}$	$-\hat{\sigma}^{x(y)} \hat{\tau}^y$	Γ_5
Γ_2^-	1	\hat{J}_z	$\hat{\sigma}^z (-1.2\hat{\tau}^0 - 0.67\hat{\tau}^z)$	Γ_1
	3	$\hat{T}_{z\alpha}$	$\hat{\sigma}^z (-\hat{\tau}^0 - 7\hat{\tau}^z)$	
Γ_3^-	3	\hat{T}_{xyz}	$-10\hat{\sigma}^0 \hat{\tau}^y$	Γ_4
Γ_4^-	3	$\hat{T}_{z\beta}$	$-6.7\hat{\sigma}^z \hat{\tau}^x$	Γ_3
Γ_5^-	1	$\hat{J}_{x(y)}$	$\hat{\sigma}^{x(y)} (1.2\hat{\tau}^0 - 0.34\hat{\tau}^z + (-)0.58\hat{\tau}^x)$	Γ_5
	3	$\hat{T}_{x\alpha(y\alpha)}$	$\hat{\sigma}^{x(y)} (\hat{\tau}^0 - (+)3.5\hat{\tau}^z + 6.1\hat{\tau}^x)$	
	3	$\hat{T}_{x\beta(y\beta)}$	$\hat{\sigma}^{x(y)} (-5.8\hat{\tau}^z - (+)3.4\hat{\tau}^x)$	

Table 4: IRs and 16-type active multipole operators of D_{4h} point group. Operator with rank k corresponds to 2^k -pole.

Q	1	$O_{20(22)}$	$O_{xy(yz,zx)}$	T_{xyz}	$J_{z(x,y)}$	$T_{z(x,y)}^\alpha$	$T_{z(x,y)}^\beta$
U^Q	-2.4	0.50	0.63	0.81	1.03	0.94	0.94

Table 5: Normalized Coulomb interaction U^Q . The relation $U^{Q,Q'} = 0$ holds for $Q \neq Q'$ except for $U^{J_\mu, T_\mu^\alpha} = 0.58$ where $\mu = x, y, z$.

The f -electron Green function has spin dependence,

$$\begin{aligned} G_{ll'}^f(k) &\equiv G_{ll'}^f(k) = G_{ll'}^f(k) \quad (G_{lm\uparrow}^f(k) \neq G_{lm\downarrow}^f(k)), \\ G^c(k) &\equiv G_\uparrow^c(k) = G_\downarrow^c(k), \end{aligned} \quad (5.7)$$

which means that the spin index can't be excluded unlike

● key facts

- * 1 We consider 2D Γ_8 quartet PAM in the presence of strong SOI.
- * 2 We can not obtain O_{xy} quadrupole phase by RPA since electric ch of bare Coulomb interaction is much smaller than magnetic ch ones.
- * 3 f -electron Green function has spin dependence; $\hat{G}^f \propto \hat{\sigma}^0 (\hat{\tau}^0 + a\hat{\tau}^x) + b\hat{\sigma}^z \hat{\tau}^y$.

Method & Result

5.2 Magnetic multipole susceptibility

Γ_7 model in Sec.4. The bare irreducible susceptibility is given by

$$\chi_{\alpha,\beta}^0(q) = -T \sum_k G_{LM}^f(k+q) G_{M'L'}^f(k), \quad (5.8)$$

where $L \equiv (l, \sigma)$ and $\alpha \equiv (L, L')$. α, β takes $1 \sim 16$, and \hat{G}^f Here we use the Green function without self-energy. Then, f -electron susceptibility within RPA is given as

$$\hat{\chi}(q) = \hat{\chi}^0(q) (\hat{1} - u\hat{U}\hat{\chi}^0(q))^{-1}, \quad (5.9)$$

Here, we consider the following eigen equation

$$u\hat{U}\hat{\chi}^0(\mathbf{q}, 0)\vec{w}^\Gamma(\mathbf{q}) = \alpha^\Gamma(\mathbf{q})\vec{w}^\Gamma(\mathbf{q}), \quad (\vec{w}^\Gamma(\mathbf{q}) = \sum_{Q \in \Gamma} Z^Q(\mathbf{q})\vec{Q}) \quad (5.10)$$

where $Z^Q(\mathbf{q})$ is a real coefficient. The maximum of the eigenvalue $\alpha^\Gamma(\mathbf{q})$ gives the Stoner factor for IR Γ ,

$$\alpha^\Gamma = \max_{\mathbf{q}}\{\alpha^\Gamma(\mathbf{q})\}, \quad / \quad \alpha^{\text{mag}(\text{el})} = \max_n\{\alpha^{\Gamma_n^{-(+)}}\}, \quad (n = 1, 3, 5) \quad (5.11)$$

where $\alpha^{\text{mag}(\text{el})}$ is the magnetic (electric) Stoner factor. The Γ -channel multipole order appears when $\alpha^\Gamma \geq 1$. Using \vec{Q} , the multipole susceptibility is given by

$$\chi^{Q,Q'}(q) = (\vec{Q})^\dagger \hat{\chi}(q) \vec{Q}'. \quad (5.12)$$

First, we show the numerical results by RPA. Figure 51 shows obtained susceptibilities $\chi^Q(\mathbf{q}, 0) \equiv \chi^{Q,Q}(\mathbf{q}, 0)$ at $u = 1.08$ ($\alpha^{\text{mag}} = 0.9$). In RPA, χ^{J_z} is the most largest. Secondly, $\chi^{T_x^\beta}, \chi^{T_x^\alpha}$ ($\nu = x, y$) and $\chi^{T_{xyz}}$ are also enlarged. $\chi^{J_z}(\mathbf{q}, 0)$ has peak value at $\mathbf{q} \approx \mathbf{0}$ and $\mathbf{q} \approx \mathbf{Q} \equiv (\pi, \pi)$, which is consistent with the inelastic neutron-scattering that reports strong ferromagnetic and antiferromagnetic fluctuations at $\mathbf{q} = (\pi, \pi, \pi), (\pi, \pi, 0)$ above T_N [23, 43]. Therefore, the present two-dimensional PAM is reliable. On the other hand, RPA quadrupole susceptibility remains small.

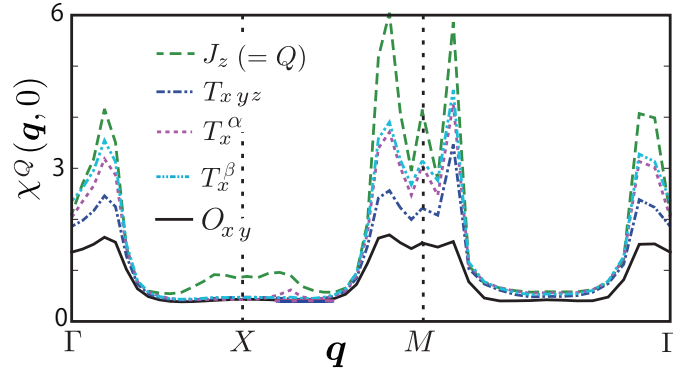


Figure 51: Obtained multipole susceptibilities by RPA. The peak positions correspond to the nesting vectors in Fig. 50 (b).

● key facts

- * 1 Various magnetic fluctuations develop within RPA.
- * 2 Obtained magnetic susceptibilities has peak at $\mathbf{q} \approx \mathbf{0}$ and $\mathbf{q} \approx \mathbf{Q} \equiv (\pi, \pi)$.

5.3 Electric multipole susceptibility

From now on, we introduce the VC due to AL and MT terms.

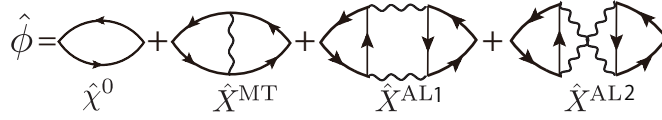
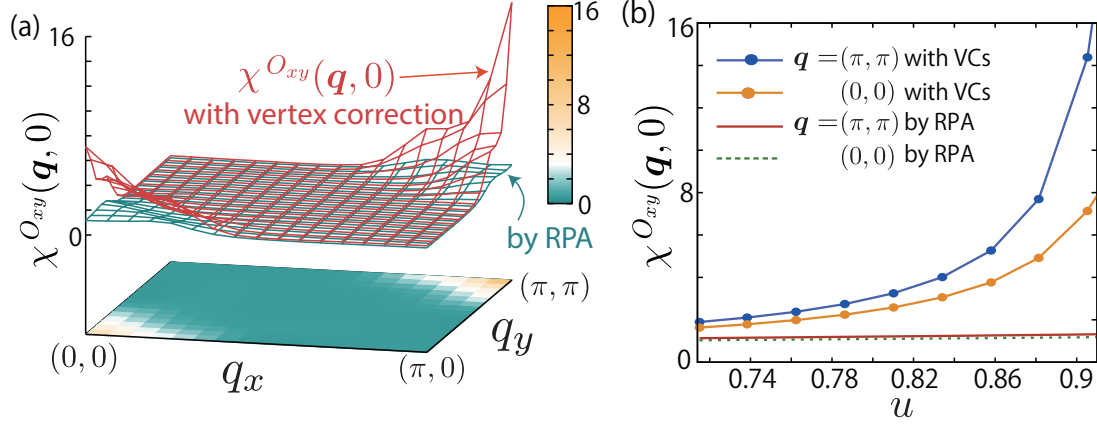
$$\hat{\chi}(q) = \hat{\phi}(q)(\hat{1} - u\hat{U}\hat{\phi}(q))^{-1}, \quad (\hat{\phi}(q) \equiv \hat{\chi}^0(q) + \hat{X}^{\text{AL+MT}}(q)) \quad (5.13)$$

where $\hat{\phi}(q)$ is irreducible susceptibility including the VC in the 16×16 matrix form. Diagrams of these VC are shown in Fig.52. For example, the expression for the MT term is

$$X_{LL'MM'}^{MT}(q) = T^2 \sum_{p,k,A \sim D} G_{LA}(k+q-p)G_{BL'}(k-p)G_{DM}(k+q)G_{M'C}(k)V_{DACB}(p). \quad (5.14)$$

where $p \equiv (\mathbf{p}, \omega_m)$, and $\hat{V}(q) \equiv u^2\hat{U}\hat{\chi}(q)\hat{U} + u\hat{U}$ is the dressed interaction given by RPA.

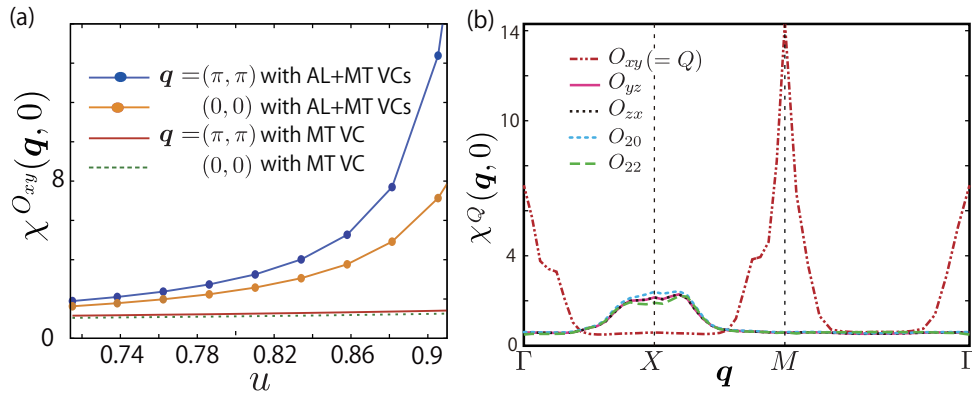
Figures 53 (a) and (b) show the obtained quadrupole susceptibility including MT- and AL-VC. In contrast to RPA result, the obtained $\chi^{O_{xy}}(\mathbf{q}, 0)$ is strongly enhanced at $\mathbf{q} = \mathbf{Q}$ and $\mathbf{q} = \mathbf{0}$, and becomes the largest of all χ^Q . This enhancement originates from the AL terms, whereas the MT term is very small as we show in 54. We find that $\chi_{\text{AL}}^{O_{xy}}(\mathbf{q}, 0)$ strongly increases with u . In contrast, $\chi_{\text{MT}}^{O_{xy}}(\mathbf{q}, 0)$ remains small and comparable to RPA result in Fig. 3 (c). Therefore, it is verified that the enhancement of O_{xy} quadrupole fluctuations originates from the AL-VC, whereas the MT-VC is very small.

Figure 52: Diagrams of the irreducible susceptibility $\hat{\phi}$ with MT- and AL-VC.Figure 53: (a) \mathbf{q} -dependence of $\chi^{O_{xy}}(\mathbf{q}, 0)$ at $\alpha^{\Gamma_4^+} = 0.94$ with AL-VC+MT-VC. (b) u -dependence of $\chi^{O_{xy}}(\mathbf{q}, 0)$ at $\mathbf{q} = \mathbf{Q}$ and $\mathbf{q} = \mathbf{0}$.

The obtained $\chi^{O_{xy}}(\mathbf{q}, 0)$ has the highest peak at $\mathbf{q} = \mathbf{Q}$, consistently with the antiferro- O_{xy} order in CeB₆. Moreover, the second highest peak of $\chi^{O_{xy}}(\mathbf{q}, 0)$ at $\mathbf{q} = \mathbf{0}$ explains the softening of shear modulus C_{44} in CeB₆ [10].

In Fig.54, we show all quadrupole susceptibilities including $O_{xy}, O_{zx}, O_{yz}, O_{20}, O_{22}$. In the present 2D model, only O_{xy} -fluctuation strongly develops. The reason is that (T_x, T_y) fluctuations are much larger than T_z fluctuations in RPA due to the violation of cubic symmetry. Since $O_{\mu\nu}$ quadrupole susceptibility is magnified by (T_μ, T_ν) fluctuations ($\mu, \nu = x, y, z$) due to the AL-VC, $\chi^{O_{xy}}(\mathbf{q}, 0)$ is larger than that for O_{zx}, O_{yz} in the present 2D model. In contrast, in the cubic model, $\chi^Q(\mathbf{q}, 0)$ with $Q = O_{xy}, O_{zx}, O_{yz}$ should equally develop.

In addition, as we show in TABLE 5, the Coulomb interaction U^Q for $Q = O_{xy/yz/zx}$ is much larger than that for $Q = O_{20/22}$. For this reason, it is difficult to expect that $Q = O_{20/22}$ quadrupole susceptibility becomes larger than $Q = O_{xy}$ one, even if the AL-VC are considered. Thus, the relation $\chi^{O_{xy}}(\mathbf{q}, 0) > \chi^{O_{20/22}}(\mathbf{q}, 0)$ should hold even in cubic systems. To summarize, the obtained strong enhancements of $\chi^{O_{xy}}(\mathbf{q}, 0)$ and $\chi^{J_z}(\mathbf{q}, 0)$ at both $\mathbf{q} = \mathbf{Q}$ and $\mathbf{q} = \mathbf{0}$ reproduce the key experimental results

Figure 54: (a) Obtained $\chi_{AL}^{O_{xy}}(\mathbf{q}, 0)$ with AL1+AL2 terms and $\chi_{MT}^{O_{xy}}(\mathbf{q}, 0)$ with MT term at $\mathbf{q} = \mathbf{Q}, \mathbf{0}$ as function of u . (b) Obtained quadrupole susceptibilities $\chi^Q(\mathbf{q}, 0)$ for $Q = O_{xy}, O_{zx/yz}$, and $O_{20/22}$.

of CeB₆.

● key facts

- * 1 $\chi^{O_{xy}}(\mathbf{q}, 0)$ develops by considering AL- and MT-terms at both $\mathbf{q} = \mathbf{Q}$ and $\mathbf{q} = \mathbf{0}$
- * 2 AL-term brings dominant contribution to the enhancement of $\chi^{O_{xy}}$
- * 3 $\chi^{O_{yz(zx)}}$ should equally develop if we consider 3D nature of CeB₆.

Discussion

5.4 Microscopic origin of quadrupole phase

Next, we explain that the O_{xy} quadrupole order is derived from the interference between magnetic multipole fluctuations. For this purpose, we analyze the total AL term for O_{xy} -channel defined as

$$X_{O_{xy}}^{\text{AL}}(q) \equiv (\vec{O}_{xy})^\dagger \hat{X}^{\text{AL}}(q) \vec{O}_{xy}, \quad (5.15)$$

The Stoner factor for $\chi^{O_{xy}}$ channel is proportional to $uU^{O_{xy}}\phi^{O_{xy}}(q)$, where $\phi^{O_{xy}}(q) \equiv (\vec{O}_{xy})^\dagger \hat{\phi}(q) \vec{O}_{xy}$. Therefore, $X_{O_{xy}}^{\text{AL}}(q) (> 0)$ works as enhancement factor of O_{xy} susceptibility. For instance, the AL1 term due to (Q, Q') -channel fluctuations is defined as

$$X_{O_{xy}}^{\text{AL1}, QQ'}(q) \equiv \frac{T}{2} \sum_p V^Q(p) V^{Q'}(p-q) \Lambda_{q,p}^{O_{xy} QQ'} (\Lambda_{\bar{q}, \bar{p}}^{O_{xy} Q'Q})^*, \quad (5.16)$$

where $V^Q(q)$ and $\Lambda_{q,p}^{O_{xy} QQ'}$ are defined as

$$\hat{V}(q) = \sum_Q V^Q(q) \vec{Q}(\vec{Q})^\dagger, \quad (5.17)$$

$$\Lambda_{q,p}^{O_{xy} QQ'} \equiv \sum_\alpha (\vec{O}_{xy})_\alpha^* (\vec{Q}')^\dagger \hat{\Lambda}^\alpha(q, p) \vec{Q}. \quad (5.18)$$

The diagrammatic expression of Eq.(5.16) is shown in Fig.55(a). Figure 55(b) shows the \mathbf{q} -dependence of $X_{O_{xy}}^{QQ'}(\mathbf{q}, 0)$ at $u = 0.91$. We find that the $(Q, Q') = (T_x^\alpha, T_y^\alpha), (J_z, T_{xyz}), (T_x^\beta, T_y^\beta)$ channels give the dominant contributions. Other terms not shown in Fig.55(b) give negligible contribution. Therefore, we conclude that O_{xy} quadrupole fluctuation is enhanced by various types of magnetic fluctuations.

Next, we discuss the \mathbf{q} -dependence of the AL-VC, which is given as

$$X_{O_{xy}}^{\text{AL}, T_x T_y}(\mathbf{q}) \propto \sum_p \chi^{T_x}(\mathbf{p}) \chi^{T_y}(\mathbf{q} - \mathbf{p}). \quad (5.19)$$

It becomes large at $\mathbf{q} = \mathbf{Q}$ and $\mathbf{q} = \mathbf{0}$ since $\chi^{T_\mu}(\mathbf{p})$ has large peaks at $\mathbf{p} \sim \mathbf{Q}, \mathbf{0}$ shown in Fig.51. Thus, antiferro-quadrupole order in CeB₆ originates from the interference between ferro- and antiferro-magnetic multipole fluctuations.

Figure 55(c) presents the quantum process of \hat{O}_{xy} quadrupole order driven by the interference between (T_x, T_y) fluctuations, which corresponds to $\Lambda^{O_{zz} T_x T_y}$ in Fig.55(a). This process is realized when

$$\Lambda^{O_{zz} QQ'} \propto \text{Tr}\{\hat{O}_{xy} \cdot \hat{Q} \cdot \hat{Q}'\} \neq 0. \quad (5.20)$$

In contrast, since $\Lambda^{QT_x T_y} \propto \text{Tr}\{\hat{Q} \cdot \hat{T}_x \cdot \hat{T}_y\} = 0$ for odd-rank Q , the AL-VC is negligible for $Q = J, T$.

● key facts

- * 1 Microscopic origin of $\chi^{O_{xy}}$ is interference between 2-types of magnetic fluctuations, mainly from T_x and T_y fluctuations.
- * 3 The peak structure of $\chi^{O_{xy}}(\mathbf{q})$ originates from large $\chi^{T_x, T_y}(\mathbf{p})$ at $\mathbf{p} \sim \mathbf{Q}, \mathbf{0}$.

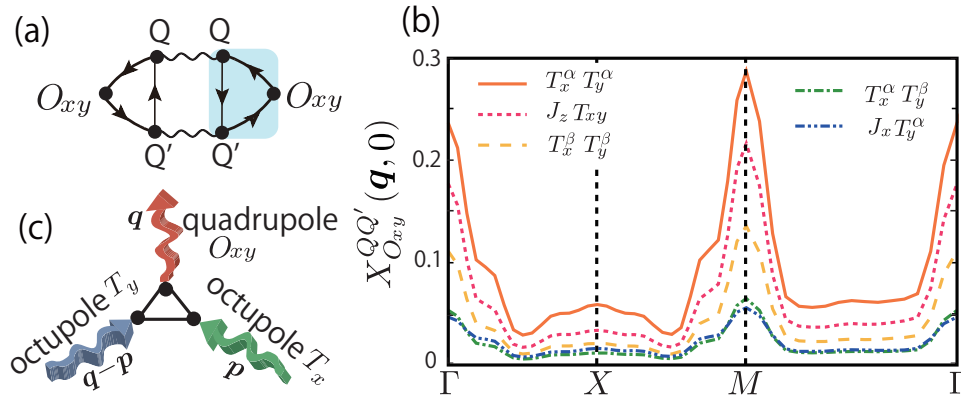


Figure 55: (a) AL-term $X_{O_{xy}}^{AL1,QQ'}$ given by (Q, Q') -channel fluctuations. (b) Obtained $X_{O_{xy}}^{QQ'}(\mathbf{q}, 0)$ along high-symmetry line. (c) Quantum process of O_{xy} fluctuations driven by the interference between (T_x, T_y) fluctuations, which corresponds to the shaded area in (a). Note that $\chi^{O_{xy}} \neq \chi^{O_{xz(yz)}}$ in the present 2D model

5.5 Magnetic field

Finally, we discuss the field-induced octupole order, which has been studied intensively as a main issue of CeB₆ [13, 14, 15, 16]. The Zeeman term under the magnetic field along z -axis is given as

$$\hat{H}_Z = h_z \sum_{L,M} (\hat{J}_z)_{L,M} f_{\mathbf{k}L}^\dagger f_{\mathbf{k}M}. \quad (5.21)$$

In the presence of magnetic field $h_z \neq 0$, electric and magnetic multipole belongs to the same IR as shown in the 5th column in TABLE4.[13] In this case, both O_{xy} and T_{xyz} belong to the same IR Γ_4 . Therefore, inter-multipole susceptibility $\chi^{O_{xy}, T_{xyz}}(\mathbf{q}, 0)$ is induced in proportion to h_z , since

$$\text{Tr}\{\hat{O}_{xy} \cdot \hat{J}_z \cdot \hat{T}_{xyz}\} \neq 0. \quad (5.22)$$

In Fig.56(a), we show the diagrammatic expression of quadrupole-octupole susceptibility in the presence of magnetic field. To verify this, we solve the eigen equation (5.10) for the IR Γ_4 under h_z , at the fixed magnetic Stoner factor in RPA at $\alpha^{\text{mag}} = 0.8$ [44, 45].

Figures 56(b) shows the obtained coefficient of eigenvector \vec{w}^{Γ_4} , which is defined as

$$\vec{w}^{\Gamma_4}(\mathbf{q}) = Z^{O_{xy}}(\mathbf{q})\vec{O}_{xy} + Z^{T_{xyz}}(\mathbf{q})\vec{T}_{xyz} \quad (|\vec{w}^{\Gamma_4}|^2 = 1). \quad (5.23)$$

$Z^{T_{xyz}}$ increases linearly in h_z , due to the interference process under h_z shown in the Fig. 56(a). $Z^{T_{xyz}}$ becomes comparable to $Z^{O_{xy}}$ under small magnetic field $h_z \lesssim 0.03 \ll W_D^{qp}/10$.

Figures 56(c) shows the largest stoner factor α^{Γ_4} at $\mathbf{q} = \mathbf{Q}$ as functions of h_z . The increment of α^{Γ_4} under h_z is consistent with the field-enhancement of T_Q in CeB₆. (In contrast, T_N will be suppressed by large O_{xz} moment.) Since the ratio of the ordered momenta at T_Q is $M^{T_{xyz}}/M^{O_{xy}} = Z^{T_{xyz}}/Z^{O_{xy}}$, field-induced antiferro T_{xyz} order is naturally explained. In Fig.56(d) we show the proposed mechanism of field-induced $O_{xy} + T_{xyz} \in \Gamma_4$ order.

● key facts

- * 1 Antiferro T_{xyz} phase is induced by magnetic field along z -axis since $\chi^{O_{xy}, T_{xyz}} \neq 0$.
- * 2 T_{xyz} order is strongly magnified by large $\chi^{O_{xy}, T_{xyz}}$, which comes from AL-type χ -VC.
- * 3 Origin of T_{xyz} phase is interference of multipole fluctuations.

Conclusion

In summary, we proposed multipole fluctuation mechanism to explain the quadrupole ordering in CeB₆ by considering AL-VC in HF systems. As a result, both ferro- and antiferro-magnetic multipole

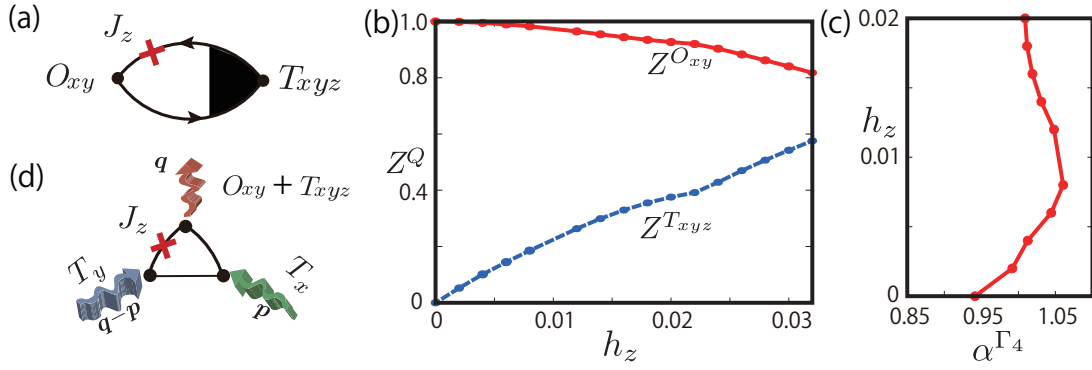


Figure 56: (a) Form factor ($Z^{O_{xy}}, Z^{T_{xyz}}$) of the eigenvector for $\Gamma_4 = \{O_{xy}, T_{xyz}\}$ at $\mathbf{q} = \mathbf{Q}$ under h_z . Inset: h_z -linear term of the three-point vertex $\Lambda^{T_{xyz}T_xT_y}$ that gives large $\chi^{O_{xy}T_{xyz}}(\mathbf{q}, 0)$. (b) Stoner factor α^{Γ_4} as function of h_z .

fluctuations are induced around nesting vector of the Fermi surface. It is consistent with recent neutron experiments. In particular, we showed that AF- O_{xy} order at T_Q ($> T_N$) originates from the interference among the different types of magnetic multipole fluctuations, which are enlarged within RPA as shown in Fig.55(c). Also, we verified that magnetic field occurs octupole ordered phase identified in CeB₆. The inter-multipole coupling mechanism will be important even in other HF systems [46, 47] as well as 4d, 5d transition metal system [48]. Therefore, it is an important future problem to analyze AL-VC in 3D system.

At the starting point of the present study, we showed that on-site quadrupole (O_{xy}) interaction is about 60% of dipole (J_μ) one as listed in TABLE 5. For this reason, quadrupole ordered phase cannot appear within RPA scheme. In contrast, by using RKKY model, quadrupole interaction gets as large as the dipole one. [13, 16, 49]. Therefore, the difference between itinerant and localized scheme may enable us to notice some important facts.

Finally, the main results of the present study are summarized as follows;

- (i) Near the AFM-QCP, several multipole fluctuations strongly develop, simultaneously including higher-rank (octupole T) fluctuations.
- (ii) Development of magnetic multiple multipole fluctuations gives large χ -VC for electric ch fluctuations, which cause violation of RPA.
- (iii) Owing to χ -VC, AF-quadrupole fluctuation $\chi^{O_{xy}}(\mathbf{q})$ at $\mathbf{q} = (\pi, \pi)$ develop due to the interference between magnetic octupole fluctuations given by T_x and T_y at $\mathbf{p} \sim \mathbf{Q}, \mathbf{0}$.
- (iv) Antiferro T_{xyz} phase is induced by small magnetic field along z -axis due to the χ -VC and inter-multipole fluctuation $\chi^{O_{xy}, T_{xyz}}$.

References

- [1] P. Coleman, *Handbook of Magnetism and Advanced Magnetic Materials*, Vol 1, 95-148 (Wiley, 2007).
- [2] T. Moriya and K. Ueda, *Adv. Phys.* **49**, 555 (2000).
- [3] Y. Yanase, T. Jujo, T. Nomura, H. Ikeda, T. Hotta, and K. Yamada, *Physics Reports* **387**, 1 (2003).
- [4] H. Kontani, *Rep. Prog. Phys.* **71**, 026501 (2008).
- [5] P. Monthoux, D. Pines, and G. G. Lonzarich, *Nature* **450**, 1177 (2007).
- [6] D. Senechal and A.-M.S. Tremblay, *Phys. Rev. Lett.* **92**, 126401 (2004).
- [7] P. Monthoux and D. J. Scalapino, *Phys. Rev. Lett.* **72**, 1874 (1994).
- [8] T. Takimoto, T. Hotta, and K. Ueda, *J. Phys.: Condens. Matter*, **15**, S2087 (2003).
- [9] T.Fujita, M.Suzuki, T.Komatsubara, S.Kunii, T.Kasuya and T.Ohtsuka, *Solid State Commun.* **35**, 569 (1980).
- [10] S. Nakamura, T. Goto, S. Kunii, K. Iwashita and A. Tamaki, *J. Phys. Soc. Jpn.* **63**, 623 (1994).
- [11] M.Hiroi, S.Kobayashi, M.Sera, N.Kobayashi and S.Kunii, *J. Phys. Soc. Jpn.* **66**, 132 (1997).
- [12] A. S. Cameron, G. Friemel, and D. S. Inosov, *Rep. Prog. Phys.* **79**, 066502 (2016).
- [13] R. Shiina, S. Shiba, and P. Thalmeier, *J. Phys. Soc. Jpn.* **66**, 1741 (1997).
- [14] O. Sakai, R. Shiina, H. Shiba, and P. Thalmeier, *J. Phys. Soc. Jpn.* **66**, 3005 (1997); O. Sakai, R. Shiina, H. Shiba, and P. Thalmeier, *J. Phys. Soc. Jpn.* **68**, 1364 (1999).
- [15] P. Thalmeier, R. Shiina, H. Shiba, and O. Sakai, *J. Phys. Soc. Jpn.* **67**, 2363 (1998).
- [16] H. Shiba, O. Sakai, and R. Shiina, *J. Phys. Soc. Jpn.* **68**, 1988 (1999).
- [17] M. Sera and S. Kobayashi, *J. Phys. Soc. Jpn.* **68**, 1664 (1999).
- [18] H. Kusunose and Y. Kuramoto, *J. Phys. Soc. Jpn.* **74**, 3139 (2005).
- [19] K. Hanzawa, *J. Phys. Soc. Jpn.* **70**, 468 (2001).
- [20] M. Neupane, N. Alidoust, I. Belopolski, G. Bian, S.-Y. Xu, D.-J. Kim, P. P. Shibayev, D. S. Sanchez, H. Zheng, T.-R. Chang, H.-T. Jeng, P. S. Riseborough, H. Lin, A. Bansil, T. Durakiewicz, Z. Fisk, and M. Z. Hasan *Phys. Rev. B* **92**, 104420 (2015).
- [21] A. Koitzsch, N. Heming, M. Knupfer, B. Buchner, P.Y. Portnichenko, A.V. Dukhnenko, N.Y. Shitsevalova, V.B. Filipov, L.L. Lev, V.N. Strocov, J. Ollivier, and D.S. Inosov, *Nat. Commun.* **7**, 10876 (2016).
- [22] G. Friemel, Yuan Li, A. V. Dukhnenko, N. Yu. Shitsevalova, N. E. Sluchanko, A. Ivanov, V. B. Filipov, B. Keimer, and D. S. Inosov, *Nat. Commun.* **3**, 830 (2012).
- [23] H. Jang, G. Friemel, J. Ollivier, A. V. Dukhnenko, N. Yu. Shitsevalova, V. B. Filipov, B. Keimer, and D. S. Inosov, *Nat. Mater.* **13**, 682 (2014).
- [24] A. Akbari and P. Thalmeier, *Phys. Rev. Lett.* **108**, 146403 (2012).
- [25] M. Endo, S. Nakamura, T. Isshiki, N. Kimura, T. Nojima, H. Aoki, H. Harima, and S. Kunii, *J. Phys. Soc. Jpn.* **75**, 114704 (2006).
- [26] H. Ikeda, M.-T. Suzuki, R. Arita, T. Takimoto, T. Shibauchi, and Y. Matsuda, *Nat. Phys.* **8**, 528 (2012).
- [27] R. Tazai and H. Kontani, *Phys. Rev. B* **98**, 205107 (2018).
- [28] S. Onari and H. Kontani, *Phys. Rev. Lett.* **109**, 137001 (2012).
- [29] S. Onari, Y. Yamakawa, and H. Kontani, *Phys. Rev. Lett.* **116**, 227001 (2016).
- [30] Y. Yamakawa, S. Onari, and H. Kontani, *Phys. Rev. X* **6**, 021032 (2016).
- [31] M. Tsuchiizu, Y. Ohno, S. Onari and H. Kontani *Phys. Rev. Lett.* **111**, 057003 (2013).
- [32] M. Tsuchiizu, Y. Yamakawa, S. Onari, Y. Ohno, and H. Kontani, *Phys. Rev. B* **91**, 155103 (2015).
- [33] M. Tsuchiizu, Y. Yamakawa, and H. Kontani, *Phys. Rev. B* **93**, 155148 (2016).
- [34] R. Tazai, Y. Yamakawa, M. Tsuchiizu, and H. Kontani, *Phys. Rev. B* **94**, 115155 (2016).
- [35] M. Tsuchiizu, K. Kawaguchi, Y. Yamakawa, and H. Kontani, *Phys. Rev. B* **97**, 165131 (2018).
- [36] R.-Q. Xing, L. Classen, and Andrey V. Chubukov, *Phys. Rev. B* **98**, 041108 (2018).
- [37] U. Karahasanovic, F. Kretschmar, T. Bohm, R. Hackl, I. Paul, Y. Gallais, and J. Schmalian, *Phys. Rev. B* **92**, 075134 (2015).
- [38] R. Tazai, Y. Yamakawa, M. Tsuchiizu, and H. Kontani, *J. Phys. Soc. Jpn.* **86**, 073703 (2017).
- [39] Supplemental Material.
- [40] K. Takegahara, Y. Aoki, and A. Yanase, *J. Phys. C* **13**, 583 (1980).
- [41] Y. Kubo and S. Asano, *Phys. Rev. B* **39**, 8822 (1989).
- [42] A. Hasegawa and A. Yanase, *Journal of Physics F, Metal Physics*, **7**, 7 (1977).
- [43] At $T \sim T_Q$, $\chi^{J\mu}(\mathbf{q}, \omega)$ at $\mathbf{q} = \mathbf{Q}, \mathbf{0}$ is much larger than that at the magnetic order wavevector $\mathbf{Q}_N = (\pi/2, \pi/2, 0)$ below T_N according to Ref. [23].

-
- [44] We adjust u to keep α^{mag} constant, since α^{mag} decreases with h_z for fixed u in RPA. In the FLEX approximation, α^{mag} increases with h_z due to the negative feedback effect between spin fluctuations and self-energy [45].
- [45] K. Sakurazawa, H. Kontani, and T. Saso, *J. Phys. Soc. Jpn.* **74**, 271 (2005).
- [46] T. Takimoto and P. Thalmeier, *Phys. Rev. B* **77**, 045105 (2008).
- [47] K. Kubo and T. Hotta, *Phys. Rev. B* **71**, 140404(R) (2005).
- [48] S. Hayami, Y. Yanagi, H. Kusunose, and Y. Motome *Phys. Rev. Lett.* **122**, 147602 (2019).
- [49] T. Yamada and K. Hanzawa, *J. Phys. Soc. Jpn.* **88**, 084703 (2019).

6 Summary

In the present paper, we studied microscopic origin of SC and multipole phase in SCES in a unified way considering many body effects beyond RPA+ME theory. Until recently, it was widely believed that the basic properties of SC states in SCES is qualitatively well understood within conventional RPA+ME theory. However, recent experiments revealed that RPA+ME theory fails in several SCES, such as Fe-based and HF superconductor. Thus, new microscopic theory is required to solve the problem. Here, we focused on significant roles of VC due to many body effects. It was revealed that violation of RPA+ME theory occur especially in multiorbital and multipole systems. As we have shown in this paper, VC is classified into χ -VC and U -VC;

- VC for p-h irreducible susceptibility (χ -VC), which is absent in RPA.
- VC for SC paring interaction (U -VC), which is neglected in the ME.

We conclude that VC is necessary to understand fundamental properties of various phenomena observed in SCES. Our main findings based on the beyond RPA+ME theory are listed as follows;

Summary 1: Both U -VC and χ -VC work as a mode coupling between different type of p-h fluctuations, as we verified by using the fRG and perturbation theory.

Summary 2: Mode coupling effects drastically change the ground state. For instance, orbital ordered state is induced by interference between different magnetic fluctuations near AFM QCP.

Summary 3: U -VC strongly enhances the attractive SC paring interaction due to the electric or orbital channel fluctuations.

Summary 4: AFM fluctuations and el-ph interaction can work cooperatively on s-wave SC paring mechanism against common knowledge. This result originates from the fact that phonon-mediated attraction is enhanced by U -VC near AFM QCP.

Summary 5: Mode coupling becomes more significant in f -electrons system than d -electrons due to large number of multipole degrees of freedom. Higher-rank electric ch multipole fluctuations stabilize s-wave SC in CeCu₂Si₂.

Summary 6: Interference between 2-types of octupole fluctuations induce quadrupole phase in CeB₆.

We believe that our findings are meaningful step for revealing essential roles of many body effects behind various long standing problems in SCES. Also, a lot of interesting issues are left in the field of SCES. One of that is non trivial transport phenomena, such as non-Fermi-liquid behavior, are reported near the SC and multipole phase. In addition, external field induced phases were also discovered. Therefore, we need to continue our work to solve these issues in the future. Hereafter, we review each section (Sec.2~5) in more detail.

Functional Renormalization Group (fRG) study

In Sec.2, we studied 2-orbital (d_{xz}, d_{yz}) Hubbard model without SOI based on fRG+cRPA theory. The fRG study has great merit for understanding fundamental properties of many body effect since parquet type higher-order processes are automatically generated in unbiased way. In fRG+cRPA study, we consider 3 energy region with lower cut off energy ω_c and boundary of fRG and cRPA Λ_0 . Hereafter, we set $\Lambda_0 \ll \epsilon_F$. In the highest energy region ($\Lambda_0 < \xi_k$), p-h instability within RPA process is the most dominant. In this case, only spin fluctuations develop while orbital ones remain small. On the other hand, in the lower energy region ($\omega_c < \xi_k < \Lambda_0$), AL-type VC for p-h fluctuation becomes significant and orbital fluctuations develop due to the χ -VC. In the lowest energy region ($\xi_k < \omega_c$), p-p instability dominates over p-h one. Then, U -VC for SC paring interaction plays significant roles in forming Cooper pairs. As a result, we revealed that TSC phase appears near the boundary of orbital and magnetic ordered phase. Therefore, microscopic origin of TSC phase comes from cooperation between spin and orbital fluctuations due to the VC beyond RPA+ME theory. In addition, we compared the result of fRG study with that of diagrammatic calculation. Then, we conclude that the dominant contribution comes from AL-type U -VC, which brings mode coupling between spin and orbital degrees of freedom.

Cooperation of el-ph and AFM fluctuations for SC state

In Sec.3, we studied 2-orbital Hubbard Holstein model in the presence of B_{1g} el-ph interaction. We revealed that small el-ph coupling g strongly enhances the quadrupole orbital fluctuations due to the significant roles of AL-type χ -VC. In addition, fully gapped s-wave SC phase emerges near magnetic QCP even in the presence of the small g . The required value of g get smaller as the system approaches to AFM-QCP. Large attractive paring interaction appeared due to the orbital fluctuation U -VC. For this reason, we conclude that microscopic origin of s-wave SC state is the cooperation between AFM fluctuation and el-ph interaction, which is neglected in conventional RPA+ME theory. We stress that U -VC is enlarged only neat the Fermi surface. Therefore, local approximation fails to explain large U -VC. We note that retardation effects due to the cut off energy of el-ph interaction is also important to understand the obtained phase diagram.

S-wave superconductivity in CeCu_2Si_2

In Sec.4, we studied 2-orbital PAM motivated by recent progress in experimental study on CeCu_2Si_2 , which revealed that s-wave SC phase appears irrespective of the fact that the system is near AFM phase. To understand the experimental fact, we focus on many body effects due to χ -VC and U -VC as well as strong SOI in f -electron system. In the presence of strong SOI, various higher-rank order parameters get to be active. Therefore, higher-rank multipole fluctuations induce nontrivial phase transition. Considering multipole fluctuations, we study SC paring mechanism. First, we showed that various magnetic channel fluctuations develop within RPA theory. And also, electric fluctuations are induced by the magnetic fluctuations due to the χ -VC or A_{1g} el-ph interaction. As a result, s-wave SC phase appears near AFM-QCP. The microscopic origin of s-wave SC state is the large attractive paring interaction due to the electric channel multipole fluctuations. We found that the attraction is drastically enhanced by magnetic channel fluctuations through the U -VC. In addition, we found that multi-orbital nature of Fermi surface plays important roles in the proposed mechanism. Especially, $D^{f_1}(0) \approx D^{f_2}(0)$ is needed. We also showed that various type of electric multipole fluctuation including quardupole and hexadecapole fluctuations works as a attraction for SC paring. In summary, we proposed SC paring mechanism in HF CeCu_2Si_2 considering many body effects beyond conventional RPA+ME theory. Essentially, violation of conventional ME theory brought us a new SC pairing mechanism, which is "interference among the different rank of multipole fluctuations".

Multipole phase

In Sec.5, we studied 2D Γ_8 quartet PAM to understand the origin of hidden ordered phase in CeB_6 . First, we performed RPA, and showed that various magnetic multipole fluctuations develop. However, magnetic multipole fluctuations cannot explain the experimental facts which revealed that the elastic constant jumps at transition temperature of hidden ordered phase. Therefore, we go beyond RPA by considering χ -VC for multipole susceptibilities. As a result, we reveled that electric quadrupole O_{xy} fluctuations is induced by the interference between 2-types of magnetic octupole T_x, T_y fluctuations. In particular, AF-octupole and ferro octupole fluctuaions induced AF quadrupole phase. Then, we proposed octupole fluctuation mediated quadrupole (O_{xy}) phase in CeB_6 . Finally, we introduced magnetic field along z-axis and showed that octupole T_{xyz} order is induced by the magnetic field.

Acknowledgements

I would like to express sincere gratitude to my supervisor, Prof. Hiroshi Kontani. I learned a lot from him through my graduate education for 5 years. He told me how to study physics, write a paper and give a presentation. In addition, his motto, which is "Do what you want to do since our life time is limited", guided me whenever I was going to lost my way. Without his sincere support, it would not be possible to publish this PhD thesis.

Besides my supervisor, I'd like to thank all (related) members of Sc laboratory (Dr. Onari, Dr. Kobayashi, Dr. Tsuchiizu, Dr. Yamakawa and colleagues). Their interesting discussion with sophisticated knowledge really inspired me. We have been through a lot together including cooking and having lunch and dinner in 'S-collo'. Every day in the laboratory was fulfilling for me. I also appreciate sincere support from Prof. Johan, who motivated me to continue to study physics. In addition, I thank every my friends who live in Toyoyama town and other prefecture as well as other countries.

My sincere thanks also go to everybody who supported my study in every situation. Their kind advices improved my research. I enjoyed valuable events and meeting held in society of physics, especially in condensed matter physics. My PhD study has been supported by leading program in Green Natural Science in Nagoya university and KAKENHI (No.18J12852) from the Japan Society for the Promotion of Science (JSPS).

Finally, I would like to express my deepest thanks to my family (my parents, young sister and my dog) for supporting my life for a long time.

7 Appendix

Appendix A: fRG theory and expression for VC

Here, we discuss on momentum conservation in fRG study. In the Sec.1, 4-point vertex function $\Gamma_{k_1 k_2 k_3 k_4}$ is analyzed by using fRG+cRPA. In the present patch method, we consider patch (p) conservation given by

$$p_1 + p_4 \simeq p_2 + p_3 \quad (7.1)$$

Compared with previous fRG method, we adopt wider condition for the momentum conservation. For instance, if we put p_1 and p_2 on the red arrow as shown in Fig.57, p_3 and p_4 were set in the yellow colored area in the previous method. Thus, only inter-band scatterings are considered. On the other hand, we include p_3 and p_4 in the pink colored area on the black dotted allows, This improvement enable us to consider low energy scattering more accurately in solving RG equation.

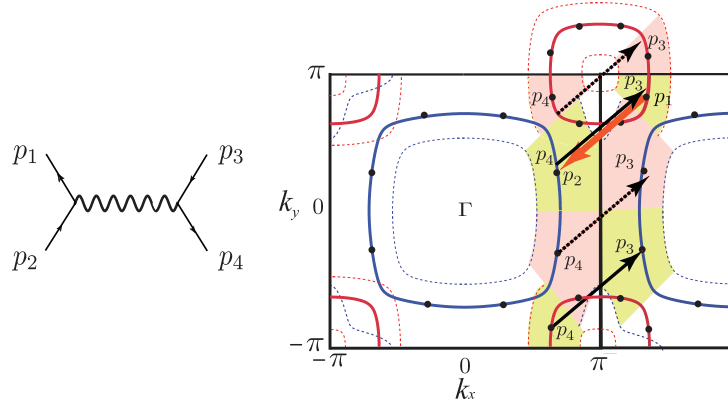


Figure 57: In the present fRG method, both pink and yellow colored area are taken into account as the position of patch p_3 and p_4 .

Here, we explain analytical expression for the AL- and MT-terms in U -VC. First, 4-point vertex function in the orbital basis due to RPA susceptibility is define as

$$\hat{I}^{c(s)}(q) = \hat{U}^{c(s)}(\hat{\chi}_{\text{RPA}}^{c(s)}(q) + \{\hat{U}^{c(s)}\}^{-1})\hat{U}^{c(s)}. \quad (7.2)$$

By using the 4-point vertex, dressed Coulomb interaction due to the MT-type VC is given by

$$U_{ll'mm'}^{c,\text{MT}}(k, k') = \frac{T}{2} \sum_{q, a \sim d} U_{lmbc}^c \{I_{amdm'}^c(q) + 3I_{amdm'}^s(q)\} G_{ab}(k+q) G_{cd}(k'+q), \quad (7.3)$$

$$U_{ll'mm'}^{s,\text{MT}}(k, k') = \frac{T}{2} \sum_{q, a \sim d} U_{lmbc}^s \{I_{amdm'}^c(q) - I_{amdm'}^s(q)\} G_{ab}(k+q) G_{cd}(k'+q), \quad (7.4)$$

where $a \sim h$ and l, l', m, m' are orbital indices. The diagrammatic expression for the MT term is shown in the 2nd term of the rhs in Fig.14(b). Also, the AL-type VC is defined by

$$\begin{aligned} U_{ll'mm'}^{c,\text{AL}}(k, k') &= \frac{T}{2} \sum_{q, a \sim h} U_{lmf}^c \{ \Lambda_{abcdef}(k'', q) + \Lambda_{fcbada}(k'', -q - k'') \} \\ &\quad \times \{ I_{bcmg}^c(q + k'') I_{m'hed}^c(q) + 3I_{bcmg}^s(q + k'') I_{m'hed}^s(q) \} G_{gh}(k' - q), \\ U_{ll'mm'}^{s,\text{AL}}(k, k') &= \frac{T}{2} \sum_{q, a \sim h} U_{lmf}^s \{ \Lambda_{abcdef}(k'', q) + \Lambda_{fcbada}(k'', -q - k'') \} \\ &\quad \times \{ I_{bcmg}^s(q + k'') I_{m'hed}^c(q) + I_{bcmg}^c(q + k'') I_{m'hed}^s(q) \} G_{gh}(k' - q) + \delta U_{ll'mm'}^{s,\text{AL}}(k, k'), \\ \delta U_{ll'mm'}^{s,\text{AL}}(k, k') &= \frac{T}{2} \sum_{q, a \sim h} U_{ll'mm'}^s \{ \Lambda_{abcdef}(k'', q) - \Lambda_{fcbada}(k'', -q - k'') \} \\ &\quad \times \{ 2I_{bcmg}^s(q + k'') I_{m'hed}^s(q) \} G_{gh}(k' - q), \end{aligned} \quad (7.5)$$

$$\Lambda_{abcdef}(q, q') = -T \sum_p G_{ab}(p+q) G_{cd}(p-q') G_{ef}(p). \quad (7.6)$$

$k'' \equiv k - k'$.

Also, we introduce the analytic expressions for dressed 4-point vertex in χ -VC without using spin and charge channel to study f -electron system with strong SOL. First, the expression for the AL1 term is given as

$$U_{\alpha\beta}^{\text{AL1}}(q) = \frac{T}{2} \sum_{\alpha'\alpha''\beta'\beta''p} C_{\alpha'\beta''}^{\alpha}(q, p) I_{\alpha'\beta'}(p-q) I_{\alpha''\beta''}(p) C_{\beta'\alpha''}^{\beta*}(\bar{q}, \bar{p}), \quad (7.7)$$

where $p \equiv (\mathbf{p}, \omega_j)$, $\bar{p} \equiv (\mathbf{p}, -\omega_j)$. The 3-point function in Eq. (7.7) is given as

$$C_{ABCD}^{EF}(q, p) \equiv -T \sum_k G_{AF}^f(k-q) G_{EC}^f(k) G_{DB}^f(k-p), \quad (7.8)$$

where \hat{G}^f is the f -electron Green function. Also, the expression for the AL2 term in χ -VC is given as

$$U_{\alpha\beta}^{\text{AL2}}(q) = \frac{T}{2} \sum_{\alpha'\beta'\alpha''\beta''p} C'_{\alpha'\beta''}{}^{\alpha}(q, p) I_{\beta''\beta'}(p-q) I_{\alpha''\alpha'}(p) \tilde{C}'_{\alpha''\beta'}{}^{\beta}(q, p), \quad (7.9)$$

where

$$\begin{aligned} C'_{ABCD}{}^{EF}(q, p) &\equiv -T \sum_k G_{BF}^f(k-q) G_{ED}^f(k) G_{CA}^f(k-q+p), \\ \tilde{C}'_{ABCD}{}^{EF}(q, p) &\equiv -T \sum_k G_{AE}^f(k+q) G_{FC}^f(k) G_{DB}^f(k+q-p). \end{aligned}$$

The total χ -VC is given by $\hat{U}^{\text{AL}} = \hat{U}^{\text{AL1}} + \hat{U}^{\text{AL2}}$ by eliminating the double counting due to the 2n order term $\propto u^2$.

Then, U -VC in f -electron system is also given by

$$(\hat{U}_{kk'})_{LL'MM'} = \frac{T}{2} \sum_{p, ABCDEF} B_{ABCDEF}^{MM'}(k-k', p, k') I_{LACD}(k-k'+p) I_{BL'EF}(-p), \quad (7.10)$$

where

$$B_{ABCDEF}^{MM'}(q, p, k') = G_{AB}^f(k'-p) \left\{ C_{CDEF}''{}^{MM'}(q, p) + C_{EFGD}''{}^{MM'}(q, q+p) \right\}, \quad (7.11)$$

$$C_{CDEF}''{}^{AB}(q, p) \equiv -T \sum_{k'} G_{CA}^f(k'+q) G_{BF}^f(k') G_{ED}^f(k'-p). \quad (7.12)$$

In addition, the expression for the AL2 term in U -VC is given as

$$U_{\alpha\beta}^{\text{AL2}}(q) = \frac{T}{2} \sum_{\alpha'\beta'\alpha''\beta''} \Lambda_{\alpha'\beta''}^{\alpha}(q, p) I_{\beta''\beta'}(p-q) I_{\alpha''\alpha'}(p) \tilde{\Lambda}_{\alpha''\beta'}^{\beta}(q, p), \quad (7.13)$$

where

$$\begin{aligned} \Lambda_{ABCD}^{EF}(q, p) &\equiv -T \sum_k G_{BF}^f(k-q) G_{ED}^f(k) G_{CA}^f(k-q+p), \\ \tilde{\Lambda}_{ABCD}^{EF}(q, p) &\equiv -T \sum_k G_{AE}^f(k+q) G_{FC}^f(k) G_{DB}^f(k+q-p). \end{aligned}$$

The expression for the MT term is written as

$$U_{LL'MM'}^{\text{MT}}(q) = T^2 \sum_{p, k, A \sim D} G_{LA}(k+q-p) G_{BL'}(k-p) G_{DM}(k+q) G_{M'C}(k) I_{DACB}(p). \quad (7.14)$$

The total U -VC is given by $\hat{U}^{\text{AL+MT}} = \hat{U}^{\text{AL1}} + \hat{U}^{\text{AL2}} + \hat{X}^{\text{MT}}$, by subtracting the double counting in the same way of χ -VC.

Appendix B: Analysis of U -VC in 1-orbital system

In the main text, we explain s -wave SC due to important roles of χ -VC and U -VC based on 2-orbital Hubbard model. In contrast, these VC can be important even in 1-orbital systems, such as Cuprate superconductor. Here, we show numerical results based on 1-orbital model. In the present model, the energy dispersion of d -electrons is defined by $\xi_k = 2t(\cos k_x + \cos k_y) + 4t' \cos k_x \cos k_y + 2t''(\cos 2k_x + \cos 2k_y)$ where $(t, t', t'') = (-1, 1/6, -1/5)$. The chemical potential is set at $\mu = -0.8$ in the following numerical study. In Fig.59, we show obtained band dispersion and Fermi surface.

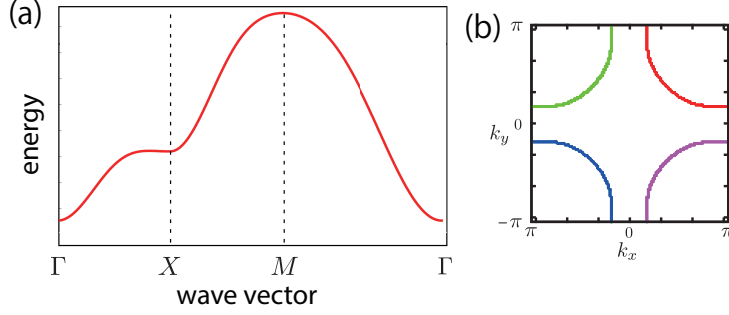


Figure 58: (a) Obtained band dispersion and (b) Fermi surface based on 1-orbital tight-binding model.

First, we perform RPA to obtain p-h susceptibility. Charge- and spin-channel susceptibility is plotted in Fig.60 (a) and (b), respectively. Here we put $\alpha_S = 0.9$ and el-ph coupling $g = 0$. Within RPA scheme, spin-channel susceptibility is much larger than charge-channel one.

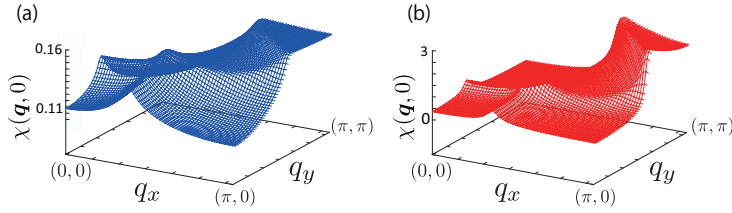


Figure 59: Obtained susceptibility of (a) charge- and (b) spin-channel.

After then, we consider el-ph interaction in A_{1g} -symmetry. In this case, g is added to SC paring interaction in linearized gap equation. In the present study, we consider only single-fluctuation term due to type-A in Fig.14. The present SC paring interaction is summarized as

	bare 4-point	bare 4-point	single-flctuation
spin-channel	0	U	$U^2 \chi_{RPA}^s$
charge-channel	g	$-U$	$U^2 \chi_{RPA}^c$

Here, the charge-channel susceptibility χ_{RPA}^c includes g , which is written by

$$\chi_{RPA}^c = \frac{\chi^0}{1 + (U - g)\chi^0}. \quad (7.15)$$

In the present study, we fix charge channel Stoner factor at $\alpha_C = 0.7$

In addition, we consider AL-type VC for SC paring interaction. The effects of g in AL-VC is neglected as discussed in Sec.3. In Fig.60 (a) and (b), obtained gap function for s - and d -wave symmetry are plotted. s -wave gap is quite isotropic while d -wave has angular-dependence belonging to $d_{x^2-y^2}$ -symmetry. In Fig.60 (c), effective SC paring interaction for each gap function is plotted. d -wave SC state is realized when the spin Stoner factor α_S is small while that for both s - and d -wave reaches the same value with large α_S due to AFM-QCP. Thus, we conclude that attractive SC paring interaction for isotropic s -wave state is strongly enlarged by AL-VC even in 1-orbital system as well as 2-orbital one.

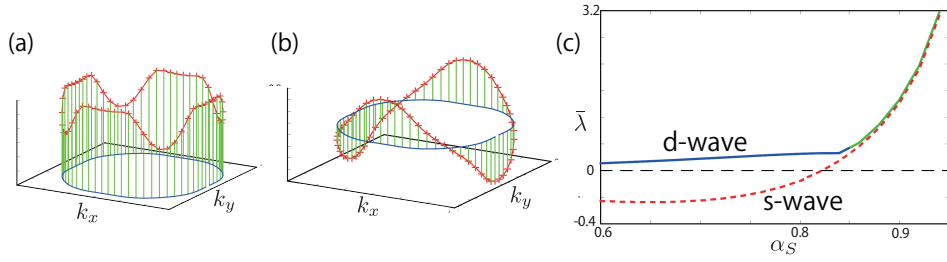


Figure 60: Gap function on the Fermi surface with (a) s-wave and (b) $d_{x^2-y^2}$ -wave symmetry. (c) Obtained effective SC pairing interaction. Red-dotted (blue-solid) line corresponds to s- (d -) wave SC state.

In Fig.61(a) and (b), we show obtained $(U-VC)^2$ due to AL-term for charge- and spin-channel. Charge-channel $U-VC$ is about ~ 3 while the maximum value of spin channel is only about ~ 0.8 . Therefore, we conclude that charge-channel AL-term strongly enhances the attractive pairing interaction due to charge-channel fluctuations (factor 3). In contrast, we naturally expect that only repulsive interaction is enhanced if we neglect $U-VC$. To identify this fact, we plot the effective SC interaction without $U-VC$ in Fig.61(c). Only d -wave state is stabilized near AFM-QCP. As a result, we reveal the importance of $U-VC$ in 1-orbital model with small el-ph interaction. Finally, we plot the effective interaction for isotropic gap function based on local approximation in 61(d). In this calculation, the k -dependence of $U-VC$ is averaged over Fermi surface. The s-wave SC interaction is much larger than that in local approximation (about factor ~ 3). This is understood by the fact that $U-VC$ in local approximation is proportional to $(\sum_q \chi^s(q))^2 \propto \xi^0$ while original one shows $\sum_q (\chi^s(q))^2 \propto \xi^2$ where ξ is correlation length. Therefore, it is verified that momentum dependence of $U-VC$ is important in 1-orbital system as well as 2-orbital system.

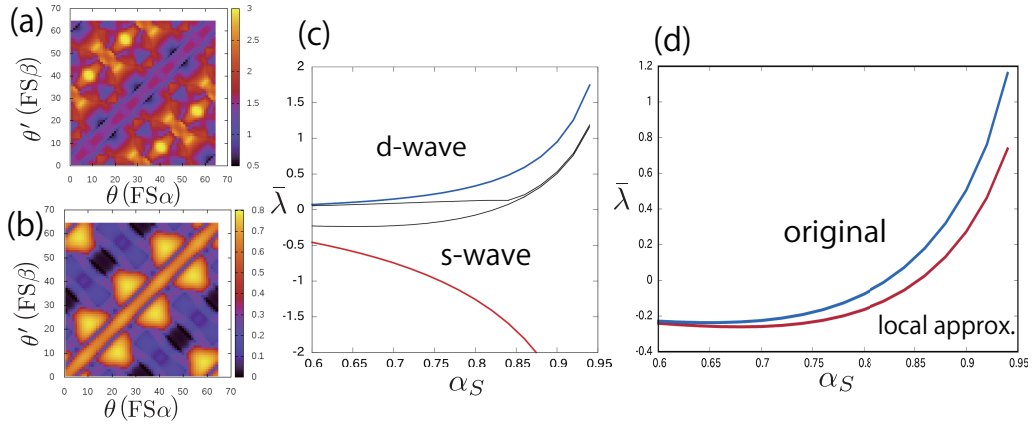


Figure 61: (a) Charge channel and (b) spin channel enhancement factor given by $(U-VC)^2$ (c) Effective pairing interaction $\bar{\lambda}$ in the absence of $U-VC$. (d) $\bar{\lambda}$ based on the local approximation (red line) and original one (blue line).

Here, we explain detailed explanation of the B_{1g} -phonon introduced in Sec.3 based on 2-orbital HH model. In the present model has $SU(2)$ symmetry and the bare 4-point vertex is written by spin and charge channel. In addition, Pauli exclusion principle is considered for the on-site Coulomb interaction. Then, each elements of the 4-point vertex function is given in Fig.62 and 63. The cross mark denotes prohibition by Pauli principle.

Appendix C: $J = 5/2$ PAM for $CeCu_2Si_2$

Here, we explain about the ground states of $J = 5/2$ PAM and derivation of complex hopping parameters given by Eq.(4.3) based on Slater-Koster table. The ground states in the present model in

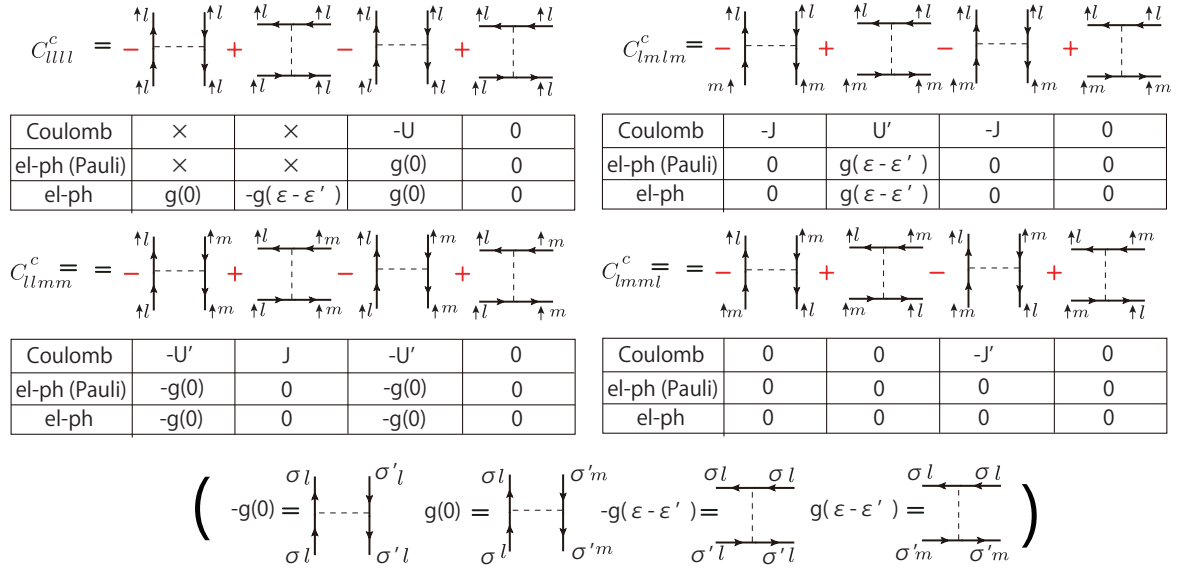
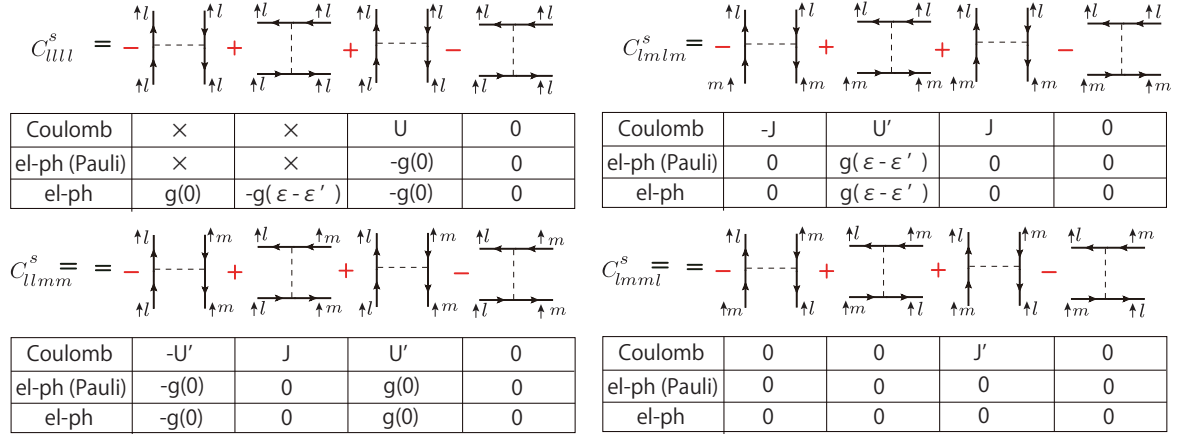
Figure 62: Definition of the charge-channel bare 4-point vertex due to B_{1g} -phonon in 2-orbital (d_{xz}, d_{yz})-model.

Figure 63: Definition of the spin-channel bare 4-point vertex.

l_z -basis are written as

$$|f_1 \downarrow\rangle = a \left\{ \sqrt{\frac{1}{7}} |2, \uparrow\rangle - \sqrt{\frac{6}{7}} |3, \downarrow\rangle \right\} + b \left\{ \sqrt{\frac{5}{7}} |-2, \uparrow\rangle - \sqrt{\frac{2}{7}} |-1, \downarrow\rangle \right\}, \quad (7.16)$$

$$|f_1 \uparrow\rangle = a \left\{ \sqrt{\frac{6}{7}} |-3, \uparrow\rangle - \sqrt{\frac{1}{7}} |-2, \downarrow\rangle \right\} + b \left\{ \sqrt{\frac{2}{7}} |1, \uparrow\rangle - \sqrt{\frac{5}{7}} |2, \downarrow\rangle \right\}, \quad (7.17)$$

$$|f_2 \uparrow\rangle = -a \left\{ \sqrt{\frac{2}{7}} |1, \uparrow\rangle - \sqrt{\frac{5}{7}} |2, \downarrow\rangle \right\} + b \left\{ \sqrt{\frac{6}{7}} |-3, \uparrow\rangle - \sqrt{\frac{1}{7}} |-2, \downarrow\rangle \right\}, \quad (7.18)$$

$$|f_2 \downarrow\rangle = -a \left\{ \sqrt{\frac{5}{7}} |-2, \uparrow\rangle - \sqrt{\frac{2}{7}} |-1, \downarrow\rangle \right\} + b \left\{ \sqrt{\frac{1}{7}} |2, \uparrow\rangle - \sqrt{\frac{6}{7}} |3, \downarrow\rangle \right\}, \quad (7.19)$$

where \uparrow (\downarrow) is pseudo spin and \uparrow (\downarrow) denotes the real spin. Note that the wave functions for $l_z = \pm 2$ are proportional to z ,

$$\langle \vec{r} | \pm 2, \sigma \rangle \propto z.$$

Therefore, in 2D system, the hopping integrals between s -orbital and $l_z = 2$ electrons should be zero. Thus, $\langle s, \sigma, \vec{R}_i | \pm 2, \sigma, \vec{R}_j \rangle = 0$ is satisfied. Finally, we obtain

$$\langle s \uparrow | f_1 \uparrow \rangle = \sqrt{\frac{6}{7}} \langle s \uparrow | -3, \uparrow \rangle, \quad \langle s \downarrow | f_1 \downarrow \rangle = -\sqrt{\frac{6}{7}} \langle s \downarrow | 3, \downarrow \rangle, \quad (7.20)$$

$$\langle s \uparrow | f_2 \uparrow \rangle = -\sqrt{\frac{2}{7}} \langle s \uparrow | 1, \uparrow \rangle, \quad \langle s \downarrow | f_2 \downarrow \rangle = \sqrt{\frac{2}{7}} \langle s \downarrow | -1, \downarrow \rangle, \quad (7.21)$$

where $a = 1, b = 0$ is adopted. Here, each wave functions $|\pm 3, \sigma\rangle, |\pm 1, \sigma\rangle$ are written in (x, y, z) -basis.

$$|\pm 3, \sigma\rangle = -\sqrt{\frac{5}{16}} \{ \pm x(5x^2 - 3r^2) - iy(5y^2 - 3r^2) \} - \sqrt{\frac{3}{16}} \{ \mp x(y^2 - z^2) - iy(z^2 - x^2) \}, \quad (7.22)$$

$$|\pm 1, \sigma\rangle = -\sqrt{\frac{3}{16}} \{ \mp x(5x^2 - 3r^2) - iy(5y^2 - 3r^2) \} - \sqrt{\frac{5}{16}} \{ \pm x(y^2 - z^2) - iy(z^2 - x^2) \}. \quad (7.23)$$

Therefore, we obtain the hopping parameters;

$$\begin{aligned} \langle s | \pm 3, \sigma \rangle &= -\sqrt{\frac{5}{16}} \{ \pm \langle s | x(5x^2 - 3r^2) \rangle \langle s | y(5y^2 - 3r^2) \rangle \} - \sqrt{\frac{3}{16}} \{ \mp \langle s | x(y^2 - z^2) \rangle - i \langle s | y(z^2 - x^2) \rangle \}, \\ &= -\sqrt{\frac{5}{16}} \left\{ \pm \frac{l}{2} (5l^2 - 3) - i \frac{m}{2} (5m^2 - 3) \right\} - \sqrt{\frac{3}{16}} \left\{ \mp \frac{\sqrt{15}}{2} l(m^2 - n^2) - i \frac{\sqrt{15}}{2} m(n^2 - l^2) \right\} t_{sf}. \end{aligned}$$

$$\begin{aligned} \langle s | \pm 1, \sigma \rangle &= -\sqrt{\frac{3}{16}} \{ \mp \langle s | x(5x^2 - 3r^2) \rangle - i \langle s | y(5y^2 - 3r^2) \rangle \} - \sqrt{\frac{5}{16}} \{ \pm \langle s | x(y^2 - z^2) \rangle - i \langle s | y(z^2 - x^2) \rangle \}, \\ &= -\sqrt{\frac{3}{16}} \left\{ \mp \frac{l}{2} (5l^2 - 3) - i \frac{m}{2} (5m^2 - 3) \right\} - \sqrt{\frac{5}{16}} \left\{ \pm \frac{\sqrt{15}}{2} l(m^2 - n^2) - i \frac{\sqrt{15}}{2} m(n^2 - l^2) \right\} t_{sf}, \end{aligned}$$

where $l = \cos \phi \sin \theta, m = \sin \phi \sin \theta, n = \cos \theta$. Here, $t_{sf} = (sf\sigma)$. Then, we consider the nearest neighbor hopping on 2D square lattice, that is, Ce-ions at $(l, m, n) = (0, 1, 0), (-1, 0, 0), (0, -1, 0), (1, 0, 0)$. Therefore, we obtain

$$\langle s | \pm 3, \sigma \rangle_{NN} = \sqrt{\frac{5}{16}} \{ i e^{ik_y a} \pm e^{-ik_x a} - i e^{-ik_y a} \mp e^{ik_x a} \} t_{sf} = \sqrt{\frac{5}{16}} (-2 \sin k_y \mp 2i \sin k_x) t_{sf}, \quad (7.24)$$

$$\langle s | \pm 1, \sigma \rangle_{NN} = \sqrt{\frac{3}{16}} \{ i e^{ik_y a} \mp e^{-ik_x a} - i e^{-ik_y a} \pm e^{ik_x a} \} t_{sf} = \sqrt{\frac{3}{16}} (-2 \sin k_y \pm 2i \sin k_x) t_{sf}. \quad (7.25)$$

Then, the s - f hopping term is given by

$$\langle s \uparrow | f_1 \uparrow \rangle = -\sqrt{\frac{15}{14}} t_{sf} (\sin k_y - i \sin k_x), \quad \langle s \downarrow | f_1 \downarrow \rangle = \sqrt{\frac{15}{14}} t_{sf} (\sin k_y + i \sin k_x), \quad (7.26)$$

$$\langle s \uparrow | f_2 \uparrow \rangle = \sqrt{\frac{3}{14}} t_{sf} (\sin k_y - i \sin k_x), \quad \langle s \downarrow | f_2 \downarrow \rangle = -\sqrt{\frac{3}{14}} t_{sf} (\sin k_y + i \sin k_x). \quad (7.27)$$

Appendix D: Coulomb interaction based on multipole basis

Now, we explain how to obtain Coulomb interaction 4-point vertex based on multipole basis. In the present study, we calculate the Coulomb interaction by using Slater-Condon parameter ($F^p.p = 0, 2, 4, 6$). To begin with, we start from

$$\bar{U}_{l_z l'_z, l''_z l'''_z} = \frac{e^2}{4\pi\epsilon_0} \int d\vec{r} \int d\vec{r}' \frac{u_{l_z}^{l''*}(\vec{r}) u_{l'_z}^{l'''*}(\vec{r}') u_{l''_z}^l(\vec{r}) u_{l'''_z}^l(\vec{r}')}{|\vec{r} - \vec{r}'|} \quad (7.28)$$

where $u_m(\vec{r})$ is written by $u_m^l(\vec{r}) = R_l(r)\Theta_m^l(\phi)$ and $\Phi_m(\phi) = 1/\sqrt{2\pi}e^{im\phi}$. Here, $|\vec{r} - \vec{r}'|$ is expanded as

$$\frac{1}{|\vec{r} - \vec{r}'|} = \sum_{k,n} \frac{(k - |n|)!}{(k + |n|)!} \frac{r^k(a)}{r^{k+1}(b)} P_k^{|n|}(\cos \theta) P_k^{|n|}(\cos \theta') e^{in(\phi - \phi')}, \quad (7.29)$$

where $r(a) = r', r(b) = r$ when $r > r'$, $r(a) = r, r(b) = r'$ when $r < r'$. P is Legendre function. In this case,

$$\begin{aligned} \bar{U}_{l_z l'_z l''_z l'''_z} &= \frac{e^2}{4\pi\epsilon_0} \int d\vec{r} \int d\vec{r}' R_l^2(r) R_l^2(r') \sum_{k,n} \frac{r^k(a)}{r^{k+1}(b)} r^2 r'^2 \int d\theta \sin \theta \int d\theta' \sin \theta' \\ &\times \Theta_{l_z}^{l_*}(\theta) \Theta_{l'_z}^{l_*}(\theta') \Theta_{l''_z}^{l_*}(\theta) \Theta_{l'''_z}^{l_*}(\theta') P_k^{|n|}(\cos \theta) P_k^{|n|}(\cos \theta') \frac{(k - |n|)!}{(k + |n|)!} \\ &\times \int d\phi \int d\phi' \Phi_{l_z}^*(\phi) \Phi_{l'_z}^*(\phi') \Phi_{l''_z}(\phi) \Phi_{l'''_z}(\phi) e^{in(\phi - \phi')}. \end{aligned} \quad (7.30)$$

Note that

$$\Phi_{l_z}^*(\phi) \Phi_{l'_z}^*(\phi') \Phi_{l''_z}(\phi) \Phi_{l'''_z}(\phi) e^{in(\phi - \phi')} = \delta_{-n, l_z - l'_z} \delta_{n, l''_z - l'''_z} \quad (7.31)$$

Therefore, the Coulomb interaction is written by

$$\bar{U}_{l_z l'_z l''_z l'''_z} = \sum_k F^k a_{l_z l'_z l''_z l'''_z}^k \quad (7.32)$$

$$\begin{aligned} F^k &\equiv \frac{e^2}{4\pi\epsilon_0} \int d\vec{r} \int d\vec{r}' R_l^2(r) R_l^2(r') \sum_{k,n} \frac{r^k(a)}{r^{k+1}(b)} r^2 r'^2 \\ a_{l_z l'_z l''_z l'''_z}^k &\equiv 2 \int d\theta \sin \theta \int d\theta' \sin \theta' \Theta_{l_z}^{l_*}(\theta) \Theta_{l'_z}^{l_*}(\theta') \Theta_{l''_z}^{l_*}(\theta) \Theta_{l'''_z}^{l_*}(\theta') \\ &\times P_k^{|l_z - l''_z|}(\cos \theta) P_k^{|l'_z - l'''_z|}(\cos \theta') \frac{(k - |l_z - l''_z|)!}{(k + |l_z - l''_z|)!}. \end{aligned} \quad (7.33)$$

where

$$\begin{aligned} \Theta_{l_z}^{l_*}(\theta) &= \sqrt{\frac{(2l + 1)(l - |l_z|)!}{(l + |l_z|)!}} P_l^{|l_z|}(\cos \theta) \\ P_l^{|l_z|} &= \frac{1}{2^l l!} \sin(\theta)^{|l_z|} \frac{\partial^{l+|l_z|}}{\partial(\cos \theta)^{l+|l_z|}} \{-1^l (1 - \cos^2 \theta)^l\} \end{aligned} \quad (7.34)$$

In the present study, we set $(F^0, F^2, F^4, F^6) = (5.3, 9.09, 6.927, 4.756)$. $a_{l_z l'_z l''_z l'''_z}^k$ is related to the angular dependence of the on-site Coulomb interaction, which is easily calculated by using Mathematica.

Appendix E: Multipole operator

In this section, we explain the derivation of multipole operators. In the present $J = 5/2$ model, we can define multipole operators up to rank 5 (= 5 - (-5)). In the space inversion symmetry, the odd (even) rank operator contributes to the magnetic (electric) or TRS odd (even) symmetry. As shown in the main text, the multipole operator of rank k is written by angular momentum operator \hat{J} based on equivalent operator method, which is verified by using Wigner-Eckart theorem. The operator of rank k is defined as

$$[J_{\pm}, J_q^{(k)}] = \sqrt{(k \mp q)(k \pm q + 1)} J_{q\pm 1}^{(k)} \quad (7.35)$$

$$J_k^{(k)} = (-1)^k \sqrt{\frac{(2k - 1)!!}{(2k)!!}} J_+^k. \quad (7.36)$$

To change the general matrix $J_q^{(k)}$ into unitary matrix, we define $\tilde{J}_q^{(k)}$ as

$$\begin{aligned}\tilde{J}_{[2p-1]_+}^{(k)} &\equiv \frac{i}{\sqrt{2}}(J_{2p-1}^{(k)} + J_{-(2p-1)}^{(k)}), & \tilde{J}_{[2p-1]_-}^{(k)} &\equiv \frac{1}{\sqrt{2}}(-J_{2p}^{(k)} + J_{-(2p-1)}^{(k)}) \\ \tilde{J}_{[2p]_+}^{(k)} &\equiv \frac{1}{\sqrt{2}}(J_{2p}^{(k)} + J_{-2p}^{(k)}), & \tilde{J}_{[2p]_-}^{(k)} &\equiv \frac{i}{\sqrt{2}}(-J_{2p}^{(k)} + J_{-2p}^{(k)})\end{aligned}\quad (7.37)$$

In 2D (D_{4h} -symmetry) system, the characteristic table for each multipole operators was obtained in Ref.[13] in Sec.4 as follows;

$$\begin{aligned}A_1^+ : O_{20} &= J_0^{(2)}, & H_0 &= \frac{1}{\sqrt{12}}(\sqrt{7}J_0^{(4)} + \sqrt{5}\tilde{J}_{[4]_+}^{(4)}), & H_4 &= \frac{1}{\sqrt{12}}(\sqrt{5}J_0^{(4)} - \sqrt{7}\tilde{J}_{[4]_+}^{(4)}) \\ A_2^+ : H_{za} &= \tilde{J}_{[4]_-}^{(4)} \\ B_1^+ : O_{22} &= \tilde{J}_{[2]_+}^{(2)}, & H_2 &= \tilde{J}_{[2]_+}^{(4)} \\ B_2^+ : O_{xy} &= \tilde{J}_{[2]_-}^{(2)}, & H_{zb} &= \tilde{J}_{[2]_-}^{(4)} \\ E^+ : O_{yz(zx)} &= \tilde{J}_{[1]_{+(-)}}^{(2)}, & H_{xa(ya)} &= \frac{1}{\sqrt{8}}(+(-)\tilde{J}_{[3]_{+(-)}}^{(4)} + \sqrt{7}\tilde{J}_{[1]_{+(-)}}^{(4)}), \\ & & H_{xb(yb)} &= \frac{1}{\sqrt{8}}(+(-)\sqrt{7}\tilde{J}_{[3]_{+(-)}}^{(4)} - \tilde{J}_{[1]_{+(-)}}^{(4)}), \\ A_1^- : D_4 &= \tilde{J}_{[4]_-}^{(5)} \\ A_2^- : J_z &= J_0^{(1)}, & T_{za} &= J_0^{(3)}, & D_{za1} &= J_0^{(5)}, & D_{za2} &= \tilde{J}_{[4]_+}^{(5)} \\ B_1^- : T_{xyz} &= \tilde{J}_{[2]_-}^{(3)}, & D_2 &= -\tilde{J}_{[2]_-}^{(5)} \\ B_2^- : T_{zb} &= \tilde{J}_{[2]_+}^{(3)}, & D_{zb} &= \tilde{J}_{[2]_+}^{(5)} \\ E^- : J_{x(y)} &= \tilde{J}_{[2]_{-(+)}}^{(1)}, & T_{xa(ya)} &= \frac{1}{\sqrt{8}}(+(-)\sqrt{5}\tilde{J}_{[3]_{-(+)}}^{(3)} - \sqrt{3}\tilde{J}_{[1]_{-(+)}}^{(3)}) \\ & & T_{xb(yb)} &= \frac{1}{\sqrt{8}}(-\sqrt{3}\tilde{J}_{[3]_{-(+)}}^{(3)} - (+)\sqrt{5}\tilde{J}_{[1]_{-(+)}}^{(3)}), \\ & & D_{xa1(ya1)} &= \frac{1}{16}(3\sqrt{14}\tilde{J}_{[5]_{-(+)}}^{(5)} - (+)\sqrt{70}\tilde{J}_{[3]_{-(+)}}^{(5)} + 2\sqrt{15}\tilde{J}_{[1]_{-(+)}}^{(5)}) \\ & & D_{xa2(ya2)} &= \frac{1}{16}(\sqrt{10}\tilde{J}_{[5]_{-(+)}}^{(5)} + (-)9\sqrt{2}\tilde{J}_{[3]_{-(+)}}^{(5)} + 2\sqrt{21}\tilde{J}_{[1]_{-(+)}}^{(5)}) \\ & & D_{xb(yb)} &= \frac{1}{8}(\sqrt{30}\tilde{J}_{[5]_{-(+)}}^{(5)} + (-)\sqrt{6}\tilde{J}_{[3]_{-(+)}}^{(5)} - 2\sqrt{7}\tilde{J}_{[1]_{-(+)}}^{(5)})\end{aligned}\quad (7.38)$$

In the 4-orbital model, the number of independent operators decreased and it should be 16(= 4 × 4), which means that 20 terms in Eq.(7.38) get to be degenerate. In particular, the matrix elements in $B_1^{+(-)}, B_2^{+(-)}$ symmetry go to zero. As a result, we obtain

$$\begin{aligned}A_1^+ : O_{20} &= J_0^{(2)}, & H_0 &= \frac{1}{\sqrt{12}}(\sqrt{7}J_0^{(4)} + \sqrt{5}\tilde{J}_{[4]_+}^{(4)}), \\ A_2^+ : H_{za} &= \tilde{J}_{[4]_-}^{(4)} \\ E^+ : O_{yz(zx)} &= \tilde{J}_{[1]_{+(-)}}^{(2)}, \\ A_1^- : D_4 &= \tilde{J}_{[4]_-}^{(5)} \\ A_2^- : J_z &= J_0^{(1)}, & T_{za} &= J_0^{(3)}, & D_{za2} &= \tilde{J}_{[4]_+}^{(5)} \\ E^- : J_{x(y)} &= \tilde{J}_{[2]_{-(+)}}^{(1)}, & T_{xa(ya)} &= \frac{1}{\sqrt{8}}(+(-)\sqrt{5}\tilde{J}_{[3]_{-(+)}}^{(3)} - \sqrt{3}\tilde{J}_{[1]_{-(+)}}^{(3)}) \\ & & D_{xa1(ya1)} &= \frac{1}{16}(3\sqrt{14}\tilde{J}_{[5]_{-(+)}}^{(5)} - (+)\sqrt{70}\tilde{J}_{[3]_{-(+)}}^{(5)} + 2\sqrt{15}\tilde{J}_{[1]_{-(+)}}^{(5)})\end{aligned}\quad (7.39)$$

Appendix F: $J = 5/2$ PAM for CeB_6

Here, we explain the model Hamiltonian for CeB_6 . The conduction band is $5d$ electrons on Ce-ions, In the present study, to simplify the model, we introduce conduction band composed of s electrons. The effective tight-binding parameters of CeB_6 is given in Ref. [21] in Sec.5. We use slightly modified model and put $k_z = 0$, in order to reproduce the experimental Fermi surfaces of CeB_6 on the k_x - k_y plane after s - f hybridization, which is given by

$$\begin{aligned} \epsilon_{\mathbf{k}} &= t_{ss}^1 (\cos k_x + \cos k_y) + t_{ss}^2 \{ \cos(k_x + k_y) + \cos(k_x - k_y) \} + t_{ss}^3 (\cos 2k_x + \cos 2k_y) \\ &+ t_{ss}^4 \{ \cos(2k_x + k_y) + \cos(2k_x - k_y) + \cos(2k_y + k_x) + \cos(2k_y - k_x) \} \\ &+ t_{ss}^5 \{ \cos(2k_x + 2k_y) + \cos(2k_x - 2k_y) \} + E_0, \end{aligned} \quad (7.40)$$

where t_{ss}^i is the i -th nearest s - s hopping integral. We set $(t_{ss}^1, t_{ss}^2, t_{ss}^3, t_{ss}^4, t_{ss}^5) = (-0.5, -0.889, 0.292, -0.229, 0.687)$, and $E_0 = 1.33$.

Next, we explain the hybridization term. Based on the Slater-Koster tight-binding method, the s - f hybridization between the nearest Ce-sites is

$$\begin{aligned} V_{\mathbf{k}f_1\uparrow} &= -A_1 t_{sf} (\sin k_y - i \sin k_x), \\ V_{\mathbf{k}f_2\uparrow} &= -A_2 t_{sf} (\sin k_y + i \sin k_x), \end{aligned} \quad (7.41)$$

and $V_{\mathbf{k}f_1\downarrow} = -V_{\mathbf{k}f_1\uparrow}^*$ and $A_1 = \sqrt{18/14}$ and $A_2 = \sqrt{3/7}$. Since $A_1 > A_2$, the relation $D_{f_1}(0) > D_{f_2}(0)$ holds in the present two-dimensional PAM, where $D_{f_i}(0)$ is the f_i -electron density-of-states at Fermi level. However, $D_{f_1}(0) = D_{f_2}(0)$ holds in the cubic model, since the s - f hybridization along z -axis is larger for f_2 -electron. To escape from the artifact of two-dimensionality, we put $A_1 = A_2 = \sqrt{18/14}$ in the present study. In the present Γ_8 model, the relation $V_{\mathbf{k}f_1\sigma} \propto V_{\mathbf{k}f_2\sigma}^*$ holds. In contrast, in the $\Gamma_7^{(1)}$ - $\Gamma_7^{(2)}$ model for CeCu_2Si_2 used in Appendix C, the relation $V_{\mathbf{k}f_1\sigma} \propto V_{\mathbf{k}f_2\sigma}$ holds.